Dissertation

submitted to the

Combined Faculties for the Natural Sciences and for Mathematics

of the Ruperto Carola University of Heidelberg, Germany

for the degree of

Doctor of Natural Sciences

Presented by

M.Sc. Navaneethan Palanisamy

born in: Appakudal (India)

Oral examination date: 14 July 2020

Molecular insights on the DNA-binding activity by the *Escherichia coli* Min CD proteins

Referees: 1) Prof. Dr. Rebecca Wade

2) Prof. Dr. Barbara Di Ventura

கேடில் விழுச்செல்வம் கல்வி யொருவற்கு
மாடல்ல மற்றை யவை.

-திருக்குறள்:400

Learning is excellence of wealth that none destroy;
To man nought else affords reality of joy.

-Thirukural:400

இடும்பைக்கு இடும்பை படுப்பர் இடும்பைக்கு
இடும்பை படாஅ தவர்.

-திருக்குறள்:623

Who griefs confront with meek, ungrieving heart,
From them griefs, put to grief, depart.

-Thirukural:623

Source: http://www.ytamizh.com/thirukural/kural

Dedicated to Godmother Melmalayanur Angalamman, my parents Vellakkarattur Kandasamy Palanisamy and Vasanthi Chellappan, and my little brother Rudhraviknesh Palanisamy (Vicky)

Acknowledgements

First and foremost, I would like to thank Prof. Dr. Barbara Di Ventura for her continuous support and supervision during the entire duration of my Ph.D. studies. I would like to thank the former and current members of Di Ventura Lab; Dr. Linda Klauss, Dr. Anna Degen, Dr. Pierre Wehler, Enoch Antwi, Edoardo Romano, Daniel Weis, Dr. Mehmet Ali Öztürk, Dagmar Krischke, Emir Bora Akmeriç, Jara Ballestin Ballestin, Simone Ugi, Dominik Niopek, Max C. Waldhauer and Silvan N. Schmitz for their help and for maintaining a friendly laboratory environment. I would like to thank my students Anna Maria Melzer, Hanna Wetzel, and Mais Alsousli for their small yet significant contributions for my Ph.D. research.

I would like to thank Prof. Dr. Roland Eils and his group members Dr. Stefan Kallenberger, Chiara Di Ponzio and Manuela Schäfer for maintaining a wonderful working atmosphere in Heidelberg, during the initial phase of my Ph.D. studies.

I would like to thank our collaborators Prof. Dr. Wolfgang Schamel and his group; Dr. Anna Morath and Claudia Juraske, and Dr. Jung-Won Youn and Prof. Dr. Georg A. Sprenger for their extraordinary contributions towards inteins project. I would like to thank our collaborators Prof. Dr. Rasmus Schröder and his group; Dr. Johan Zeelen and Dr. Götz Hofhaus, Dr. Günter Roth and his group; Christin Rath and Normann Kilb, Dr. Martin Beck, Dr. Beata Turonova, Dr. Aswin Sai Narain Seshasayee, Dr. Parul Singh and Prof. Dr. Rebecca Wade for their contributions towards DNA binding by the *E. coli* MinCD proteins project.

I would like to thank Prof. Dr. Sonja-Verena Albers, Dr. Chris van der Does and João Nuno de Sousa Machado for clarifying my technical doubts from time to time, and for providing liposomes and for performing size-exclusion chromatography experiments for the MinE-eYFP project.

Last, but not least, I would like to thank my friends Dr. Bushra Saeed, Arunraj Dhamodaran, Abinaya Kamaraj, Dr. Kanagaraj Palsamy, Dr. Vinodh Ilangovan, Dr. Oliva Saldanha, Dr. Sankari Nagarajan, Kritika Bhatia, Lenin Chandran, Karthikeyan Dhamotharan, Praveen Kumar Nattramilarasu, Advait Jagirdar, Kamal Prakash P. R. Nair and Dr. Harikrishnan Radhakrishnan.

Contributions

Circular dichroism (CD) spectroscopy experiments and size-exclusion chromatography experiments with the N-terminal domain of MinC WT and mutants were performed by the Protein Expression and Protein Purification Core Facility of the European Molecular Biology Laboratory (EMBL), Heidelberg.

Computational analyses were performed by Dr. Mehmet Ali Öztürk, a former Ph.D. student of Prof. Rebecca Wade, who is currently a postdoctoral researcher in our lab.

Microscopy images were taken by Edoardo Romano, a Ph.D. student in our lab and Emir Bora Akmeriç, a technical assistant in our lab.

German translation of my Ph.D. thesis summary was done by Daniel Weis, a Ph.D. student in our lab.

Wherever applicable, the contributions provided by respective people have been duly stated in my thesis.

Summary

Every living organism, including viruses, has to undergo reproduction in order to successfully establish a niche on this planet. One of the vital steps in the reproduction process is replication of the genetic material and its subsequent segregation between the two daughter cells. Errors in these processes may be fatal to the organism causing it to disappear from this planet.

Eukaryotic cells have evolved an energy-consuming dedicated machinery to properly segregate the replicated genetic material between the two daughter cells. Unlike eukaryotes, prokaryotes adopt different mechanisms for chromosome segregation, which are in some cases still poorly understood. Moreover, in prokaryotes, chromosome replication and segregation happen simultaneously. While a dedicated chromosome segregation machinery has been identified in *Caulobacter crescentus*, such machinery has not been identified in many other prokaryotes. There is an ongoing debate in the prokaryotic field whether mere entropic forces of repulsion between the duplicated chromosomes alone can achieve full and precise chromosome segregation, or whether additional machineries are needed.

A previous study from our group has shown that *Escherichia coli* MinD binds to DNA in a non-sequence-specific manner. Based on computational, *in vitro* and *in vivo* analyses, it was hypothesized that such binding would be used by *E. coli* cells to properly segregate their chromosomes. Residues on MinD that, either directly or indirectly, affect DNA binding have been identified; however, the direct MinD-DNA binding interface is so far unknown.

E. coli MinD, together with MinC and MinE, constitutes the so-called Min system, which has been extensively studied for its role in mid-cell determination. MinC actively counteracts FtsZ polymerization. It would do this anywhere in the cell, if it were not for MinD and MinE, which regulate MinC localization so that it is minimal at mid-cell, where the FtsZ ring can be assembled. The way in which MinD and MinE keep MinC away from mid-cell is very dynamic, and consists in pole-to-pole oscillations that never cease. These oscillations are self-organized and occur also in the absence of MinC, as far as MinD, MinE and the membrane are present. Since MinC forms a complex with MinD, it effectively gets carried along in the oscillations, spending on average more time at the poles and being at low concentration at the centre. Without MinC, the Min oscillations do not exert any activity towards FtsZ. Thus, the three Min proteins ought to work together to achieve their goal of mid-cell determination. It is plausible that a concerted action of all Min proteins is required also for proper chromosome

segregation, since we discovered that MinC strongly enhances the DNA-binding activity of MinD, while MinE terminates the binding by releasing MinC and the DNA off MinD (1).

In my thesis, I aimed to identify the residues of MinC that either directly or indirectly aid MinD in DNA binding. To this end, potential MinC residues that could bind to the DNA were first computationally predicted and then mutated to experimentally test the consequences of such mutations on the DNA binding activity of MinC and MinD. Using electrophoretic mobility shift assay (EMSA) experiments, I found that glycine at position 10 and lysine at position 66 on MinC are involved in DNA binding since the $MinC^{G10D}$ and $MinC^{K66A}$ mutants showed strongly reduced binding. By performing circular dichroism experiments, I could exclude that the impairment of $MinC^{G10D}$-MinD in DNA binding is due to changes in the secondary structure of the mutant protein, suggesting that the DNA is repelled by the negative charge of the aspartic acid. Most importantly, I discovered that not only the length, but also the amino acid sequence of the unstructured linker region of MinC, which connects the N- and the C-terminal domains of the protein, play a vital role in the DNA-binding activity of MinCD. Since MinC is also involved in inhibiting FtsZ polymerization, by performing cell viability spot assays I found that the linker should consist of at least two amino acids in order to efficiently inhibit FtsZ polymerization. EMSA assays with various synthetic constructs I made to test the necessity of different elements (MinC N- and C-terminal domain, linker region, MinD) for DNA binding revealed that the linker region of MinC is necessary for DNA binding. Further experiments are needed to understand if MinC N- and C-terminal domains and MinD are needed solely to place the linker in the proper orientation for it to bind to the DNA or if they contribute directly to the binding with specific residues. Interestingly, microscopy experiments performed using a synthetic construct made of the N-terminal MinC domain, the linker, a bZIP dimerizing domain and mRuby showed that this construct co-localizes with the *E. coli* nucleoid. Introduction of the G10D mutation on the synthetic construct did not alter its *in vivo* association with the nucleoid, suggesting that G10 is not used to directly bind to the DNA.

Beyond studying the DNA binding activity of MinC and MinD, during my Ph.D. I analyzed the mechanism by which MinE is impaired when eYFP is C-terminally fused to it. By combining *in vivo* and *in vitro* assays, I show that eYFP makes the fusion protein prone to aggregation, and reduces the accessibility of MinE MTS as well as of arginine at position 21, needed to activate the ATPase activity of MinD.

Finally, as to study biological processes it is often necessary to co-transform two plasmids in the cells of interest, I wanted to devise a method to reduce the requirement from

two to one antibiotic to maintain two plasmids. To this aim, I employed split inteins to reconstitute full-length, functional enzymes conferring resistance towards antibiotics, which are expressed as two dysfunctional halves each on one plasmid. This method, which we called SiMPl, allows maintaining two plasmids in bacteria and mammalian cells using a single antibiotic chosen between kanamycin, chloramphenicol, ampicillin, hygromycin and puromycin.

Zusammenfassung

Jeder lebende Organismus, einschließlich Viren, muss sich vermehren, um erfolgreich eine Nische auf diesem Planeten aufzubauen. Einer der entscheidenden Schritte im Reproduktionsprozess ist die Replikation des genetischen Materials und dessen anschließende Trennung zwischen den beiden Tochterzellen. Fehler in diesen Prozessen können für den Organismus tödlich sein und dazu führen, dass er von diesem Planeten verschwindet.

Eukaryontische Zellen haben eine spezielle Maschinerie entwickelt, die Energie nutzt, um das replizierte genetische Material zwischen den beiden Tochterzellen richtig zu trennen. Im Gegensatz zu Eukaryoten wenden Prokaryoten unterschiedliche Mechanismen für die Chromosomensegregation an, die in einigen Fällen noch wenig verstanden werden. Darüber hinaus finden bei Prokaryoten die Replikation und Segregation der Chromosomen gleichzeitig statt. Während bei *Caulobacter crescentus* eine spezielle Chromosomensegregations-maschinerie identifiziert wurde, wurde diese Maschinerie bei vielen anderen Prokaryoten nicht identifiziert. Auf dem Gebiet der Prokaryoten gibt es eine anhaltende Debatte darüber, ob bloße entropische Abstoßungskräfte zwischen den duplizierten Chromosomen allein eine vollständige und präzise Chromosomensegregation erreichen können oder ob zusätzliche Mechanismen erforderlich sind.

Eine frühere Studie aus unserer Gruppe hat gezeigt, dass *Escherichia coli* MinD nicht sequenzspezifisch an DNA bindet. Basierend auf Computer-, *In-vitro*- und *In-vivo*-Analysen wurde die Hypothese aufgestellt, dass eine solche Bindung von *E. coli*-Zellen verwendet wird, um ihre Chromosomen richtig zu trennen. Aminosäuren von MinD, die entweder direkt oder indirekt die DNA-Bindung beeinflussen, wurden identifiziert; Die direkte MinD-DNA-Bindungsschnittstelle ist jedoch bislang unbekannt. *E. coli* MinD bildet zusammen mit MinC und MinE das sogenannte Min-System, das eingehend auf seine Rolle bei der Bestimmung der Mitte der Zelle untersucht wurde. MinC wirkt der FtsZ-Polymerisation aktiv entgegen. Dies würde überall in der Zelle geschehen, wenn es nicht MinD und MinE gäbe, die die MinC-Lokalisierung so regulieren, dass sie in der Mitte der Zelle, in der der FtsZ-Ring zusammengesetzt werden kann, minimal ist. Die Art und Weise, wie MinD und MinE MinC von der Mitte der Zelle fernhalten, ist sehr dynamisch und besteht in einer kontinuierlichen Oszillation von Pol zu Pol, die niemals aufhört. Diese Oszillationen sind selbstorganisiert und treten auch in Abwesenheit von MinC auf, sofern MinD, MinE und die Membrane vorhanden sind. Da MinC mit MinD einen Komplex bildet, wird es mitgezogen, verbringt dadurch

durchschnittlich mehr Zeit an den Polen und kommt in der Mitte in geringer Konzentration vor. Ohne MinC üben die Min-Oszillationen keine Aktivität gegenüber FtsZ aus. Daher sollten die drei Min-Proteine zusammenarbeiten, um ihr Ziel, die Bestimmung der Mitte der Zelle, zu erreichen.

Es ist denkbar, dass eine konzertierte Wirkung aller Min-Proteine auch für eine ordnungsgemäße Chromosomensegregation erforderlich ist, da wir festgestellt haben, dass MinC die DNA-Bindungsaktivität von MinD stark erhöht, während MinE die Bindung von MinC und der DNA mit MinD beendet (1).

In meiner Doktorarbeit wollte ich die Aminosäuren von MinC identifizieren, die MinD entweder direkt oder indirekt bei der DNA-Bindung unterstützen. Zu diesem Zweck wurden potenzielle MinC-Aminosäuren, die an die DNA binden könnten, zuerst rechnerisch vorhergesagt und dann mutiert, um die Konsequenzen solcher Mutationen auf die DNA-Bindungsaktivität von MinC und MinD experimentell zu testen. Unter Verwendung von EMSA-Experimenten (Electrophoretic Mobility Shift Assay) fand ich heraus, dass Glycin an Position 10 und Lysin an Position 66 auf MinC eine wichtige Rolle bei der DNA-Bindung spielen, da die MinCG10D- und MinCK66A-Mutanten eine stark reduzierte Bindung zeigten.

Durch die Durchführung von Zirkulardichroismus-Experimenten konnte ich ausschließen, dass die Beeinträchtigung der DNA-Bindung von MinCG10D-MinD auf Änderungen der Sekundärstruktur des mutierten Proteins zurückzuführen ist, was darauf hindeutet, dass die DNA durch die negative Ladung der Asparaginsäure abgestoßen wird. Vor allem entdeckte ich, dass nicht nur die Länge, sondern auch die Aminosäuresequenz der unstrukturierten Linkerregion von MinC, die seine N- und C-terminalen Domänen verbindet, eine wichtige Rolle bei der DNA-Bindungsaktivität von MinCD spielt. Da MinC auch an der Hemmung der FtsZ-Polymerisation beteiligt ist, fand ich durch Durchführung von Zellviabilität -Assays heraus, dass der Linker mindestens 2 Aminosäuren aufweisen sollte, um die FtsZ-Polymerisation effizient zu hemmen. EMSA-Assays mit verschiedenen synthetischen Konstrukten, die von mir hergestellt wurden, um die Notwendigkeit verschiedener Elemente (MinC-N und Cterminale Domäne, Linkerregion, MinD) für die DNA-Bindung zu testen, zeigten, dass die MinC-Linkerregion für die DNA-Bindung notwendig ist, sofern es sich um ein Dimer handelt. Weitere Experimente sind erforderlich, um zu verstehen, ob MinC N- und C-terminale Domänen und MinD nur benötigt werden, um den Linker in die richtige Orientierung zu bringen, damit er an die DNA bindet, oder ob sie direkt zur Bindung mit

spezifischen Resten beitragen. Interessanterweise zeigten Mikroskopieexperimente, die unter Verwendung eines synthetischen Konstrukts aus der N-terminalen MinC-Domäne, dem Linker, einer bZIP-Dimerisierungsdomäne und mRuby durchgeführt wurden, dass dieses Konstrukt zusammen mit dem *E. coli*-Nukleoid lokalisiert ist. Die Einführung der G10D-Mutation in das synthetische Konstrukt veränderte seine *In-vivo*-Assoziation mit dem Nukleoid nicht, was darauf hindeutet, dass G10 nicht zur direkten Bindung an die DNA verwendet wird. Neben der Untersuchung der DNA-Bindungsaktivität von MinC und MinD analysierte ich während meiner Doktorarbeit den Mechanismus, durch den eYFP C-terminal an MinE fusioniert wird und dessen Funktion beeinträchtigt. Durch die Kombination von *In-vivo*-Tests und *In-vitro*-Tests zeige ich, dass eYFP das Fusionsprotein zur Aggregation neigen lässt und die Zugänglichkeit von MinE MTS sowie von Arginin an Position 21 verringert, die zur Aktivierung der ATPase-Aktivität von MinD erforderlich ist.

Schließlich wollte ich, da zur Untersuchung von biologischen Prozessen oft zwei Plasmide co-transformiert werden müssen, eine Methode entwickeln, um zwei Plasmide mit einem Antibiotikum aufrechtzuerhalten. Zu diesem Zweck verwendete ich gespaltene Inteine, um funktionelle Enzyme voller Länge zu rekonstruieren, die als zwei dysfunktionelle Hälften jeweils auf einem Plasmid exprimiert werden. Diese Methode, die wir SiMPl nannten, ermöglicht die Aufrechterhaltung von zwei Plasmiden in Bakterien und Säugetierzellen unter Verwendung eines einzigen Antibiotikums, das zwischen Kanamycin, Chloramphenicol, Ampicillin, Hygromycin und Puromycin gewählt wird.

Publications

Peer-reviwed:

The results on SiMPl plasmid toolbox (**Section 2.3.**) have been reported in:

Palanisamy N, Degen A, Morath A, Ballestin JB, Juraske C, Öztürk MA, *et al*. Split intein-mediated selection of cells containing two plasmids using a single antibiotic. Nat Commun. 2019 Oct 31;10(1):1–15.

Under review:

The results on functional impairment of MinE-eYFP (**Section 2.2.**) have been reported in:

Palanisamy N, Öztürk MA, Ventura BD. C-terminal eYFP fusion impairs *Escherichia coli* MinE function. bioRxiv. 2020 Jan 10.

Table of contents

1. Introduction..... 1

1.1. *E. coli* Min system, mid-cell determination and chromosome segregation..... 1

1.1.1. Bacterial cell cycle..... 1

1.1.2. Bacterial chromosome segregation and cell division..... 1

1.1.3. *E. coli* MinD..... 2

1.1.4. *E. coli* MinC..... 4

1.1.5. *E. coli* MinE..... 5

1.1.6. Min oscillations..... 6

1.1.7. *E. coli* MinD binds to DNA..... 8

1.1.8. Residues in MinD involved in DNA binding..... 10

1.1.9. Visualization of Min proteins *in vivo* and *in vitro*..... 12

1.2. Stable maintenance of multiple plasmids in *E. coli* and inteins..... 13

1.2.1. Plasmid incompatibility..... 13

1.2.2. Maintenance of multiple plasmids in *E. coli* using single antibiotic..... 14

1.2.3. Inteins..... 15

1.3. Aim of my thesis..... 16

2. Results..... 18

2.1. DNA binding by the MinCD complex..... 18

2.1.1. MinC enhances the DNA-binding activity of MinD..... 18

2.1.2. ATP is needed for the DNA-binding activity of the MinCD proteins..... 19

2.1.3. Alternating copolymer formation by MinD and MinC is not needed for the DNA binding..... 20

2.1.4. G10 residue in MinC plays a role in the DNA-binding activity of MinC/MinD..... 21

2.1.5. MinC mutants bind to MinD as well as the MinC WT..... 23

2.1.6. DNA binding of the $MinC^{G10D}$ mutant is impaired electrostatically..... 24

2.1.7. Linker region of MinC plays a critical role in the DNA binding..... 27

2.1.8. FtsZ inhibits the DNA-binding ability of MinC/MinD..... 34

2.1.9. FtsZ interaction of $MinC^{G10P}$ is impaired..... 35

2.1.10. MinC N-terminal bZIP synthetic construct co-localizes with *E. coli* chromosome *in vivo*……... 38
2.2. MinE-eYFP fusion protein characterization……..... 41
2.2.1. Overexpression of $MinC^{G10D}$DE-eYFP in a Δ*minB* strain exhibits a lethal phenotype……. 41
2.2.2. *In vivo* complementation of mini-cell phenotype of a Δ*minB* strain by MinE-eYFP is impaired compared to untagged MinE……. 41
2.2.3. MinE-eYFP is vulnerable to aggregation……. 43
2.2.4. MinE-eYFP cannot dislodge MinC from MinD as well as untagged MinE.... 45
2.2.5. MinE-eYFP cannot dislodge MinD from the membrane as well as untagged MinE……. 46
2.2.6. MinE-eYFP is able to bind to MinD…..……... 47
2.2.7. Computational analysis of MinE-eYFP predicted reduced accessibility of membrane targeting sequence and R21 in MinE…….. 49
2.2.8. MinE-eYFP is not able to bind to the membrane as predicted computationally…… 50
2.2.9. MinE-eYFP dimerization interface is not affected as predicted computationally…… 51
2.3. SiMPl plasmid toolbox……... 53
2.3.1. SiMPl plasmid pair based on kanamycin……. 53
2.3.2. SiMPl plasmid pairs based on chloramphenicol and ampicillin…….. 57
2.3.3. SiMPl plasmid pairs based on hygromycin and puromycin…… 59
3. Discussion…….. 66
3.1. MinC linker plays a vital role in the DNA binding and FtsZ interaction……... 66
3.1.1. Appearance of a higher order DNA-bound structure not responsive to MinC in the EMSAs …….. 66
3.1.2. Co-polymer formation and DNA binding……..... 66
3.1.3. MinC G10 residue in the DNA binding and dimerization……... 67
3.1.4. MinC unstructured linker region and its importance in DNA binding..... 68
3.1.5. Role of MinC linker in MinC-FtsZ interaction……... 69

3.1.6. Co-localization of MinC$^{N\text{-}term+linker}$-bZIP-mRuby3 in the *E. coli* MG1655 Δ*minB* and *hu-gfp* strains…….. 70
3.1.7. Min system and chromosome segregation - what did we learn from my Ph.D. studies ……..... 71
3.2. Aggregation tendency, loss of direct MinE membrane interaction, inability to dislodge MinC and reduced accessibility of R21 residue in MinE-eYFP……... 73
3.2.1. Direct membrane interaction of MinE-eYFP……... 73
3.2.2. Displacement of MinC and MinD from the membrane by MinE-eYFP…….. 73
3.2.3. Aggregation tendency of MinE-eYFP……..... 74
3.3. SiMPl plasmid toolbox outperforms conventional method in maintaining two plasmids…….. 74
3.3.1. Splitting and reconstituting enzymes conferring resistance towards antibiotics using split inteins……..... 74
4. Outlook……. 76
4.1. *E. coli* MinCD proteins and chromosome segregation..... 76
4.1.1. Physiological role of DNA binding by MinCD proteins……. 76
4.1.2. Elucidation of DNA binding interface……. 76
4.2. Linker sequence composition and length in fusion proteins…….. 76
4.3. Expanding the SiMPl plasmid toolbox…….. 76
5. Materials and Methods…….. 77
5.1. Plasmid constructs and bacterial strains…… 77
5.2. Protein expression and purification……..... 78
5.3. Electrophoretic mobility shift assay (EMSA)…… 79
5.4. Liposome co-sedimentation assay……..... 79
5.5. Cell viability spot assay……..... 79
5.6. Fluorescence microscopy……... 80
5.7. Pull-down assay……..... 80
5.8. MinE membrane-binding assay……. 80

5.9. Size-exclusion chromatography……..... 81
5.10. Construction of SiMPl plasmids…….... 81
5.11. Transformation and selection of *E. coli* cells containing SiMPl plasmids……... 82
5.12. Plasmid isolation and agarose gel electrophoresis……... 82
5.13. Bacterial growth analysis……..... 82
5.14. Protein Cα-fluctuation analysis……... 83
5.15. Image analysis……. 83
6. List of plasmids constructed…….. 84
7. References…… 90

1. Introduction

1.1. E. coli Min system, mid-cell determination and chromosome segregation

For an organism to successfully thrive in an environment, it has to compete for nutrients and reproduce. Reproduction can be sexual or asexual. Prokaryotes like archaea and eubacteria, reproduce asexually through binary fission. In the asexual type of reproduction, the daughter cell carries the same genetic makeup as the parent cell. In such organisms, a new genotype/phenotype arises primarily due to the introduction of mutations and/or uptake of foreign genetic material from the environment. If protein(s) expressed from the foreign genetic material or the expression of mutant protein benefits the organism, either in their competition for nutrients and/or in their reproduction, they eventually get incorporated with the organism after several generations. During binary fission, the genome has to be evenly distributed between the daughter cells in order to be called a successful reproduction. Any mishap in this process will lead to reproductive failure and thereby the organism will eventually perish. In eukaryotic cell division, after the DNA replication, during anaphase, spindle fibres pull apart the sister chromatids towards the opposite poles thereby making sure that the genetic material is evenly distributed among the daughter cells.

1.1.1. Bacterial cell cycle

Unlike the eukaryotic cell, a unified mechanism for chromosome segregation does not exist in prokaryotes. Moreover, fast-growing prokaryotes like *Escherichia coli*, *Bacillus subtilis*, etc., when grown in a nutrient-rich media, undergoes multi-fork replication (new DNA replication starts even before the finish of the previous DNA replication) (2). In such cases, unlike the eukaryotes, DNA replication and segregation happens at the same time frame. The cell cycle of bacteria is broadly divided into three periods; 1) B-period, it is the time between the end of cell division and initiation of DNA replication (2). This period is similar to the G1 phase in eukaryotic cells. 2) C-period, which is for DNA replication (**Figure 1**) (2). This period is similar to the S phase in eukaryotic cells. 3) D-period, it is the time between the termination of DNA replication and completion of cell division (**Figure 1**) (2). Multi-fork replication happens when the bacterial doubling time gets shorter than the C-period (**Figure 1**) (2).

1.1.2. Bacterial chromosome segregation and cell division

In some bacteria, for e.g. *Caulobacter crescentus*, a dedicated chromosome segregation machinery has been identified (3), while in many bacteria it is still unclear how their chromosome is segregated. If cell division happens before the chromosome segregation, the

daughter cell will either carry a guillotined chromosome or lack the chromosome completely (anucleate). In either case, the daughter cell will not be viable. To tightly regulate chromosome segregation and cell division, bacteria have adopted several strategies. In *E. coli*, two systems namely Noc and Min systems, work in parallel, to place the division site near the mid-cell (4,5). Noc system consists of proteins like Noc (in *B. subtilis*) and SlmA (in *E. coli*) (4). SlmA binds to a specific sequence (SBS) on the chromosomal DNA and prevents the FtsZ polymerization (4). It has been shown that SlmA activity is enhanced several folds upon binding to the SBS (4).

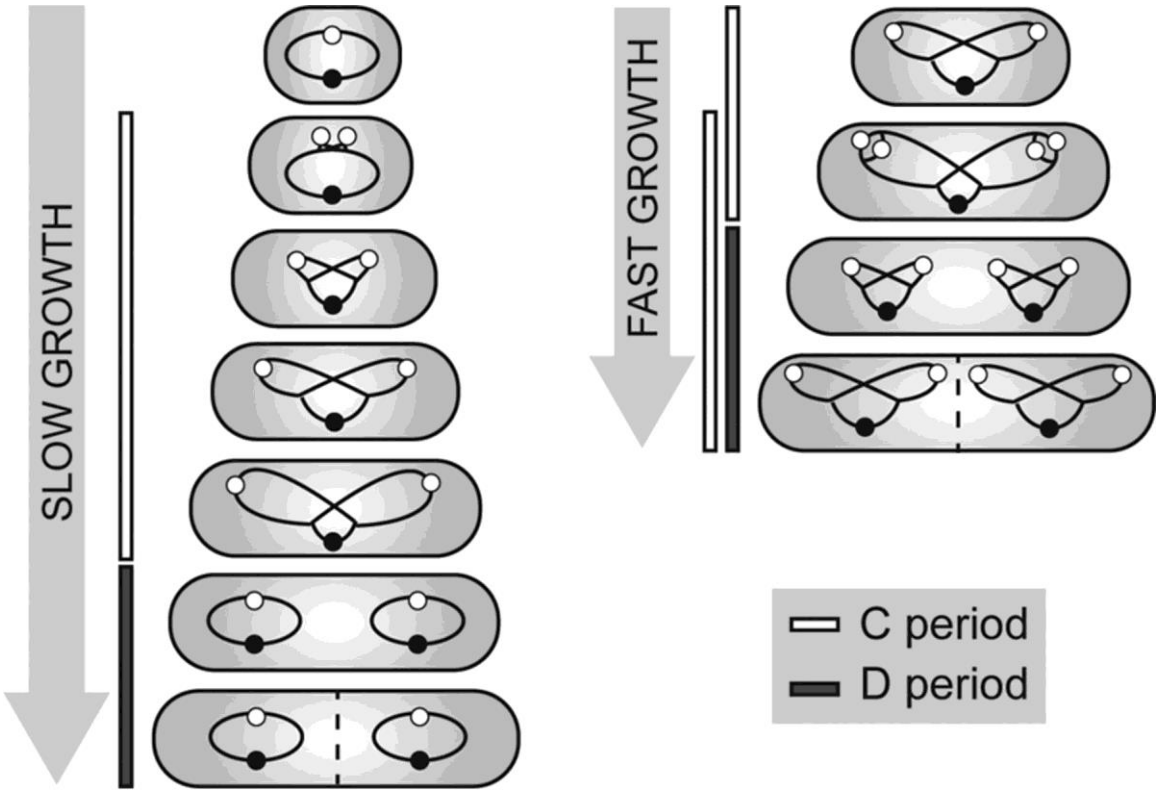

Figure 1. Chromosome replication in slow growing and fast growing bacterial cells. In the fast growing bacterial cells like *Escherichia coli*, multifork replication is observed. C period = time taken from the start to end of chromosome replication. D period = time taken from the end of chromosome replication till the end of cell division. Image was taken from Böhm *et al*. (6) under a Creative Commons Attribution 4.0 International License.

1.1.3. E. coli MinD

Escherichia coli (*E. coli*) Min system consists of three proteins namely, MinC, MinD, and MinE. The Min proteins are encoded by the *minB* operon (7,8). The Min system has been extensively studied for its role in the mid-cell determination in *E. coli* (8). MinD, a ParA homolog, possesses a deviant Walker A motif with inherent weak ATPase activity (10). The Walker A motif consists of amino acids GXXXXGKT/S, where X can be any one of the 20

canonical amino acids (10). In *Ec*MinD (*E. coli* MinD), residues from 10 to 17 constitute the Walker A motif. Lysine at position 11 in *Ec*MinD preferentially interacts with ATP ribonucleotide but also can interact with GTP ribonucleotide (11,12). ATP hydrolysis by MinD is mediated *via* two sequential steps; 1) activation of a nearby water molecule and 2) the transfer of the electron pair to the γ-phosphate of ATP while maintaining the transition state (13). Aspartic acid at position 40 activates the nearby water molecule and transfers the electron pair, while residues lysine and asparagine at positions 11 and 45, respectively, maintain the transition state (13,14).

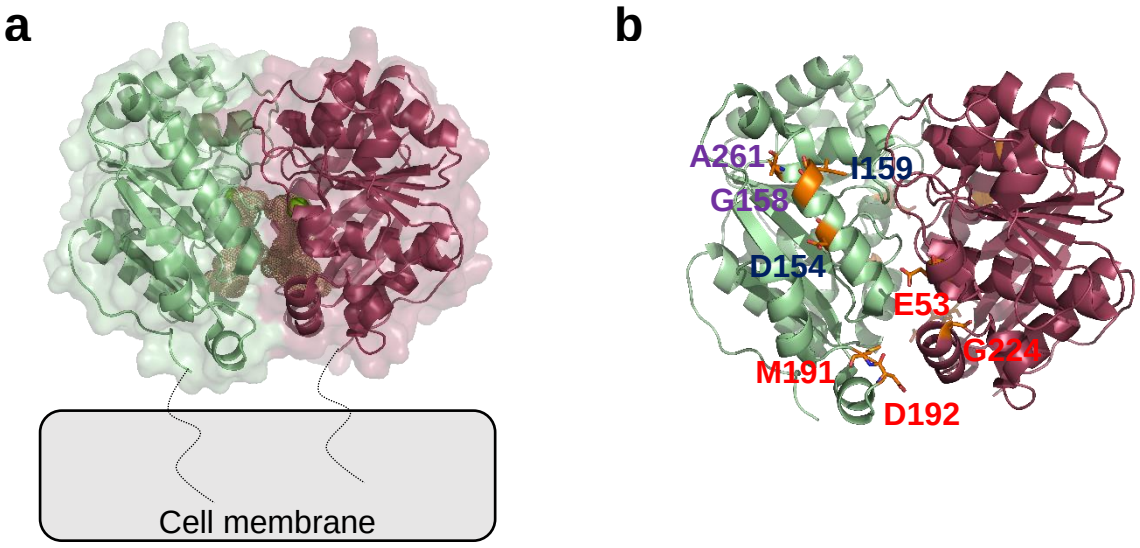

Figure 2. Structure of *Escherichia coli* MinD and residues important for interaction with MinC and MinE. a) Crystal structure of dimeric *E. coli* MinD$^{D40A\Delta10}$. Individual MinD monomers are coloured in pale green and raspberry. The membrane targeting sequence is represented by a dotted line. ATP is represented as surface dots and magnesium is represented by a green sphere. b) Residues important for interaction with MinC, MinE, and MinC and MinE are indicated in purple, red and dark blue, respectively, and represented as sticks. Image was created using Pymol version 0.99. Crystal structure of PDB ID: 3q9l (12) was used in generating the image.

Apart from the inherent weak ATPase activity, MinD also possesses membrane-binding activity *via* its C-terminal membrane targeting sequence (MTS) (15). Although the membrane-binding activity is weak in its monomeric state, upon binding to ATP, MinD dimerizes, and the membrane-binding activity is enhanced (16). The deletion of 10 amino acids from the C-terminal of MinD abolishes the membrane-binding activity of MinD (called MinD$^{\Delta10}$) completely (15). Nevertheless, MinD$^{\Delta10}$ still can dimerize with the presence of ATP (15). In its monomeric state, K11 in MinD interacts with glutamic acid at position 146 and aspartic acid at position 152 electrostatically, and with serine at position 148 through the formation of a

hydrogen bond (11,13,14). Upon binding to ATP, the interactions of K11 with S148 and D152 were broken, and MinD now dimerizes through interactions of K11 with the α and γ phosphates of the neighboring ATP-bound MinD and *vice versa* (14). Replacing K11 with alanine abolishes the dimer formation of MinD (11). The crystal structure of $MinD^{D40A\Delta10}$ has been elucidated by Lutkenhaus *et al*. and is available in the protein data bank (PDB; https://www.rcsb.org/) with PDB ID: 3Q9L (12). **Figure 2** shows the crystal structure of *Ec*$MinD^{D40A\Delta10}$. With the presence of ATP, this MinD mutant remains as a dimer, yet it can neither bind to membrane nor hydrolyze the bound ATP (12).

1.1.4. E. coli MinC

E. coli MinC (*Ec*MinC) is a passenger of MinD and exists in an equilibrium between monomeric and dimeric states in the cytoplasm (17). MinC is recruited to the cell membrane through binding with MinD. MinC binding to MinD occurs only when the latter forms a dimer (11). MinC fully becomes dimeric when it binds with membrane-bound MinD (17). MinC contains two domains; N (also called Z)- and C (also called D)- terminal domains (18). The C-terminal domain of MinC binds to MinD (18). Both the N- and C-terminal domains of MinC inhibit FtsZ polymerization with varying levels of inhibition, and the N-terminal domain exhibits the strongest inhibition among the two domains (19). The N-terminal domain inhibits longitudinal interactions between FtsZ molecules within a protofilament and the C-terminal domain inhibits lateral interactions of FtsZ between the protofilaments (19). Lutkenhaus group has identified residues in the N-terminal domain of MinC (K9, G10, K35, A39, and F42) that interact with FtsZ (20,21). Camberg *et al.* has also recently identified two hotspots on MinC that interact with FtsZ; a cleft in the MinC N-terminal domain and a surface on the MinC C-terminal domain (22). The N- and C- terminal domains of *Ec*MinC are connected by an unstructured linker region rich in proline. A complete crystal structure of *Ec*MinC is not yet available albeit two separate studies have elucidated the structures of the N- and C-terminal domains separately and can be accessed with PDB IDs 4L1C (23) and 5XDM (24), respectively. Both the domains have been crystallized as a dimer separately, although dimerization of the N-terminal domain by domain swapping is still under controversy (**Figure 3**). The residues G42 and R44 (switch I) and residues I125 and E126 (switch II) of MinD bind and activate MinC (25).

1.1.5. E. coli MinE

E. coli MinE (*Ec*MinE) is a small protein (88 amino acids), yet has been found to be highly dynamic in nature (26). MinE enhances the ATPase activity of MinD with a 10-fold increase in the presence of anionic phospholipids (27). MinE possesses 3 functional units; 1) N-terminal cryptic membrane targeting sequence (MTS; residues 2-12), 2) anti-MinCD domain (residues 13-30), and 3) dimerization domain (residues 31-88) (28–31). The N-terminal cryptic MTS has been shown to aid in the direct membrane interaction of MinE (28). The direct membrane association of MinE is needed for Min oscillations and for the proper functioning of the Min system (28,32,33). Shih *et al*. postulated that this N-terminal cryptic MTS may play a role as a 'topology specificity factor' (28).

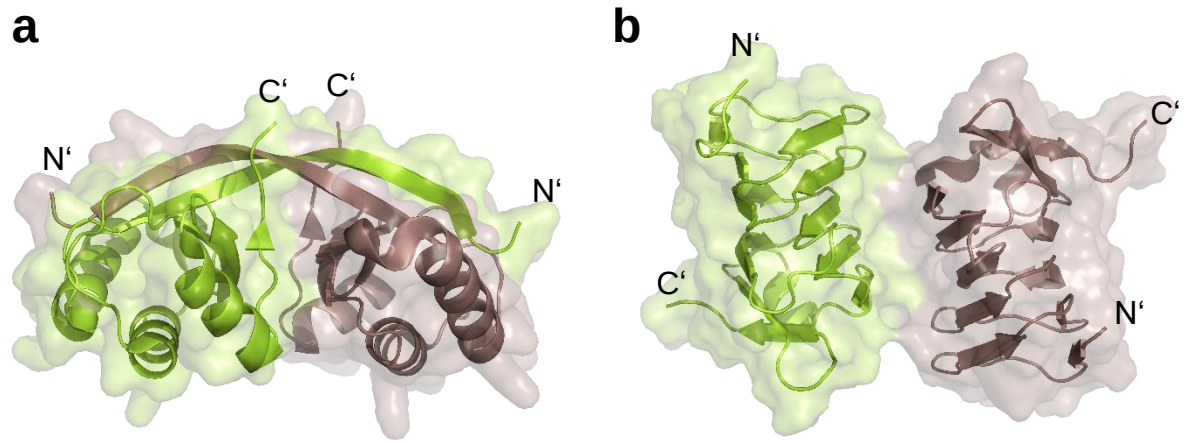

Figure 3. Structure of *Escherichia coli* MinC N- and C-termini domains. a) Crystal structure of dimeric *E. coli* MinC N-terminal domain. Dimerization happens *via* domain swapping of a β-sheet constituting of residues from 6 to 20. b) Crystal structure of dimeric *E. coli* MinC C-terminal domain. Image was created using Pymol version 0.99. Crystal structure of PDB IDs: 4l1c (23) and 5xdm (24) were used in generating the images.

*Ec*MinE exists in two structural conformations inside the cell; 6β-stranded and 4β-stranded conformations (32). Two plausible models were initially proposed for the two observed MinE conformations by the Lutkenhaus group (26,32). In the first model, both the conformations are in equilibrium and on binding with MinD the equilibrium shifts towards 4β-strand conformation. In the second model, MinD directly induces the 6β-strand to 4β-strand conformation like a switch (sensing model) (26). Increasing experimental evidence suggest the sensing model (26). In the 6β-strand conformation, cryptic MTS exists in two states; in one state, the MTS interacts with a β-sheet within MinE (closed state) (26). This β-sheet will later become a α-helix upon sensing MinD (26). In the other state, the MTS is released freely from the β-sheet (open state) (26). Upon the release of the N-terminal cryptic MTS (open state), and

on contacting MinD, the anti-MinCD domain in MinE gets stabilized into a α-helix (referred to as contact helix) which then enhances the ATPase activity of MinD (**Figure 4**) (26). More specifically, MinE dimer contacts the dimer interface of a MinD dimer, and the contact helix of MinE gets stabilized, and arginine at position 21 (a residue in the contact helix) contacts asparagine at position 45 in MinD thereby inducing the downstream cascade for the ATP hydrolysis in MinD (14). Although a MinD dimer has two binding sites for MinE, a study has shown that binding of MinE to one of the two sites is enough to stimulate the ATPase activity (14). Crystal structures of anti-MinCD peptide and MinE lacking the MTS, bound to MinD, are available in the public domain and can be accessed with PDB IDs 3R9I and 3R9J, respectively (32). MinE dimerization domain confers topological specificity by preventing the growth of MinD/MinC complex on the membrane beyond the mid-cell (8,29). Shih *et al.* postulated that MinE dimerization domain (C-terminal domain) controls the topology specificity function of N-terminal domain by sequestration (28).

1.1.6. Min oscillations

The Min system forms an oscillatory pattern inside *E. coli* cells, from one pole to another, with a duration of under a minute for every oscillation (9). In detail, MinD upon binding to ATP dimerizes and because of the increased affinity for the membrane-binding, the dimers get recruited to the membrane (10,16,34,35). MinC has a liking for MinD dimers and they too get recruited to the membrane (9,36). The MinD/MinC complex stays on the membrane and continuously grows from one pole towards the mid-cell until upon encountering the E-ring (an assembly of MinE), which is formed close to the mid-cell (37). MinE transiently remains attached to membrane *via* its N-terminal MTS, and progressively dislodges MinD/MinC complex from the membrane by enhancing the ATPase activity of MinD (27,38). In the cytoplasm, ADP bound MinD exchanges ADP for ATP and gets recruited to the other pole where the concentration of MinE is the least. After completely dislodging the MinD/MinC complex from the ongoing pole, the E-ring dissociates and gets assembled again near to the mid-cell and now it moves towards the other pole where the new MinD/MinC complexes have been built up (39). *In vitro* studies have shown that for the Min oscillations, MinD and MinE are indispensable while MinC is dispensable (40,41). On average over time, the concentration of MinD/MinC forms polar gradients with maxima at the poles and minima near the mid-cell. FtsZ polymerization happens near the mid-cell where the concentration of MinC is minimum, and this polymerization further recruits the divisome complex necessary for the cell wall synthesis and septum formation (**Figure 6**) (42). Like *E. coli*, Gram (+) counterpart *B. subtilis*

also expresses MinD and MinC, but not MinE, form static gradients of MinD and MinC with concentrations being high at the poles (43). A study by Barák *et al*. has shown that *E. coli* Min proteins when exogenously expressed in *B. subtilis* resulted in cell elongation and *Ec*MinD can partly compensate for the function of *Bs*MinD (44). Another study by the same group has also shown the oscillation of *E. coli* Min proteins when exogenously expressed in *B. subtilis* (45). Further, another group has also showen the oscillation of *Neisseria gonorrhoeae* proteins when exogenously expressed in *E. coli* (46).

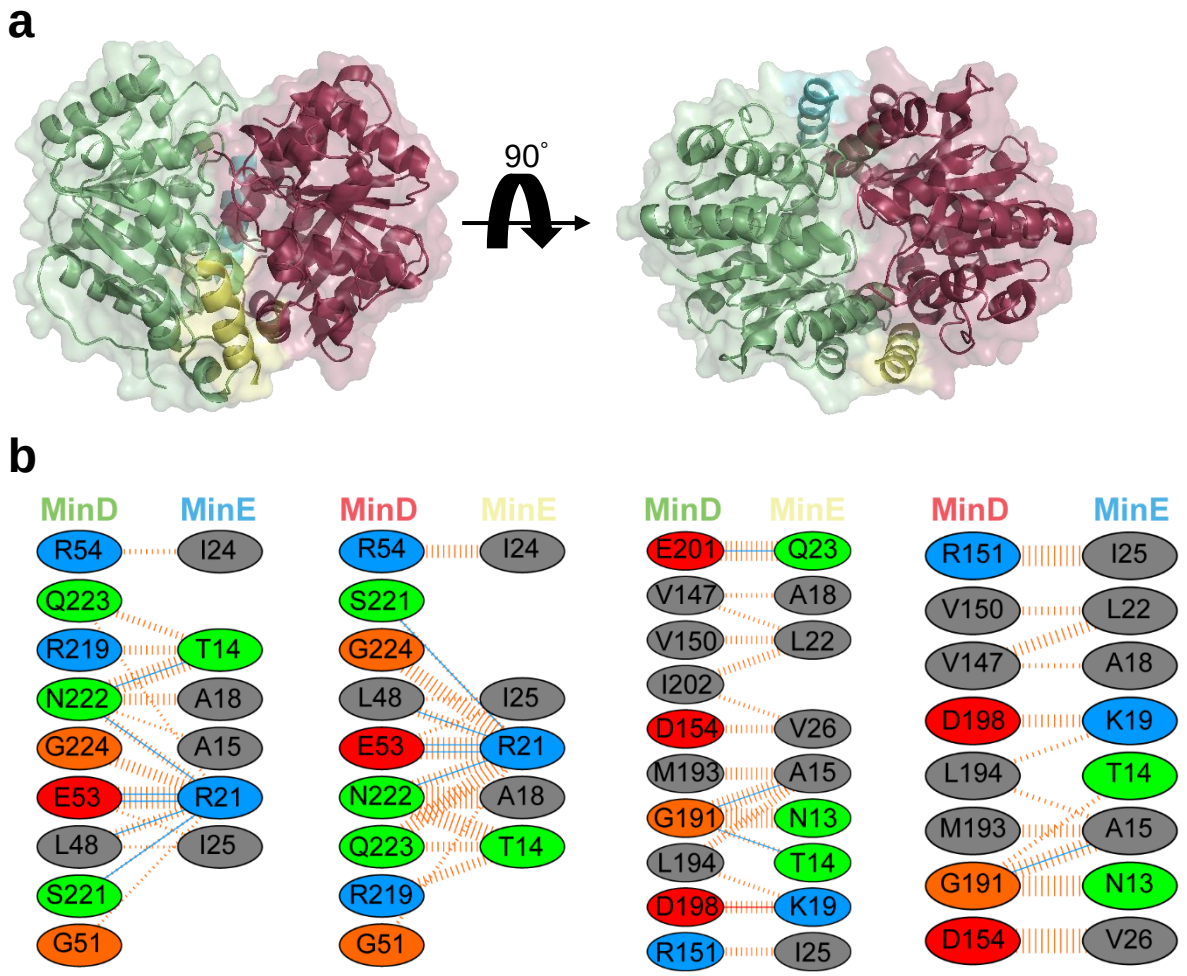

Figure 4. Structure of *Escherichia coli* MinD bound with MinE peptide (residues 12-31) and interaction profile of MinD and MinE. a) Crystal structure of dimeric *E. coli* MinD$^{D40A\Delta10}$ bound with MinE peptides. Individual MinD monomers are coloured in pale green and raspberry. Individual MinE peptides are coloured in pale yellow and cyan. b) Residues involved in the interaction between MinD and MinE peptide. MinD and MinE are coloured according to a). Image was created using Pymol version 0.99. Crystal structure of PDB ID: 3r9i (32) was used in generating the image. Protein-peptide interaction profile was generated using the PDBSUM webserver (http://www.ebi.ac.uk/thornton-srv/databases/cgi-bin/pdbsum/GetPage.pl?pdbcode=index.html). Red line = salt bridges, yellow line = disulphide bonds, blue line = hydrogen bonds, dashed orange line = non-bonded contacts.

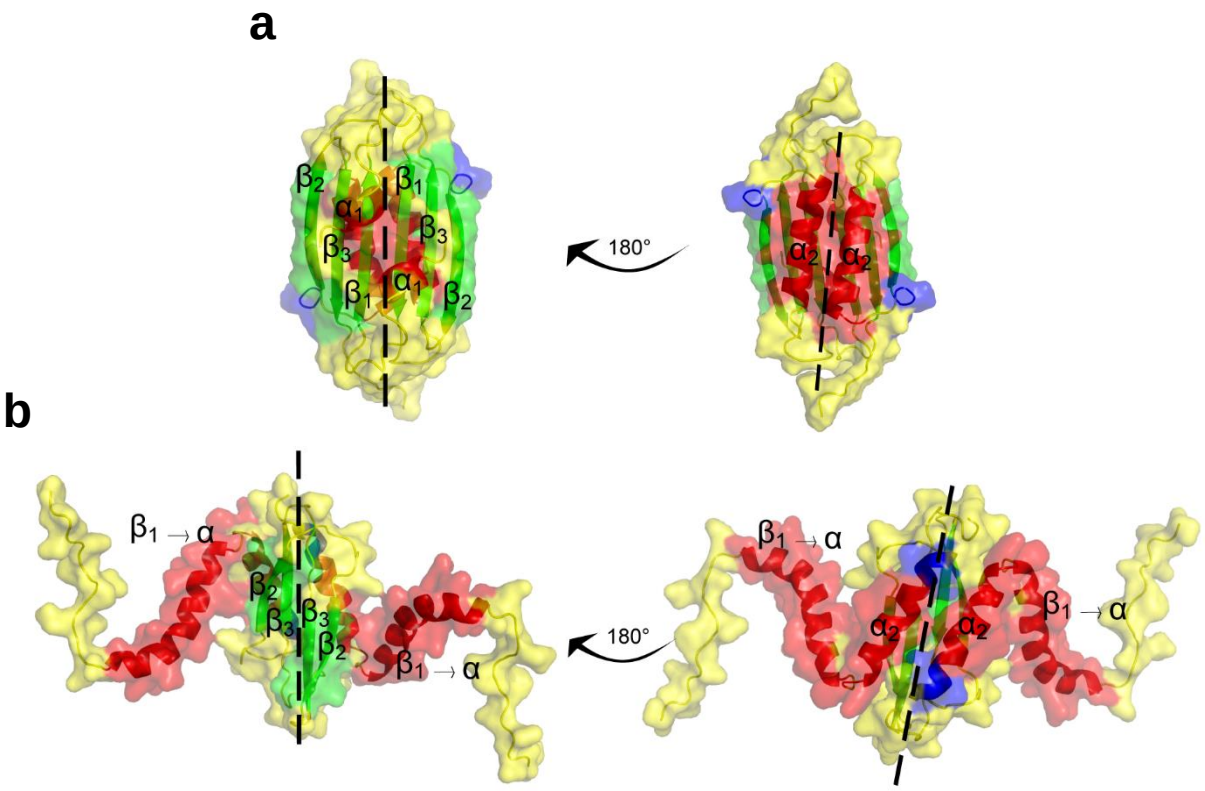

Figure 5. Modelled structure of *Escherichia coli* MinE in dimeric state. a) 6-β conformation. b) 4-β conformation. Protein structure modelling was done by Dr. Mehmet Ali Öztürk. β1 in the 6-β conformation converts to a α-helix in the 4-β conformation. Image was taken and modified from Palanisamy *et al*. (47) under a Creative Commons Attribution 4.0 International License.

1.1.7. E. coli MinD binds to DNA

Unlike their eukaryotic counterparts, a universal mechanism of chromosome segregation does not apply in prokaryotes (48). That being said, chromosome segregation in *E. coli* is poorly understood. It has been shown that daughter chromosomes segregate by mere force of repulsion created by the two massive negatively charged DNA (49,50). If this is true, then the chromosome segregation in *E. coli* is a passive process not requiring any energy. While in some prokaryotes, for example, *C. crescentus*, a dedicated system by Par proteins has been found (3). This system, on the other hand, utilizes energy for the proper segregation of chromosomes (3). By performing computer simulations, Di Ventura *et al*. has shown that entropic forces alone are not sufficient to achieve a full chromosome segregation in *E. coli* (51). Further, they found that full chromosome segregation is possible if DNA is transiently tethered to the membrane, provided the tethering happens in a gradient fashion with maxima near the poles (51). With further insights, they proposed that MinD could aid in chromosome segregation as MinD forms a similar distribution inside *E. coli* cells (51). By including MinD into their computer simulations, they observed full chromosome segregation (51). They further

showed by performing both *in vitro* and *in vivo* experiments that MinD can bind to DNA albeit very weakly with a K_d of 0.6 μM (51). Our group has proposed that MinD mediates the Brownian ratchet type of motion, which aids the sister chromosomes to segregate properly (**Figure 7**) (51). As a support to this proposal, Soj protein in *B. subtilis*, a homolog of *E. coli* MinD, has been shown to bind to DNA by another group (52). Di Ventura *et al*. have characterized several mutants of MinD, mostly residues at the C-terminal, and found that mutating positively charged arginine at position 219 to negatively charged aspartic acid impaired the DNA binding (51). Additionally, it was found that removing the MTS in MinD also impaired the DNA binding, but this loss in DNA binding was complemented by introducing a double mutation, in both cases where arginine was replaced by glutamic acid, one at position 251 and another at 254 ($MinD^{R2E\Delta10}$) (51). Expression of $MinD^{R219D}$ in *E. coli* cells showed impairment in both membrane-binding and binding to MinC (51). On the other hand, overexpression of $MinD^{R2E\Delta10}$ in *E. coli* cells resulted in its co-localization with the nucleoid (51).

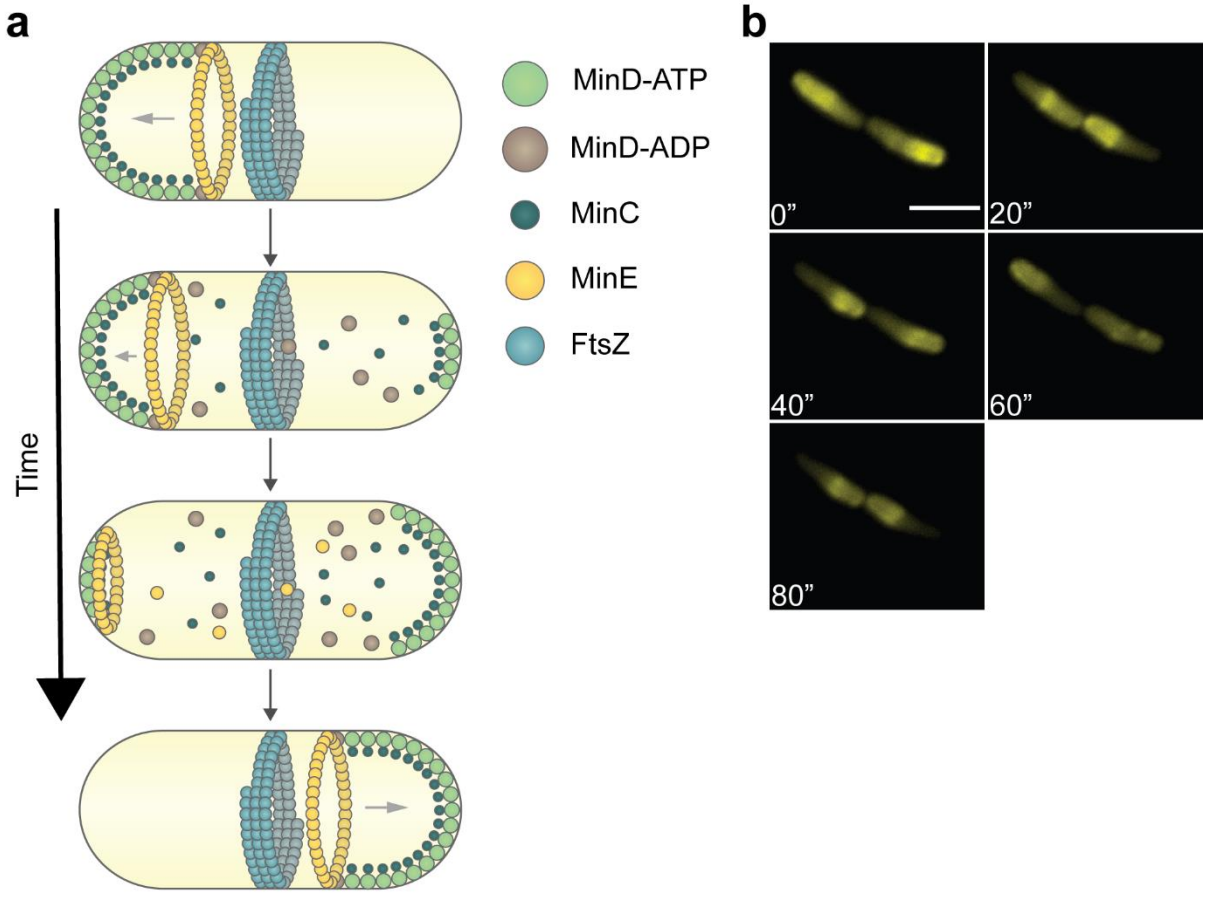

Figure 6. Oscillation of Min proteins from pole to pole in *Escherichia coli* cells. a) Schematics of Min oscillation and polymerization of FtsZ close to mid-cell. Image was taken from Zlir'a under a Creative Commons Attribution-

Share Alike 3.0 Unported license (CC BY-SA 3.0 Creative Commons license) (https://commons.wikimedia.org/wiki/File:MinCDE.svg). The image has been modified from the original version. b) Time-lapse fluorescence microscopy images showing the Min oscillations. *minB* operon was cloned between the *SacI* and *HindIII* restriction sites in pBAD33 vector. *eyfp* was fused downstream to MinE with 'GSGGG' linker. Scale bar = 3 μm.

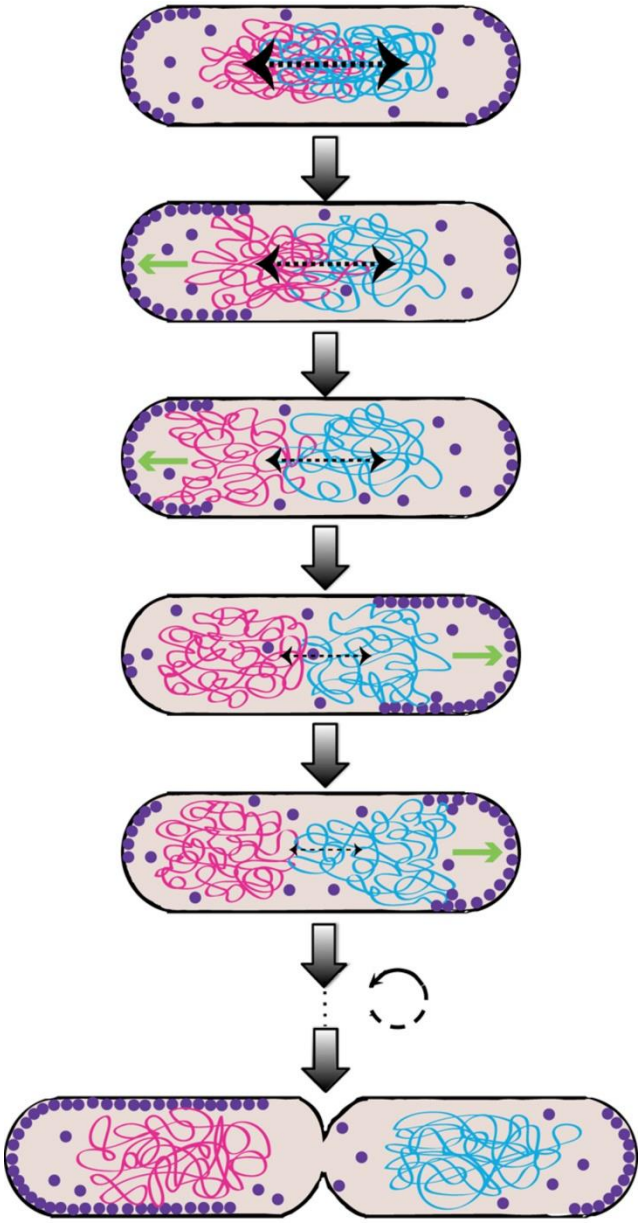

Figure 7. Proposed model of *Escherichia coli* MinD aiding in chromosome segregation. Image was taken from Di Ventura *et al*. (51) under the Creative Commons Attribution CC BY 4.0 License. During chromosome replication, due to force of repulsion (represented by dotted line with arrows), the chromosomes move to the opposite poles. As the distance between the chromosomes increase, the force of repulsion decreases. And, MinD aids in the complete chromosome segregation in the end.

1.1.8. Residues in MinD involved in DNA binding

A former Ph.D. student in our lab (Dr. Linda Klauss) continued studying *E. coli* MinD, in order to identify the residues in MinD that directly or indirectly interact with DNA (1). She created a small library of MinD mutants (single and double mutations), where positively charged amino acids found in the N-terminal part of MinD have been replaced with negatively

charged amino acids (**Figure 8**) (1). Using this library, by performing EMSA experiments she found that double mutants namely MinD$^{R54E/R55E}$, MinD$^{K78E/R79E}$, and MinD$^{R99E/K110E}$ had impaired DNA binding (1). By performing liposome co-sedimentation assays, she found that membrane binding was impaired in MinD$^{R54E/R55E}$ (1). By performing time-lapse fluorescence microscopy experiments, she found that Min oscillations were distorted in the MinD$^{R54E/R55E}$ and MinD$^{K78E/R79E}$ mutants (1). Finally, she found that MinD$^{R99E/K110E}$ mutant exhibited impaired DNA binding *in vivo* (1). In addition to these observations, by performing microarray experiments, she found that presence or absence of MinD did not affect either the transcriptome (transcription regulator) nor the proteome (protein regulator) in *E. coli* (1). By performing ChIP-Seq experiments, she found that MinD did not possess any sequence specificity (1). During the end phase of her Ph.D. thesis, she observed that MinC enhances the DNA-binding activity of MinD (1).

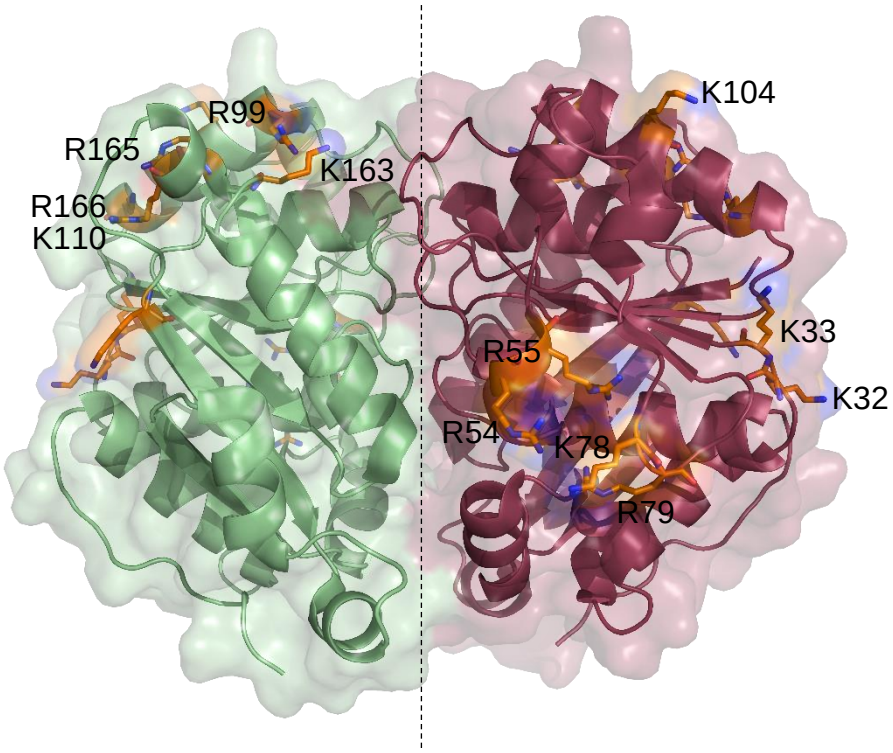

Figure 8. *Escherichia coli* MinD mutant library studied by Dr. Linda Klauss (1). Individual MinD monomers are coloured in pale green and raspberry. Monomers are separated by a dotted line. Residues mutated have been indicated and have been represented as sticks in the image. Image was created using Pymol version 0.99. Crystal structure of PDB ID: 3q9l (12) was used in generating the image.

1.1.9. Visualization of Min proteins in vivo and in vitro

The discovery of fluorescent proteins and their application in the biology field has brought us vast information about several biological processes, which otherwise would not have been possible (53). In the 1990's, Dr. Martin Chalfie showed for the first time that desired protein can be visualized *in vivo* by tagging the protein of interest with GFP (53). **Figure 9a** shows the crystal structure of GFP. Since then, a vast development has occurred in the field of fluorescent proteins. Now, we have fluorescent proteins having emissions covering the entire visible spectral range (**Figure 9b**) (54,55). While immunofluorescence studies using fixed cells provide information about localization of the protein(s) inside a cell, fusing a protein with GFP (green fluorescent protein) gives real-time dynamics of the protein (37). Further, GFP being relatively small (~27 kDa), in most cases, does not interfere with the protein function to which GFP is fused too (56,57). The oscillatory behavior of *E.coli* Min proteins was first observed by fusing GFP to MinD (9). The formation of E-ring close to the mid-cell in *E. coli* was observed by tagging *Ec*MinE with GFP (58). Further, using MinE-GFP, it was shown that the E-ring structure is highly dynamic (39). All these observations were made possible by the availability of fluorescent proteins. However, the problem arises if the GFP position in the fusion protein was wrongly assigned: for instance, the N-terminal fusion of GFP might impair the function of desired protein while C-terminal fusion of GFP to the same protein might not affect the function (59–61). Also, in some cases, GFP in the fusion protein brings unexpected changes to the desired protein and impairs the latter's function (62). Prior knowledge about protein-protein or protein-membrane interactions of the desired protein will suggest whether the desired protein has to be N- or C- terminally fused to the fluorescent protein. The C-terminal of *Ec*MinD interacts with the cell membrane. By fusing a fluorescent protein to the C-terminal of *Ec*MinD, the interaction between MinD and membrane is impaired thereby also impairing the MinD function. Similarly, the C-terminal of *Ec*MinC interacts with *Ec*MinD. By fusing a fluorescent protein to the C-terminal of *Ec*MinC, the interaction between *Ec*MinC and *Ec*MinD is impaired. To overcome the drawbacks of fluorescent protein fusions, thiol-reactive dyes are used to label the desired protein provided the desired protein contain accessible cysteine residue (63). Several commercial kits are available for *in vitro* labeling of proteins albeit the labelling efficiency still remains low. Using MinE labeled at cysteine residue 51 with Alexa647-maleimide and MinD labeled at cysteine residue 52 with Bodipy FL-maleimide, Schwille *et al.* showed that Min proteins form planar surface waves on a flat membrane *in vitro* (41).

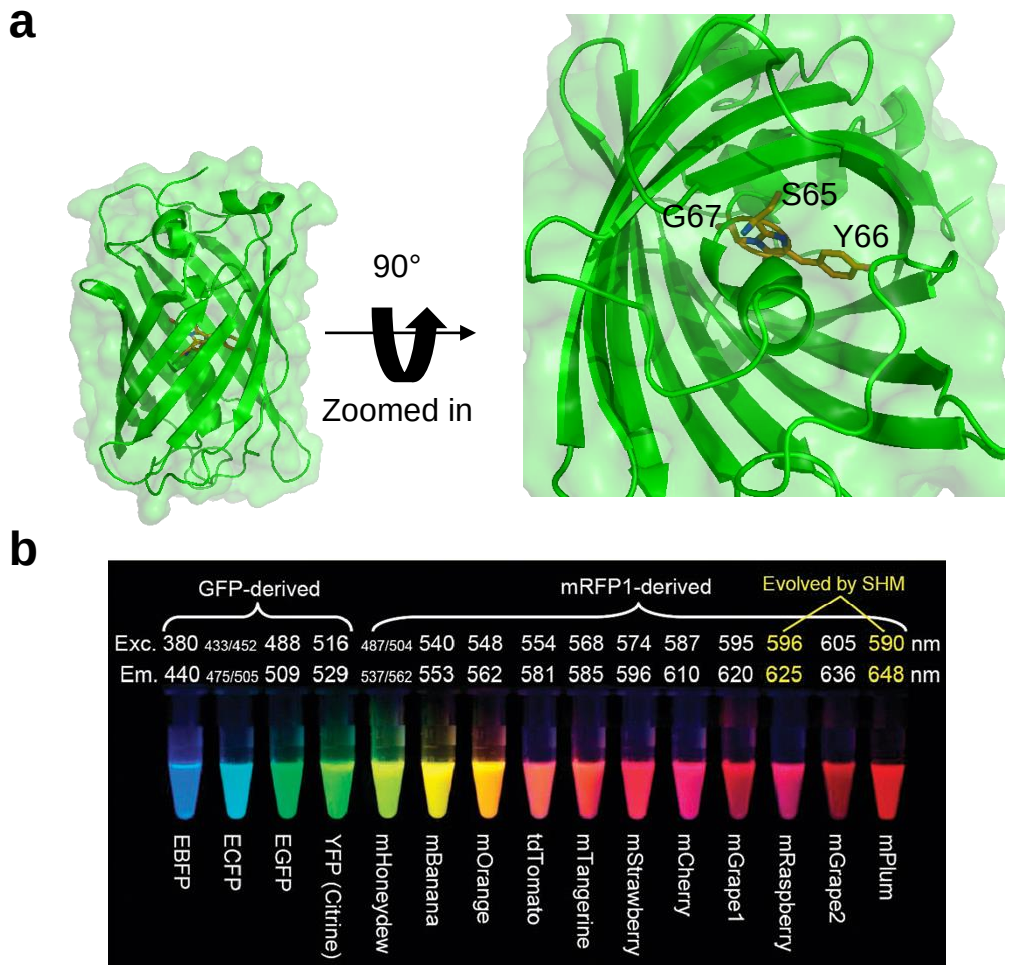

Figure 9. Green fluorescent protein (GFP) and monomeric red fluorescent protein (mRFP1), and their derivatives (54,55). a) Crystal structure of recombinant GFP WT. Fluorophore in GFP consists of amino acids serine (position 65), tyrosine (position 66) and glycine (position 67) which have been indicated in the figure and have sticks representation. Image was created using Pymol version 0.99. Crystal structure of PDB ID: 1gfl (64) was used in generating the image. b) Derivatives of GFP and mRFP1. GFP is from *Aequorea* spp. and mRFP1 is from *Discosoma* spp. Exc. = excitation wavelength. Em. = emission wavelength. SHM = somatic hypermutation. Image was taken from Dr. Roger Y. Tsien, Nobel Lecture, 8 December 2008. © The Nobel Foundation. Link: https://www.nobelprize.org/uploads/2018/06/tsien_lecture.pdf

1.2. Stable maintenance of multiple plasmids in E. coli and inteins

1.2.1. Plasmid incompatibility

E. coli has been extensively used in many aspects of research, including, but not limited to, plasmid propagation, protein expression, and purification, molecular cloning, industrial biotransformation and in synthetic biology. The number of plasmids to be maintained in *E. coli* requires equal numbers of antibiotics for selection. The available number of useable antibiotics and the origins of replication limits the number of plasmids to be maintained in *E. coli*.

Currently, the plasmids used in *E. coli* are broadly classified into three groups, namely, incompatible groups A, B and C (**Table 1**). Plasmids belonging to the same group cannot be stably maintained together in any *E. coli* strain without any selection pressure (65–68). A study by Velappan *et al*. has shown that this dogma is not absolute (69). For complex metabolic engineering, a situation arises such that multiple plasmids are needed to be maintained in *E. coli* at the cost of having an equal number of antibiotics, which impose a huge negative impact on the bacterial growth and the protein expression. Needless to say, the additional antibiotics also impose a huge cost on the product production.

Table 1. General information about commonly used plasmid vectors

Common vectors	Copy number§	ORI (origin of replication)	Incompatibility group	Control
pUC	~500-700	pMB1 (derivative)	A	Relaxed
pBR322	~15-20	pMB1	A	Relaxed
pET	~15-20	pBR322	A	Relaxed
pGEX	~15-20	pBR322	A	Relaxed
pColE1	~15-20	ColE1	A	Relaxed
pR6K	~15-20	R6K*	C	Stringent
pACYC	~10	p15A	B	Relaxed
pSC101	~5	pSC101	C	Stringent
pBluescript	~300-500	ColE1 (derivative) and F1†	A	Relaxed
pGEM	~300-500	pUC and F1†	A	Relaxed

§ = copy number also depends on other factors, * = needs *pir* for replication (70), † = F1 ORI is for replication and packaging of ssDNA (phagemid). Data taken from Kendall Morgan. Plasmids 101: Origin of Replication. Link: https://blog.addgene.org/plasmid-101-origin-of-replication. Posted on 6 Feb 2014. Accesses on 23 Feb 2020. Used with permission from Addgene.

1.2.2. Maintenance of multiple plasmids in E. coli using single antibiotic

The idea of stable maintenance of multiple plasmids using only one antibiotic is not new. Bennett Lab, from Rice University, the US, in 2012 showed the proof of principle for stably maintaining two and three plasmids in *E. coli* with just kanamycin as the selective marker (71). They have used a previously split aminoglycoside phosphotransferase (APT) enzyme that confers resistance towards kanamycin (72). They placed one half of the APT in

one plasmid and the other half in another plasmid, both these halves were under T7 or lac promoter (71). The expressed dysfunctional protein halves were brought together and become functional *via* a leucine zipper that was additionally added to both the APT halves (71,72). Only when both the plasmids are present in the same cell, *E. coli* can exhibit resistance towards kanamycin. While for maintaining the three plasmids, they used the same plasmid system as described for maintaining the two plasmids, while the third plasmid carried a gene encoding for T7 RNA polymerase that is needed to express the APT halves (**Figure 9**) (71). This method has several drawbacks in that the gene fragments encoding for the APT halves were cloned into the multiple cloning site (MCS) and their expression was under the inducible promoter. This prevents the usage of these plasmids as the gene of interest cannot be cloned into the MCS. Additionally, these plasmids also carried a gene conferring resistance to antibiotics other than kanamycin.

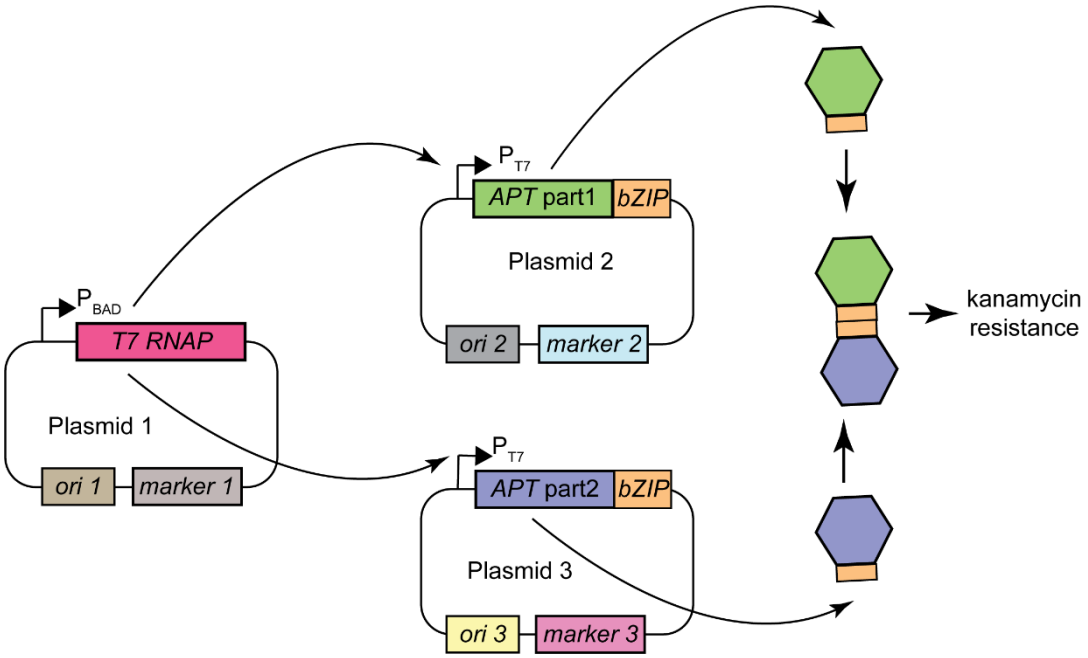

Figure 9. Schematics for maintenance of 3 plasmids using single antibiotic developed by Bennett Lab, Rice University, the US (71). *T7RNAP* = T7 RNA polymerase, *ori* = origin of replication, *APT* = aminoglycoside phosphotransferase, *marker* = resistance cassette other than *APT*, *bZIP* = leucine zipper.

1.2.3. Inteins

Unlike the complementation method developed by the Bennett lab, we wanted to fully reconstitute the dysfunctional protein halves into a full-length functional protein. For this purpose, we resorted to inteins. Inteins are protein sequences that cleave themselves out of a parent protein, finally yielding a spliced parent protein consisting of protein fragments found

upstream and downstream to the inteins (73,74). Inteins exist as a contiguous or split type naturally, and some inteins have also been split artificially (75,76). **Figure 10** shows cis- and trans- splicing of proteins by contiguous and split inteins, respectively. Using genome sequences, nearly 500 inteins have been identified so far (77). For a complete list, see Intein Database (http://www.biocenter.helsinki.fi/bi/iwai/InBase/tools.neb.com/inbase/index.html) (77).

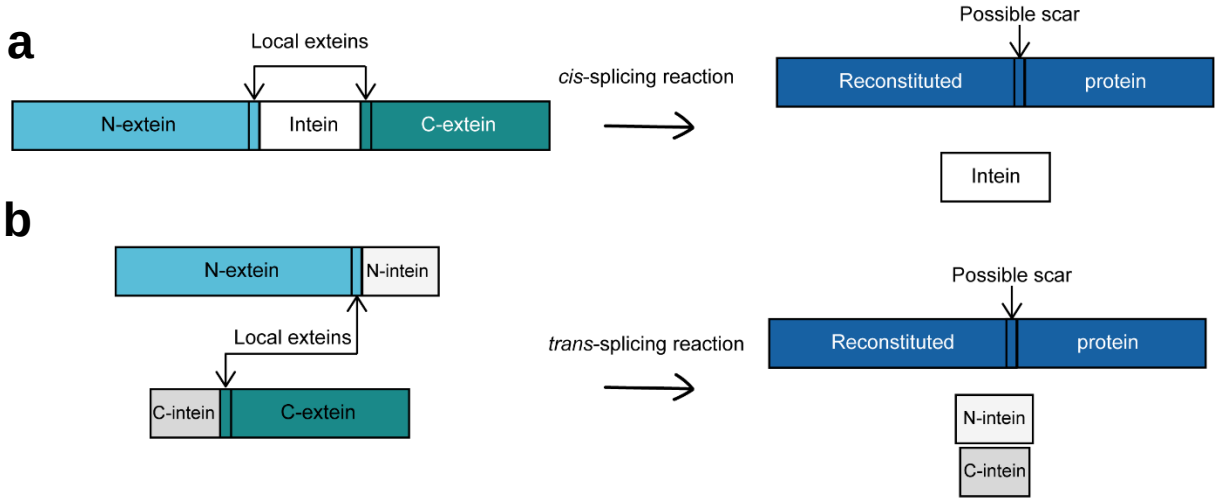

Figure 10. Schematics of contiguous (**a**) and split (**b**) inteins showing *cis*- and *trans*- splicing of proteins, respectively. Local exteins constitute amino acids 'SGY' and 'SSS' in the -3, -2, -1 and +1, +2, +3 positions, respectively, corresponding to the intein region. Local exteins (scar) remain in the final reconstituted protein. Image was created and kindly provided by Prof. Dr. Barbara Di Ventura.

1.3. Aim of my thesis

Aim 1: In context with the enhanced DNA-binding activity by the *E. coli* MinCD proteins, I continued my Ph.D. thesis from Dr. Klauss's work (1). I wanted to identify the residues in MinC that either directly or indirectly interact with DNA. To this end, I wanted to create a library of MinC point mutants and test them for their DNA-binding activity. But, unlike Dr. Klauss's strategy, I wanted to go for a rational approach, useing computational tools to predict the potential residues involved in DNA binding. Finally, I wanted to further test the MinC mutants, both *in vitro* and *in vivo*, to study the role of MinC and MinD in chromosome segregation in *E. coli*.

Aim 2: During the course of my Ph.D. study, I observed that MinE-eYFP fusion protein cannot complement the Δ*minB* phenotype in *E. coli* as well as untagged MinE. Earlier studies by de Boer *et al*. showed that MinE-GFP is functionally impaired, but the mechanism behind

the functional impairment of the fusion protein was not known (37,58). I wanted to study how fusing a fluorescent protein downstream of MinE affects its function.

Aim 3: Since in microbiology we often need to transform bacteria with two plasmids, I thought it would be advantageous to have a way to use a single antibiotic to maintain two plasmids in the cells. To this aim, I set up to develop a plasmid tool based on split inteins as a means to reconstitute enzymes that confer resistance towards antibiotics, which I would express as two dysfunctional halves from the two plasmids. Importantly, I planned to adopt a computational strategy to find the location where to split the enzymes.

2. Results

2.1. DNA binding by the MinCD complex

2.1.1. MinC enhances the DNA-binding activity of MinD

Electrophoretic mobility shift assay (EMSA) experiments performed by Dr. Linda Klauss showed that MinC enhances the DNA-binding activity of MinD, and the concentration of MinD is the limiting factor in the reaction mixture. To validate her observations, EMSA experiments were performed under exactly the same conditions as done by her before. MinD was incubated alone, or co-incubated with varying concentration of MinC (0 – 4 μM), and hex-labelled DNA in a buffer containing ATP and magnesium. With either only MinD (4 μM) or MinC (4 μM), no DNA binding was observed (**Figure 11**). While in the presence of MinD (4 μM) and with as low as 1 μM MinC concentration, DNA binding was observed (**Figure 11**). When MinD and MinC, each at 4 μM, >90 % of DNA was found to be bound (**Figure 11**).

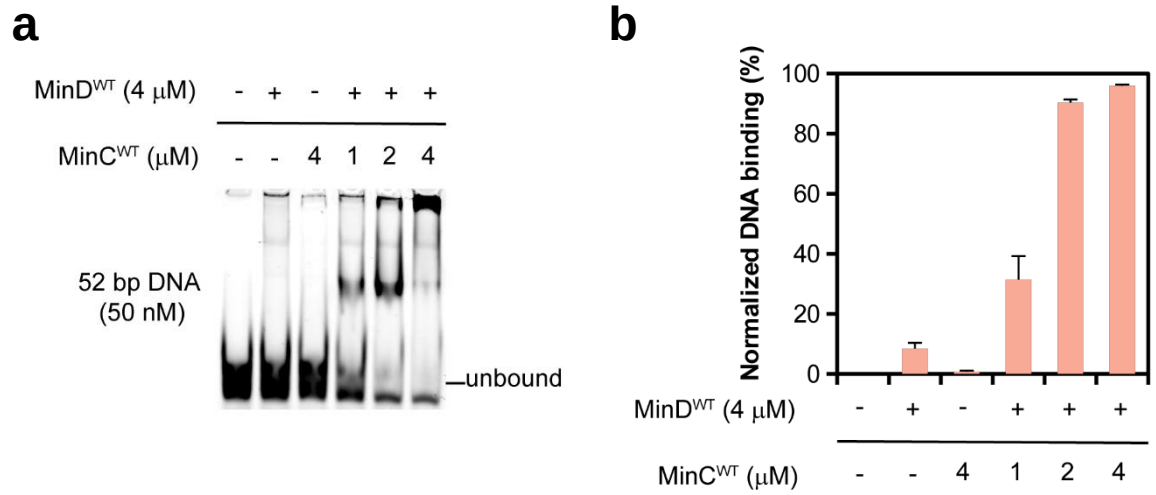

Figure 11. DNA-binding activity of MinD with increasing concentration of MinC and fixed concentration of MinD. MinD (4 μM) was incubated alone, or with varying concentration of MinC (0 – 4 μM), and 50 nM of hex-labelled DNA (52 bp) in a buffer containing 1 mM ATP and 5 mM $MgCl_2$. a) Representative native-PAGE (EMSA) gel showing DNA-binding activity of MinD with increasing MinC concentration. b) Bar plot showing quantification of DNA binding (in %) of MinD with increasing MinC concentration. Experiments were performed thrice and mean±S.E.M. is plotted in the graph.

The EMSA experiments were repeated again, but this time, the concentration of MinC was kept fixed at 4 μM, while varying the MinD concentration (0 – 4 μM). MinC was incubated alone, or co-incubated with varying concentration of MinD (0 – 4 μM), and hex-labelled DNA in a buffer containing ATP and magnesium. Like observed before, with either 4 μM MinC or 4 μM MinD, no DNA binding was observed (**Figure 12**). But, unlike before, no DNA binding

was observed until 2 μM MinD concentration (**Figure 12**). DNA binding was observed only when 4 μM of MinD was used (**Figure 12**). These observations suggest that the DNA-binding activity of MinD is enhanced by MinC (or the *vice versa*) and the limiting factor in the DNA-binding ability of MinCD complex is the MinD concentration.

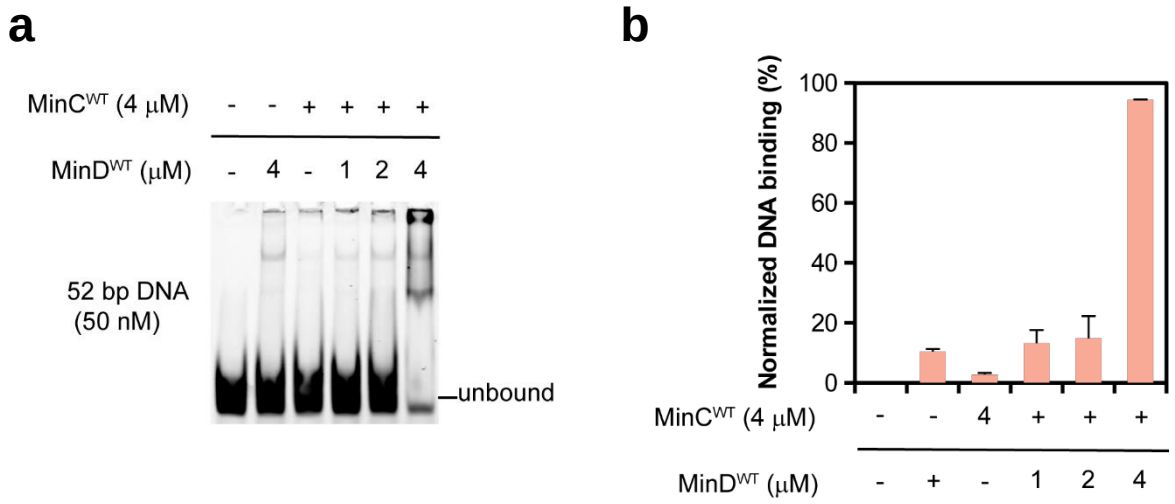

Figure 12. DNA-binding activity of MinD with fixed concentration of MinC and increasing concentration of MinD. MinC (4 μM) was incubated alone, or with varying concentration of MinD (0 – 4 μM), and 50 nM of hex-labelled DNA (52 bp) in a buffer containing 1 mM ATP and 5 mM $MgCl_2$. a) Representative native-PAGE (EMSA) gel showing DNA-binding activity of MinD with fixed concentration of MinC and increasing MinD concentration. b) Bar plot showing quantification of DNA binding (in %) of MinD with fixed concentration of MinC and increasing MinD concentration. Experiments were performed thrice and mean±S.E.M. is plotted in the graph.

2.1.2. ATP is needed for the DNA-binding activity of the MinCD proteins

MinD dimerizes with the presence of ATP. MinC binds to MinD only when the latter dimerizes. An earlier study by Di Ventura *et al.* has shown by EMSA experiments that MinD binds to DNA either in presence of ATP or in absence of any nucleotide, and no DNA binding was observed with the presence of ADP (51). The observed DNA-binding activity of MinCD proteins can be mediated by dimeric MinC and monomeric MinD, binding to DNA separately but in close proximity to one another, or dimeric MinC and dimeric MinD binding to DNA in close proximity to one another and/or together. To understand this, EMSA experiments were performed with the presence of either ADP or ATP, or the absence of any nucleotide. MinD (4 μM) was co-incubated with MinC (4 μM) in a buffer containing either 1 mM ADP or ATP or no nucleotide and ran on a native-PAGE gel. With the presence of ADP or the absence of any nucleotide, only a meager DNA binding was observed (≤20 %), which was more or less the background level (**Figure 13**). On the other hand, with the presence of ATP, the DNA binding

was enhanced up to 4-fold (**Figure 13**). These observations suggest that MinD dimerization is needed to see the enhancement in DNA binding with the presence of MinC.

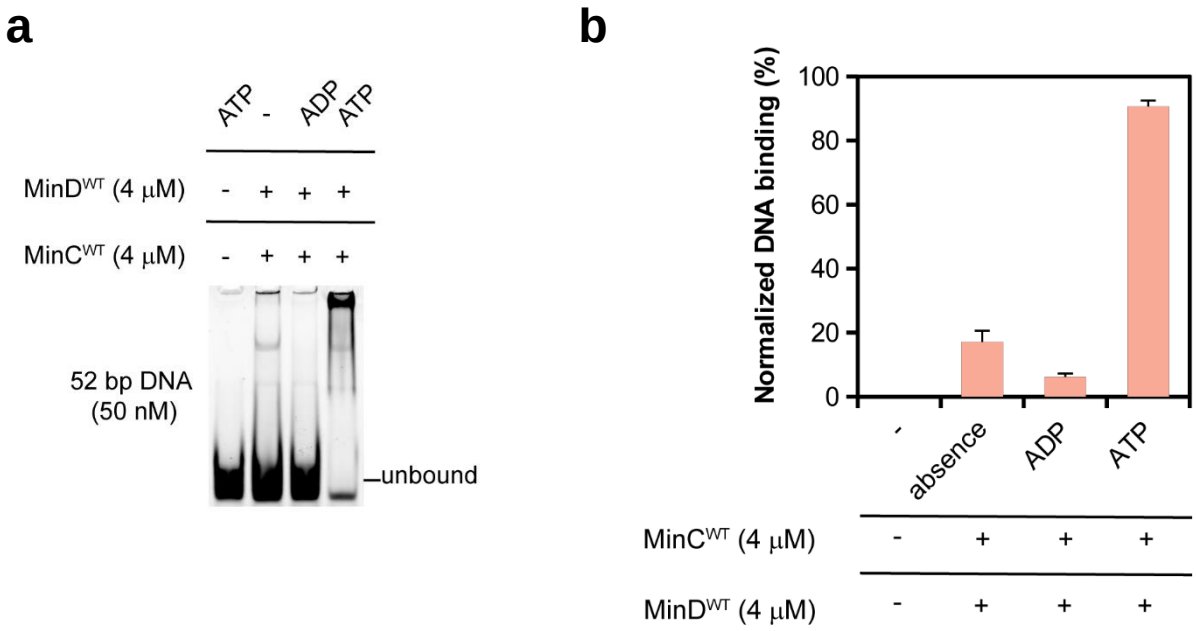

Figure 13. DNA-binding activity of MinCD with presence of ADP or ATP and absence of any nucleotide. MinD (4 μM) was co-incubated with MinC (4 μM) and 50 nM of hex-labelled DNA (52 bp) in a buffer containing 5 mM $MgCl_2$, with presence of 1 mM ADP/ATP and absence of any nucleotide . a) Representative native-PAGE (EMSA) gel showing DNA-binding activity of MinCD with presence of 1 mM ADP/ATP and absence of any nucleotide. b) Bar plot showing quantification of DNA binding (in %) of MinCD with presence of 1 mM ADP/ATP and absence of any nucleotide. Experiments were performed thrice and mean±S.E.M. is plotted in the graph.

2.1.3. Alternating copolymer formation by MinD and MinC is not needed for the DNA binding

MinC dimer binds to the dimerization interface of a MinD dimer (11). Based on the observations made before, the question still remains whether MinD and MinC form alternating copolymers to be able to bind DNA or the co-polymer architecture of the MinCD complex is irrelevant for the DNA binding. To study this, EMSA experiments were performed with fixed MinD (4 μM) and MinC (4 μM) concentrations in a buffer containing hex-labelled DNA, ATP and magnesium, and adding an excess of a MinC mutant ($MinC^{R133A}$). The R133A mutant of MinC, in excess, is known to form heterodimers with MinC WT, but this mutant is unable to bind with MinD (78). It was observed that even at 16 μM $MinC^{R133A}$ concentration, the DNA binding was not affected (**Figure 14**). Taken this observation, alternating copolymers of MinD/MinC are not needed for the DNA binding.

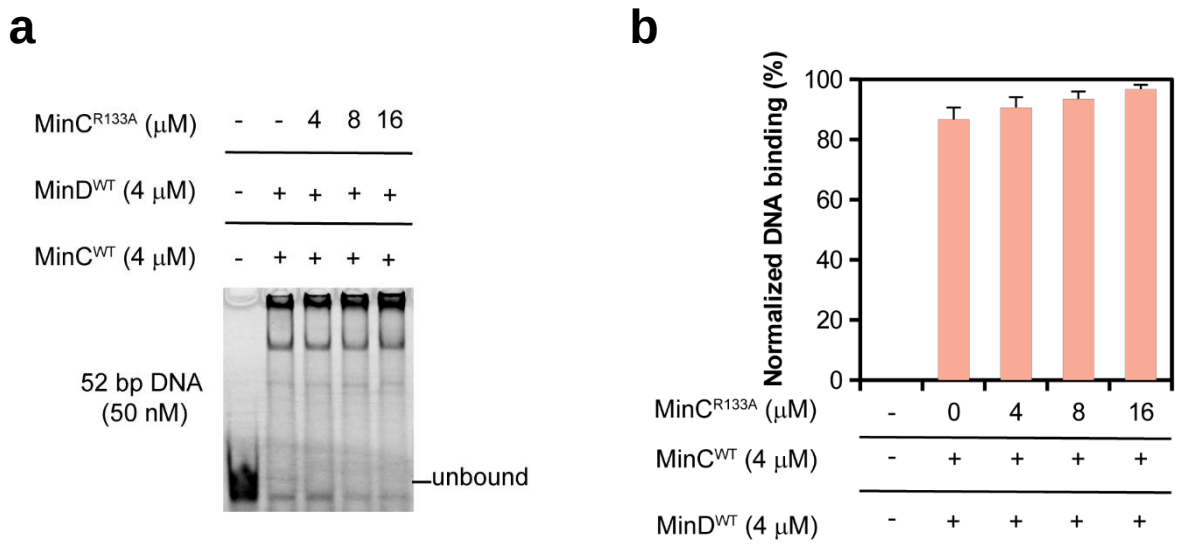

Figure 14. MinC/MinD alternating copolymers are not needed for the DNA-binding. MinD (4 μM) was co-incubated with MinC (4 μM) and 50 nM of hex-labelled DNA (52 bp) in a buffer containing 5 mM $MgCl_2$ and 1 mM ATP, and with increasing concentration of MinC^{R133A}. a) Representative native-PAGE (EMSA) gel showing DNA-binding activity of MinCD with increasing concentration of MinC^{R133A}. b) Bar plot showing quantification of DNA binding (in %) of MinCD with increasing concentration of MinC^{R133A}. Experiments were performed thrice and mean±S.E.M. is plotted in the graph.

2.1.4. G10 residue in MinC plays a role in the DNA-binding activity of MinC/MinD

Now I know that both MinC and MinD are needed for the DNA binding, I studied further to identify the residues in MinC and MinD that interact(s) with DNA. Instead of going for the random mutagenesis strategy, we used computational tools to predict the DNA-binding interface on MinC/MinD. Dr. Mehmet Ali Öztürk performed molecular docking of a short piece of double-stranded DNA with modeled MinC/MinD dimers. Initial docking analysis predicted G10 residue in MinC to interact with the DNA (**Figure 15**). Additionally, through evolutionary conservation studies, he predicted that K66 residue in MinC also plays a role in the DNA binding (**Figure 15**).

To validate the *in silico* predictions, MinC G10 mutants namely, G10A, G10D, G10P and G10R, and K66A were purified and EMSA experiments were performed. MinD (4 μM) was co-incubated with MinC (4 μM) WT or mutants and hex-labelled DNA in a buffer containing ATP and magnesium. It was found that the DNA-binding activity of G10A and G10P mutants were similar to that of the MinC WT (**Figure 16**). While DNA binding was impaired in the G10D mutant, DNA binding was enhanced, even higher than that of the MinC

WT, when the G10R mutant was used (**Figure 16**). The DNA binding was reduced, nearly half of what has been seen for the MinC WT, when the K66A mutant was used (**Figure 16**).

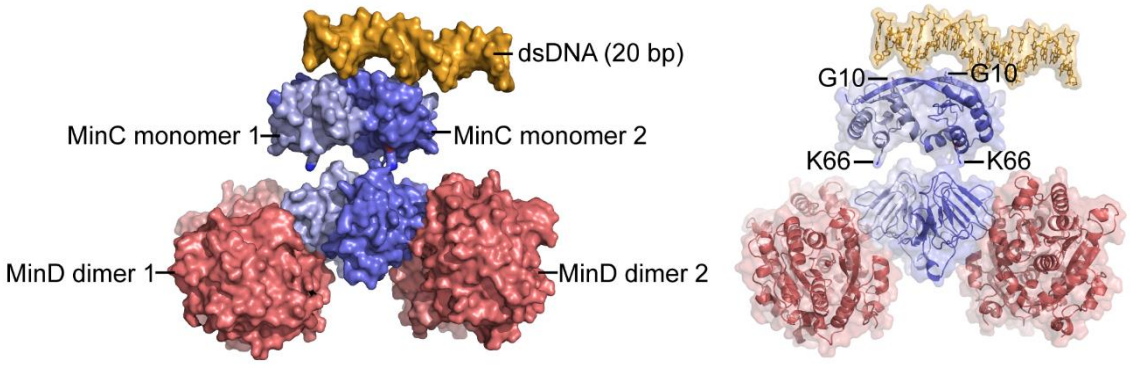

Figure 15. *In silico* docking of modelled MinC/MinD dimers with double stranded DNA. Image provided by Dr. Mehmet Ali Öztürk.

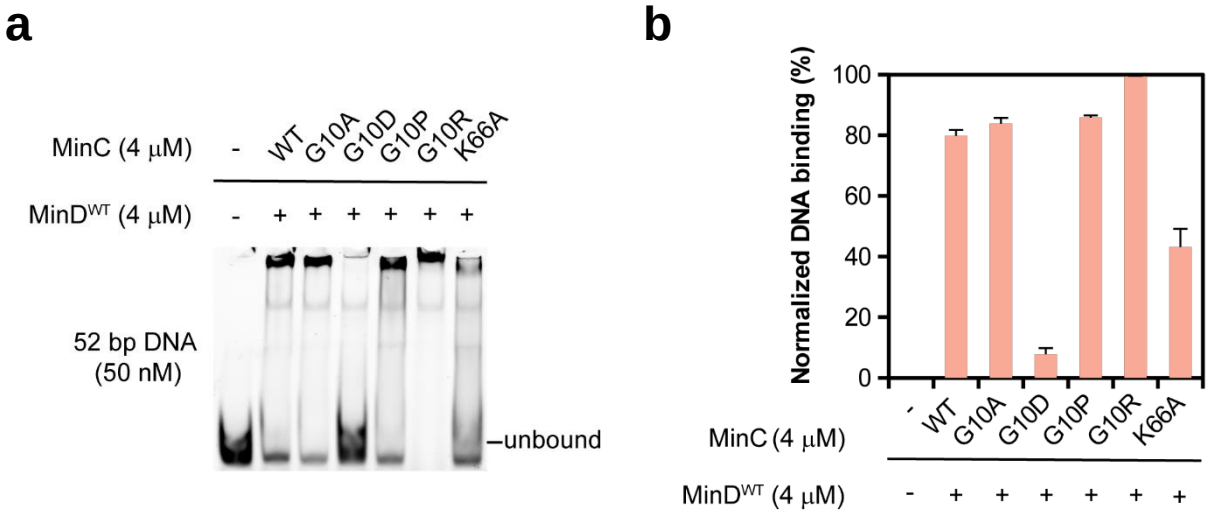

Figure 16. DNA-binding activity of single amino acid substituted MinC mutants. MinD (4 μM) was co-incubated with MinC (4 μM) WT or mutants and 50 nM of hex-labelled DNA (52 bp) in a buffer containing 1 mM ATP and 5 mM $MgCl_2$. a) Representative native-PAGE (EMSA) gel showing DNA-binding activity of MinC WT and single amino acid substituted mutants. b) Bar plot showing quantification of DNA binding (in %) of MinC WT and single amino acid substituted mutants. Experiments were performed thrice and mean±S.E.M. is plotted in the graph.

The G10 residue, and a few amino acids upstream and downstream to this residue, in the MinC N-terminal domain, have been shown to form a β-sheet and they homo-dimerize *via* domain swapping (23). From the previous experiment, we know that the G10 residue plays a role in DNA binding either directly or indirectly. We hypothesized that removing the whole β-sheet in the N-terminal of MinC should impair the DNA binding. For this purpose, we constructed and purified a MinC mutant lacking the first 20 amino acids from the N-terminal

region ($MinC^{\Delta 1-20}$). EMSA experiments were performed with MinD WT (4 μM) and $MinC^{\Delta 1-20}$ (4 μM). Surprisingly, it was found that removing the first 20 amino acids from the N-terminal of MinC resulted in reduced DNA binding, but not as impaired as the G10D mutant (**Figure 17**). We further questioned whether the N- or C- terminal domain of MinC is dispensable for the DNA binding. EMSA experiments were performed with purified $MinC^{N\text{-}term}$ (amino acids from 1 to 101, encompassing the entire N-terminal domain of MinC) and $MinC^{C\text{-}term}$ (amino acids from116 to 231, encompassing the entire C-terminal domain of MinC) in presence of MinD WT and hex-labelled DNA. Even at 4 μM of $MinC^{N\text{-}term}$ and $MinC^{C\text{-}term}$, no DNA binding was observed (**Figure 17**). These observations suggest that neither the N-terminal domain of MinC nor the C-terminal domain is dispensable for the DNA binding (**Figure 17**).

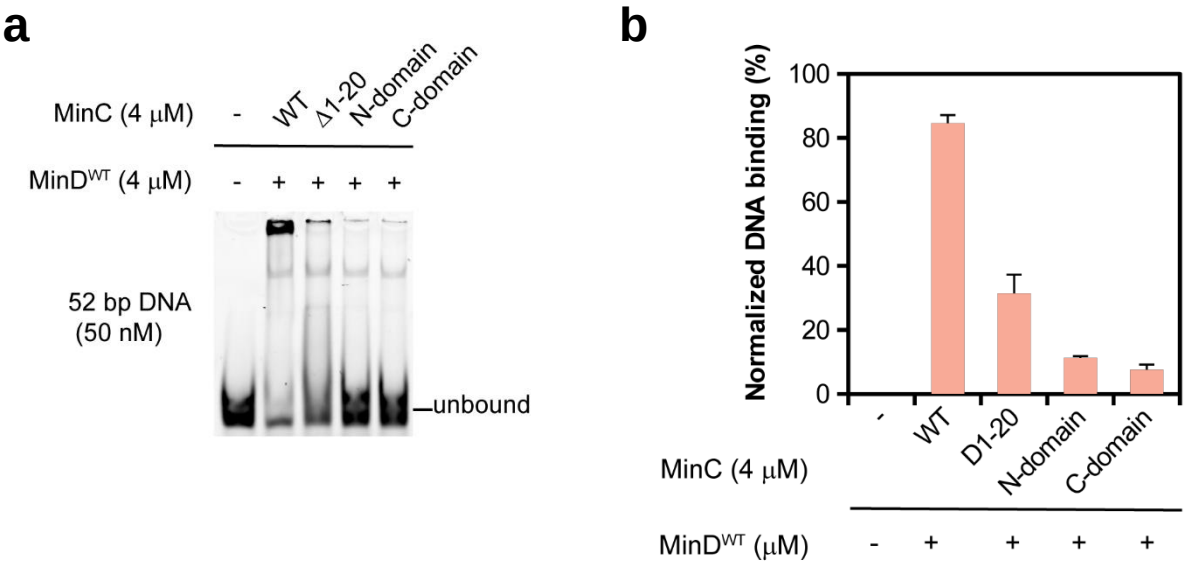

Figure 17. DNA-binding activity of MinC deletion mutants. MinD (4 μM) was co-incubated with MinC (4 μM) WT or deletion mutants and 50 nM of hex-labelled DNA (52 bp) in a buffer containing 1 mM ATP and 5 mM $MgCl_2$. a) Representative native-PAGE (EMSA) gel showing DNA-binding activity of MinC WT and deletion mutants. b) Bar plot showing quantification of DNA binding (in %) of MinC WT and deletion mutants. Experiments were performed thrice and mean±S.E.M. is plotted in the graph.

2.1.5. MinC mutants bind to MinD as well as the MinC WT

The EMSA experiments performed with the $MinC^{R133A}$ mutant suggested that alternating copolymers of MinCD are not needed for the DNA binding. So far, it was not clear whether the impairment in the DNA binding by the $MinC^{G10D}$ mutant and the reduced DNA binding by the $MinC^{K66A}$ and the $MinC^{\Delta 1-20}$ mutants were due to lack of MinD binding.

For this purpose, I performed a liposome co-sedimentation assay. As MinD possesses membrane targeting sequence, upon dimerization, they get recruited to the liposomes. MinC

also gets recruited to the liposomes with the help of MinD. On centrifugation, liposome being heavy goes to the pellet carrying with it the bound MinD and MinC. MinD WT (2 μM) was incubated with MinC WT or the mutants (2 μM) and 0.5 mg/ml of liposomes in a buffer containing 1 mM ATP and 5 mM $MgCl_2$, and then the mixture was centrifuged. It was found that $MinC^{G10D}$, $MinC^{K66A}$ and $MinC^{\Delta 1\text{-}20}$ mutants interacted with MinD as well as the MinC WT (**Figure 18**). This suggested that the impairment in DNA binding by $MinC^{G10D}$ mutant and reduced DNA binding by $MinC^{K66A}$ and $MinC^{\Delta 1\text{-}20}$ mutants were not due to impairment with MinD binding.

2.1.6. DNA binding of the $MinC^{G10D}$ mutant is impaired electrostatically

As the $MinC^{G10D}$ mutant behaves similarly to MinC WT in binding to MinD, and only the DNA binding is impaired in the EMSA experiments, we speculated that the introduction of aspartate at residue position 10 in MinC might have disrupted the β-sheet. To validate our speculation, the N-terminal domain of MinC carrying the respective mutations ($MinC^{N\text{-}term\ WT}$, $MinC^{N\text{-}term/G10D}$, $MinC^{N\text{-}term/G10P}$ and $MinC^{N\text{-}term/\Delta 1\text{-}20}$) were purified and submitted to the Protein Expression and Purification Core Facility at the EMBL, Heidelberg for performing circular-dichroism (CD) experiments.

It was found that $MinC^{WT}$ and $MinC^{G10D}$ have similar molar ellipticity per mean residue (θ) albeit with minor differences, and $MinC^{G10P}$ and $MinC^{\Delta 1\text{-}20}$ were found to have larger perturbations in θ (**Figure 19**).

The CD spectra of MinC N-terminal domain WT and mutants were also studied at different temperatures. This experiment provides data about the unfolding dynamics of a protein as a function of temperature. Depending on the secondary structures a protein has, the temperature needed to dissipate these secondary structures varies. From this study, it has been found that, like before, both the $MinC^{N\text{-}term\ WT}$ and $MinC^{N\text{-}term/G10D}$ mutant have similar θ when studied at temperatures varying from 20 ºC to 95 ºC (**Figure 20**). The θ of the $MinC^{N\text{-}term/G10P}$ mutant, on the other hand, varied significantly (**Figure 20**). In both the experiments, the $MinC^{N\text{-}term/\Delta 1\text{-}20}$ mutant exhibited similar trends to that of the WT and $MinC^{G10D}$ mutant; when absorbance was measured from 200 nm to 250 nm (**Figure 19**) and when absorbance was measured at different temperatures from 20 ºC to 95 ºC (**Figure 20**). But, the differences in θ were significant.

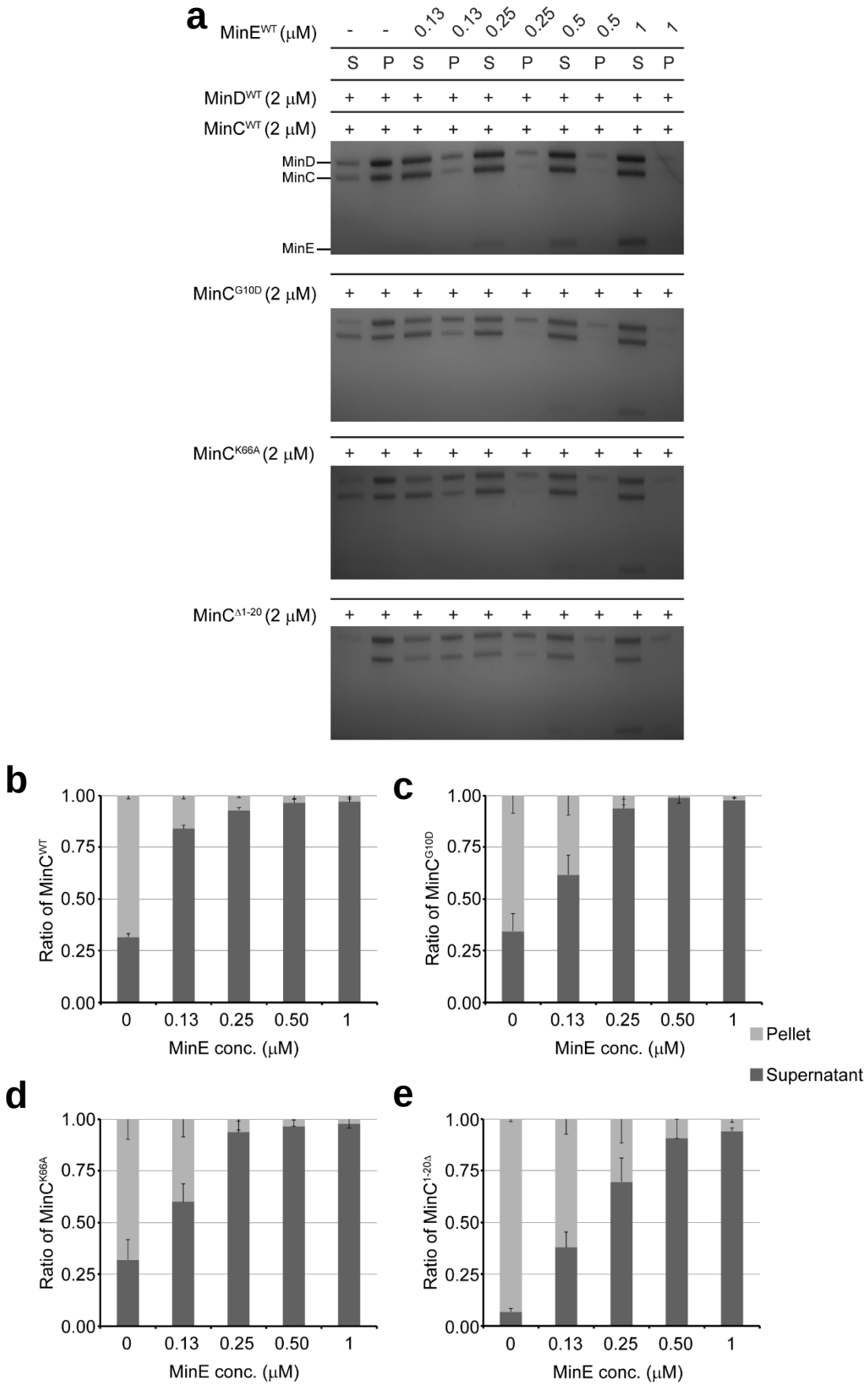

Figure 18. Liposome co-sedimentation assay with MinC mutants. MinD WT (2 μM) was co-incubated with MinC (2 μM) WT or mutants and 0.5 mg/ml of liposomes in a buffer containing 1 mM ATP and 5 mM $MgCl_2$. a)

Representative SDS-PAGE gels showing fraction of MinC WT and mutants in the supernatant (S) and the pellet (P) after the liposome co-sedimentation assay. (b) – (e) Bar plots showing quantification of MinC WT and mutants in the supernatant and the pellet after the liposome co-sedimentation assay. Experiments were performed thrice and mean±S.E.M. is plotted in the graph.

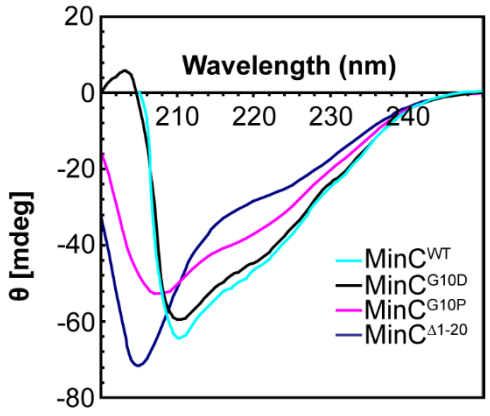

Figure 19. CD spectra of N-terminal domain of MinC WT and mutants at constant temperature. MinC N-terminal domain (10 μM) WT or mutants in a buffer containing 50 mM HEPES-KOH pH 7.25, 150 mM KCl, 10 % glycerol and 0.1 mM EDTA pH 8.0 was incubated at 20 ºC and measurements were done using a Jasco-815 spectrometer. Data was provided by the Protein Expression and Protein Purification Core Facility of the EMBL, Heidelberg.

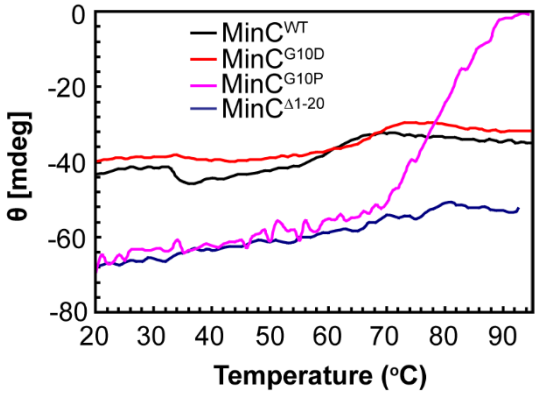

Figure 20. CD spectra of N-terminal domain of MinC WT and mutants at different temperatures. MinC N-terminal domain (10 μM) WT or mutants in a buffer containing 50 mM HEPES-KOH pH 7.25, 150 mM KCl, 10 % glycerol and 0.1 mM EDTA pH 8.0 was incubated at varying temperatures and measurements were done using a Jasco-815 spectrometer. Data was provided by the Protein Expression and Protein Purification Core Facility of the EMBL, Heidelberg.

MinC N-terminal domain exists as a dimer and this dimerization occurs *via* domain swapping (18,23). From the CD experiments, it was clear that the $MinC^{N\text{-}term}$ WT and $MinC^{N\text{-}term/G10D}$ mutant have similar secondary structural elements, while the $MinC^{N\text{-}term/G10P}$ and $MinC^{N\text{-}term/\Delta 1\text{-}20}$ mutants have different secondary structural elements. Size exclusion

chromatography (SEC) was performed with the MinC N-terminal domain WT and mutants, in order to study the dimerization property of these proteins. Like the CD experiments, SEC experiments were also performed by the Protein Expression and Protein Purification Core Facility of the EMBL, Heidelberg. Superdex 75 10/300 GL column was used for the SEC experiments and the running buffer consisted of 50 mM HEPES-KOH pH 7.25, 150 mM KCl, 10 % glycerol and 0.1 mM EDTA pH 8.0. It was found that MinC N-terminal domain WT, and the mutants G10D and G10P, eluted as a dimer (**Figure 21**). Interestingly, a fraction of $MinC^{N\text{-}term/\Delta 1\text{-}20}$ mutant eluted as a tetramer while the remaining major fraction eluted as a dimer (**Figure 21**). Taken together with the observations from the CD and SEC experiments, we interpreted that the impairment in $MinC^{G10D}$ binding to DNA is purely electrostatic and not due to any secondary structural deformation.

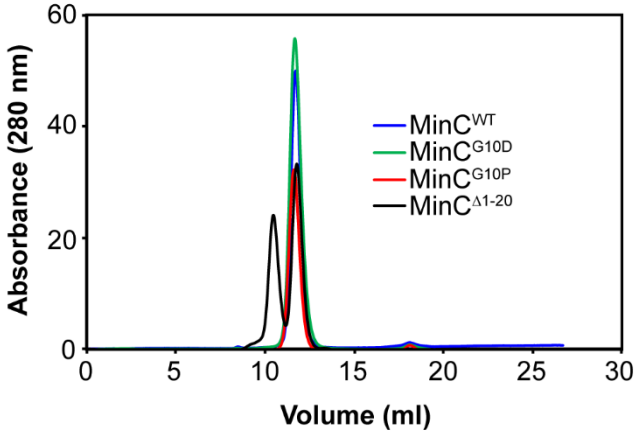

Figure 21. MinC N-terminal domain G10D mutant dimerizes. Data was provided by the Protein Expression and Protein Purification Core Facility of the EMBL, Heidelberg.

2.1.7. Linker region of MinC plays a critical role in the DNA binding

One of our collaborators elucidated the cryo-EM structure of *Ec*MinC and *Ec*MinD copolymers. Unfortunately, secondary structural features of the N-terminal domain and the linker region of MinC could not be assigned with a greater confidence. This problem might have arosen primarily due to the predicted high flexibility of the MinC linker region. So, to get better cryo-EM data, I questioned the importance of the MinC linker region in the DNA binding. The proline-rich linker region of *Ec*MinC is composed of 19-25 amino acids depending on how one arbitrarily assigns the start position of the MinC C-terminal domain (**Figure 22**). For this purpose, several MinC non-native linker variants, namely GS, 1x AGGSG, 2x AGGSG, 3x AGGSG, and 4x AGGSG were constructed. These names indicate the amino acid composition of the MinC linkers. For example, in the GS construct, between

the MinC N- and C- terminal domains, the linker region constitutes only 2 amino acids namely glycine (G) and serine (S). In the 1x AGGSG construct, the linker region constitutes 5 amino acids namely alanine (A), glycine (G), glycine (G), serine (S) and glycine (G). The number prior to the amino acid sequence indicates the number of times this pentapeptide sequence is present in the linker. In the 2x construct, this pentapeptide is repeated twice and in the 3x construct this pentapeptide is repeated thrice, etc. in order to match the length of the native MinC linker region. MinC non-native linker variants were purified and EMSA experiments were performed. MinD (4 μM) was co-incubated with MinC (4 μM) WT or non-native linker variants and hex-labelled DNA, in a buffer containing ATP and $MgCl_2$. It was found that altering MinC's linker region resulted in impairment of DNA binding (**Figure 23**).

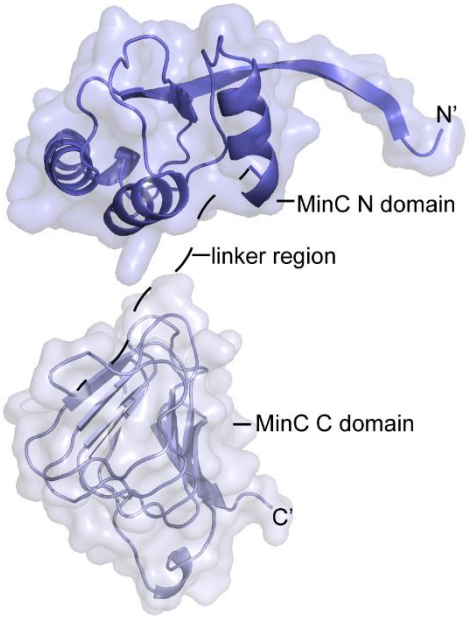

Figure 22. Modelled structure of *E. coli* MinC. Crystal structures of MinC N-terminal and C-terminal domains were obtained from the protein data bank (https://www.rcsb.org/) with IDs 4l1c (23) and 5xdm (24), respectively. Linker region is represented with dashes. Image was created by Dr. Mehmet Ali Öztürk.

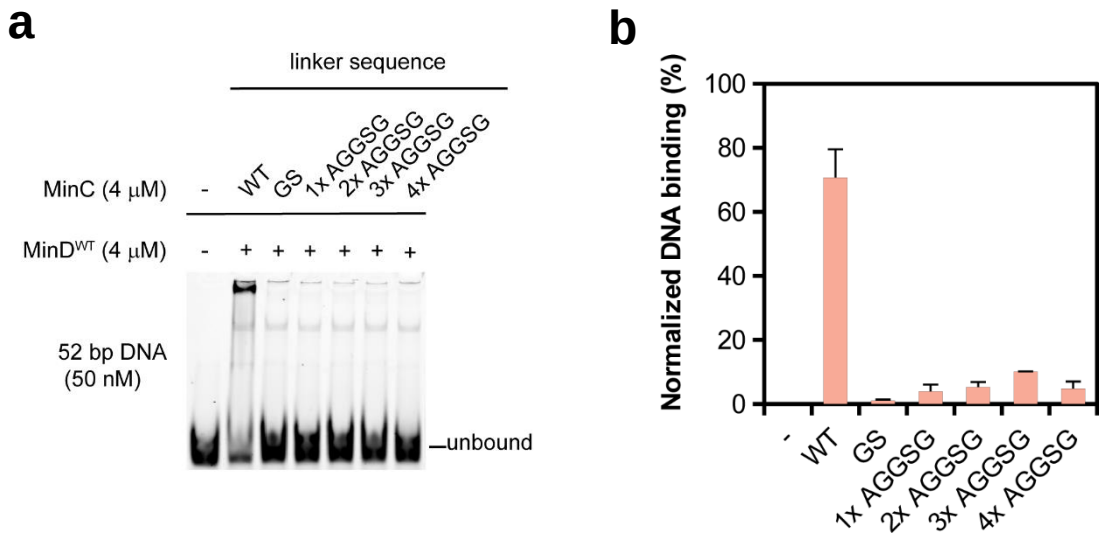

Figure 23. DNA-binding activity of MinC non-native linker variants. MinD (4 μM) was co-incubated with MinC (4 μM) WT or non-native linker variants and 50 nM of hex-labelled DNA (52 bp) in a buffer containing 1 mM ATP and 5 mM $MgCl_2$. a) Representative native-PAGE (EMSA) gel showing DNA-binding activity of MinC WT and non-native linker variants. b) Bar plot showing quantification of DNA binding (in %) of MinC WT and non-native linker variants. Experiments were performed thrice and mean±S.E.M. is plotted in the graph.

At first, we speculated that probably the length of the MinC linker is critical for the DNA binding. The aforementioned 4x construct has 20 amino acids as the linker, while the WT linker consists of only 19 amino acids. In the 4x AGGSG construct, the final glycine residue in the fourth pentapeptide repeat was eliminated and this protein (3x AGGSG+AGGS) was purified, and EMSA experiments were performed. Similar to the other MinC non-native linker variants, DNA binding was impaired with this MinC linker variant too (**Figure 24**).

Next, we speculated that the amino acid sequence of the MinC linker is critical for the DNA binding. For this purpose, the native residues of *Ec*MinC's linker were retained while playing around only with the length of this linker. Three MinC native linker variants, namely $MinC^{\Delta 102\text{-}105}$, $MinC^{\Delta 102\text{-}109}$ and $MinC^{\Delta 102\text{-}114}$ were purified and EMSA experiments were performed. Surprisingly, it was found that altering the length of the native linker also impaired the DNA-binding ability (**Figure 25**). Taken together these observations, we interpreted that not only the amino acid sequence but also the length of the MinC linker plays a vital role in the DNA-binding ability of the MinC.

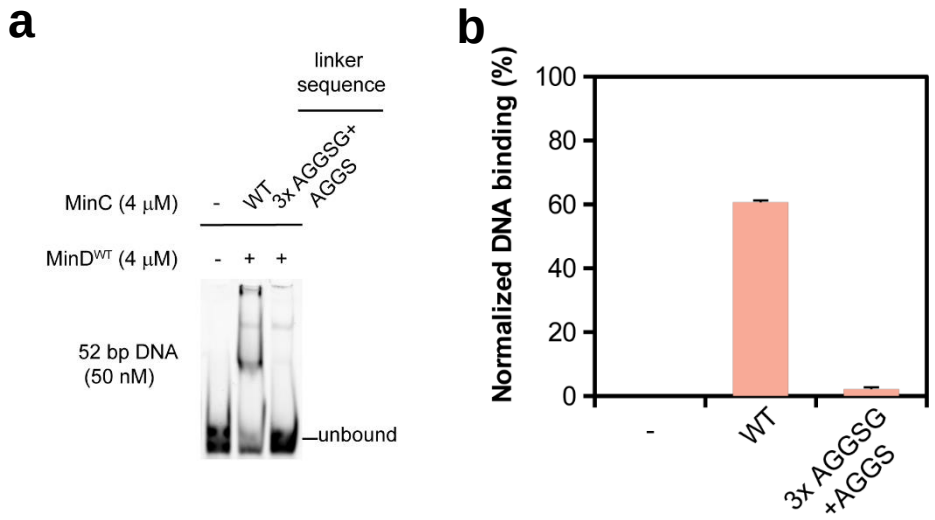

Figure 24. DNA-binding activity of a MinC non-native linker variant having same linker length as WT. MinD (4 μM) was co-incubated with MinC (4 μM) WT or non-native linker variant and 50 nM of hex-labelled DNA (52 bp) in a buffer containing 1 mM ATP and 5 mM $MgCl_2$. a) Representative native-PAGE (EMSA) gel showing DNA-binding activity of MinC WT and non-native linker variant. b) Bar plot showing quantification of DNA binding (in %) of MinC WT and non-native linker variant. Experiments were performed thrice and mean±S.E.M. is plotted in the graph.

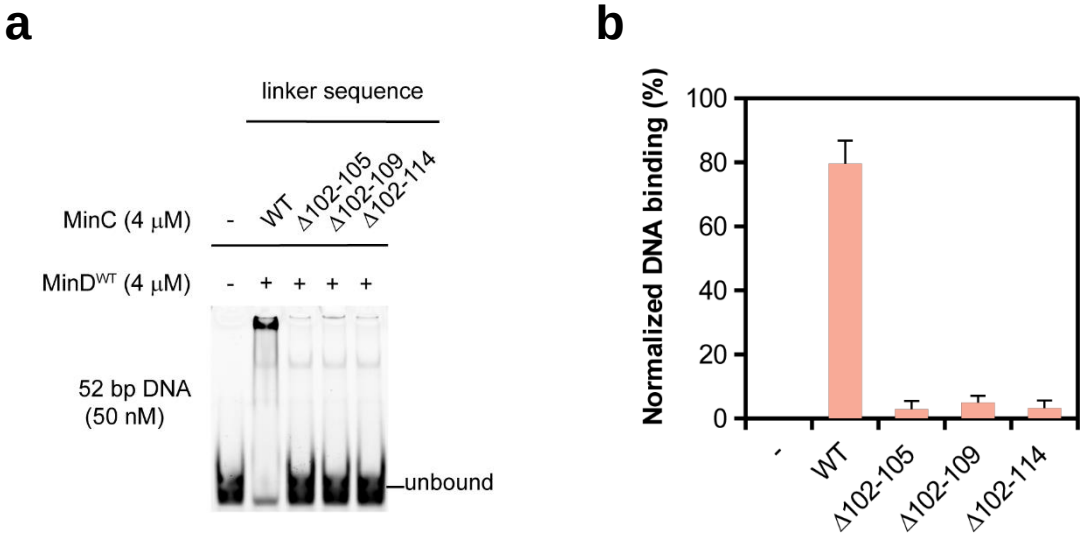

Figure 25. DNA-binding activity of MinC native linker variants. MinD (4 μM) was co-incubated with MinC (4 μM) WT or native linker variants and 50 nM of hex-labelled DNA (52 bp) in a buffer containing 1 mM ATP and 5 mM $MgCl_2$. a) Representative native-PAGE (EMSA) gel showing DNA-binding activity of MinC WT and native linker variants. b) Bar plot showing quantification of DNA binding (in %) of MinC WT and native linker variants. Experiments were performed thrice and mean±S.E.M. is plotted in the graph.

Using the $MinC^{R133A}$ mutant, we have shown that alternating copolymers of MinC/MinD are not needed for the DNA-binding activity. We questioned whether MinC heterodimers, formed with MinC WT and one of the non-native MinC linker variants, can retain the DNA-binding ability. For this purpose, MinC 4x AGGSG linker variant was used.

EMSA experiments were performed similar to that of the $MinC^{R133A}$ study, except here we used way less concentration of the MinC non-native linker variant. Interestingly, it was found that as little as 1 μM of the MinC non-native linker variant reduced the DNA-binding ability of MinC WT by ~10 % (**Figure 26**). At an equimolar concentration of MinC WT and the non-native linker variant, the DNA-binding ability of MinC WT was brought down to the basal level (**Figure 26**). We questioned if varying the length of the MinC's linker affected its ability to bind to MinD. To study this, liposome co-sedimentation assay was performed as described before. It was found that all the MinC linker variants (with both native and non-native linker residues) retained their MinD-binding ability as good as the MinC WT (**Figure 27**).

In one of our earlier EMSA experiments, we studied $MinC^{N\text{-}term}$ and $MinC^{C\text{-}term}$, and found that the DNA-binding activity was impaired. Those MinC deletion mutants were devoid of the linker. We next questioned whether adding the native linker to these MinC N- and C-terminal domains show any increased DNA binding. For studying this, we constructed five constructs namely, 1) $MinC^{N\text{-}term}$ with the native linker; $MinC^{N\text{-}term+linker}$, 2) native linker with $MinC^{C\text{-}term}$; $MinC^{linker+C\text{-}term}$, 3) $MinC^{N\text{-}term}$ with the native linker followed by a leucine zipper from *Saccharomyces cerevisiae* general control protein 4 (GCN4) (bZIP); $MinC^{N\text{-}term+linker}$-bZIP, 4) maltose-binding protein (MBP) followed by bZIP; MBP-bZIP, and 5) maltose-binding protein (MBP) with the MinC native linker followed by bZIP; MBP^{linker}-bZIP (**Figure 28a**). Proteins were purified and EMSA experiments were performed. The experiments were performed in the presence and the absence of MinD. In the absence of MinD, no DNA binding was observed with MinC WT, $MinC^{N\text{-}term+linker}$, and $MinC^{linker+C\text{-}term}$. On the other hand, in the presence of MinD, MinC WT and $MinC^{linker+C\text{-}term}$ exhibited DNA-binding activity (**Figure 28b and c**). In fact, $MinC^{linker+C\text{-}term}$ had even higher DNA-binding activity than that of the MinC WT (**Figure 28b and c**). The DNA-binding activity of $MinC^{N\text{-}term+linker}$ was slightly higher than that of the background, and the presence or the absence of MinD had no effect (**Figure 28b and c**). When using the $MinC^{N\text{-}term+linker}$-bZIP, MBP-bZIP and MBP^{linker}-bZIP, interestingly, $MinC^{N\text{-}term+linker}$-bZIP exhibited DNA binding slightly higher than that of the MinC WT but lower than that of $MinC^{linker+C\text{-}term}$, and unlike the MinC WT, the presence or the absence of MinD had no effect (**Figure 28b and d**). MBP-bZIP, which was used as a negative control, exhibited no DNA-binding activity (or meager). MBP^{linker}-bZIP, on the contrary, exhibited DNA binding albeit only half of what has been seen for the MinC WT (**Figure 28b and d**), and the presence or the absence of MinD had no effect.

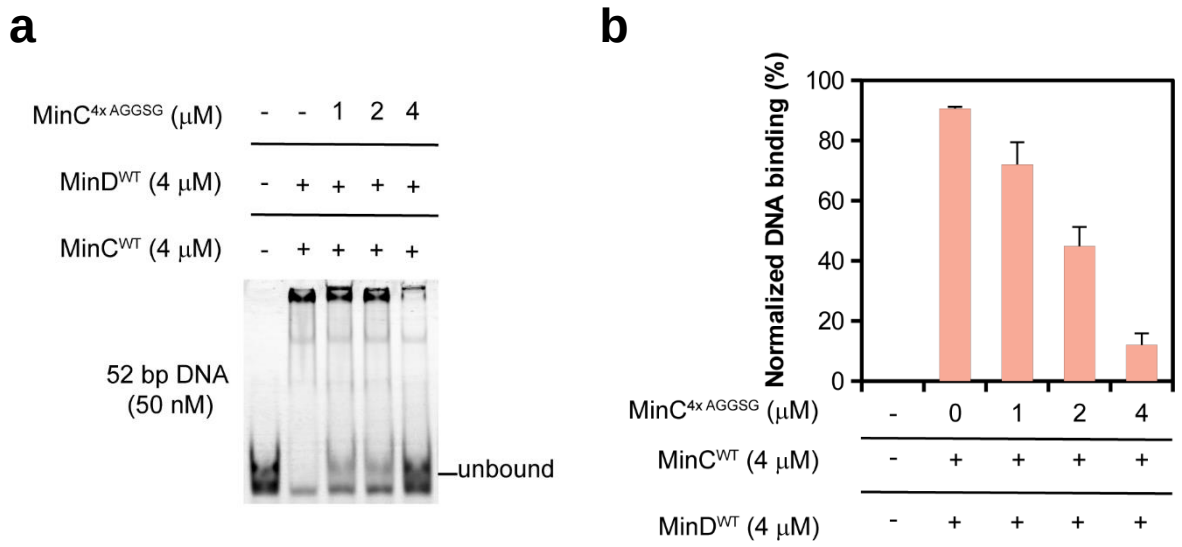

Figure 26. MinC non-native linker variant (4x AGGSG) inhibits the DNA-binding ability of $MinC^{WT}$/MinD. MinD (4 μM) was co-incubated with MinC (4 μM) and 50 nM of hex-labelled DNA (52 bp) in a buffer containing 5 mM $MgCl_2$ and 1 mM ATP, and with increasing concentration of $MinC^{4x\ AGGSG}$. a) Representative native-PAGE (EMSA) gel showing DNA-binding activity of MinCD with increasing concentration of $MinC^{4x\ AGGSG}$. b) Bar plot showing quantification of DNA binding (in %) of MinCD with increasing concentration of $MinC^{4x\ AGGSG}$. Experiments were performed thrice and mean±S.E.M. is plotted in the graph.

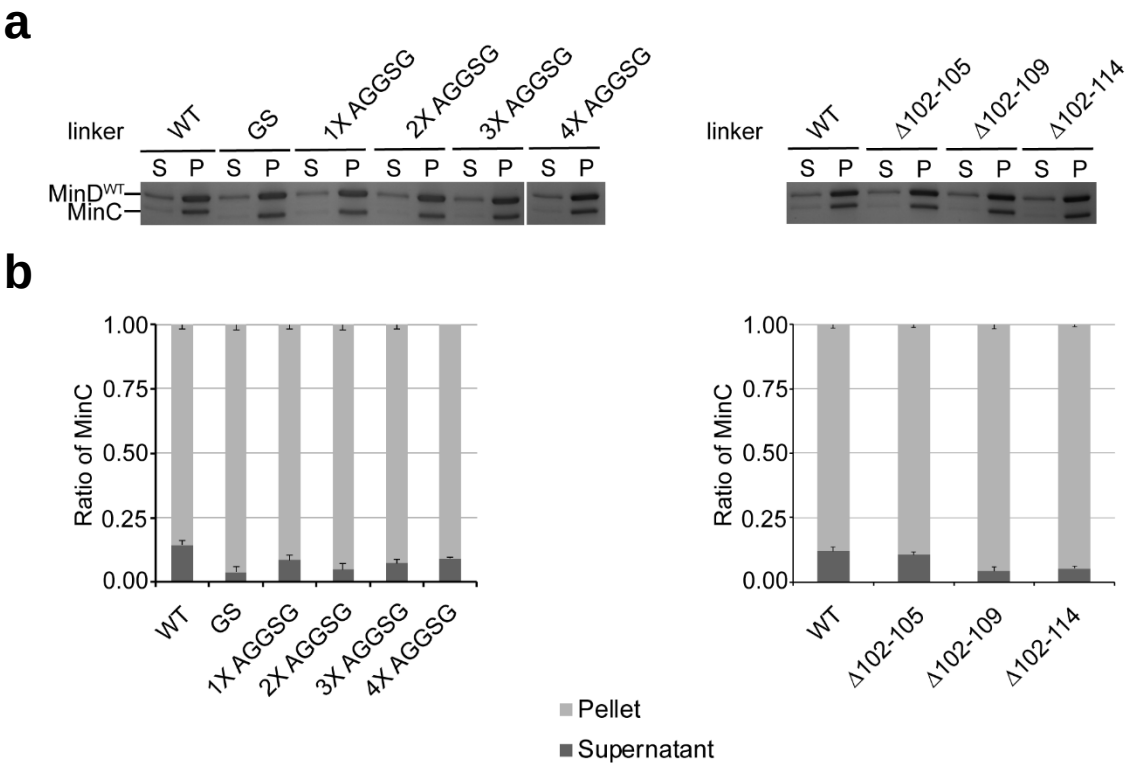

Figure 27. Liposome co-sedimentation assay with MinC linker variants. MinD WT (2 μM) was co-incubated with MinC (2 μM) WT or linker variants and 0.5 mg/ml of liposomes in a buffer containing 1 mM ATP and 5 mM $MgCl_2$. a) Representative SDS-PAGE gels showing fraction of MinC WT and linker variants in the supernatant

(S) and the pellet (P) after the liposome co-sedimentation assay. b) Bar plots showing quantification of MinC WT and linker variants in the supernatant and the pellet after the liposome co-sedimentation assay. Experiments were performed thrice and mean±S.E.M. is plotted in the graph.

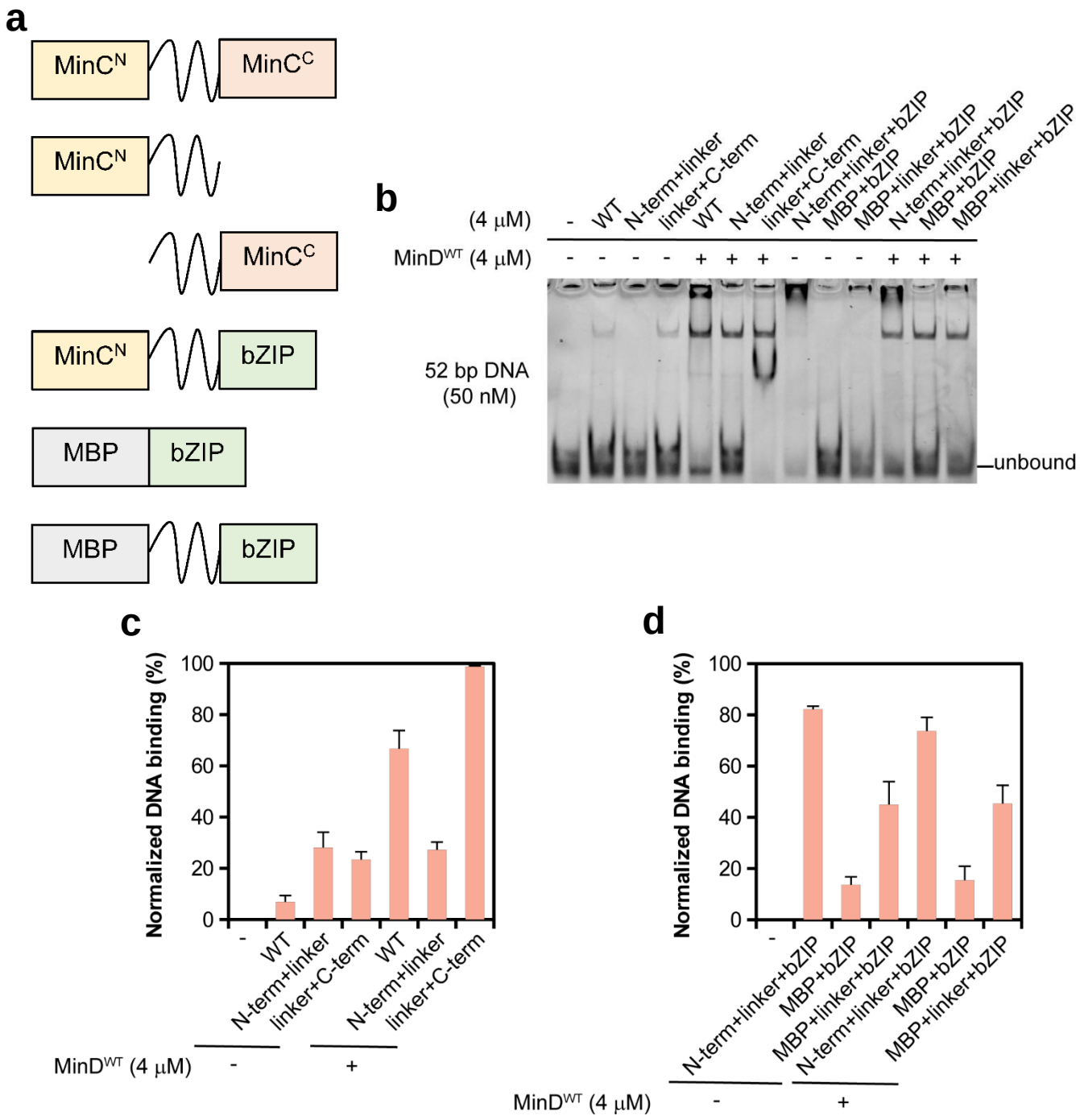

Figure 28. *E. coli* MinC native-linker sequence exhibits DNA binding in electrophoretic mobility shift assay (EMSA). a) Schematics of proteins used in this study. b) Representative gel image showing DNA binding by MinC native-linker sequence. Maltose binding protein (MBP) with leucine zipper (bZIP) and MBP with MinC linker and bZIP were used as controls. c) and d) Bar graphs showing quantification of DNA binding by MinC native-linker sequence. Experiments were performed three times and mean±SEM are plotted in the graph.

2.1.8. FtsZ inhibits the DNA-binding ability of MinC/MinD

MinC G10 residue has been shown to interact with FtsZ, and mutation of glycine to aspartate at this position resulted in the impairment (21,22,79). From our earlier EMSA experiments, we know that G10D mutation impairs the DNA binding electrostatically. Based on this observation, we questioned whether FtsZ and the DNA binding interface on MinC overlap. To study this, EMSA experiments were performed in presence of excess of FtsZ. MinD WT (4 μM) was co-incubated with MinC WT (4 μM) and hex-labelled DNA. At different time points, with an interval of 2 min, 10 μM FtsZ was added to the reaction mixture. If the binding interface(s) overlap, depending on the time of addition of excess FtsZ, the DNA-binding activity of MinC should be impaired. As expected, FtsZ inhibited the DNA-binding activity of MinC with time (**Figure 29**). This experiment suggests that FtsZ and the DNA-binding interface on MinC overlap.

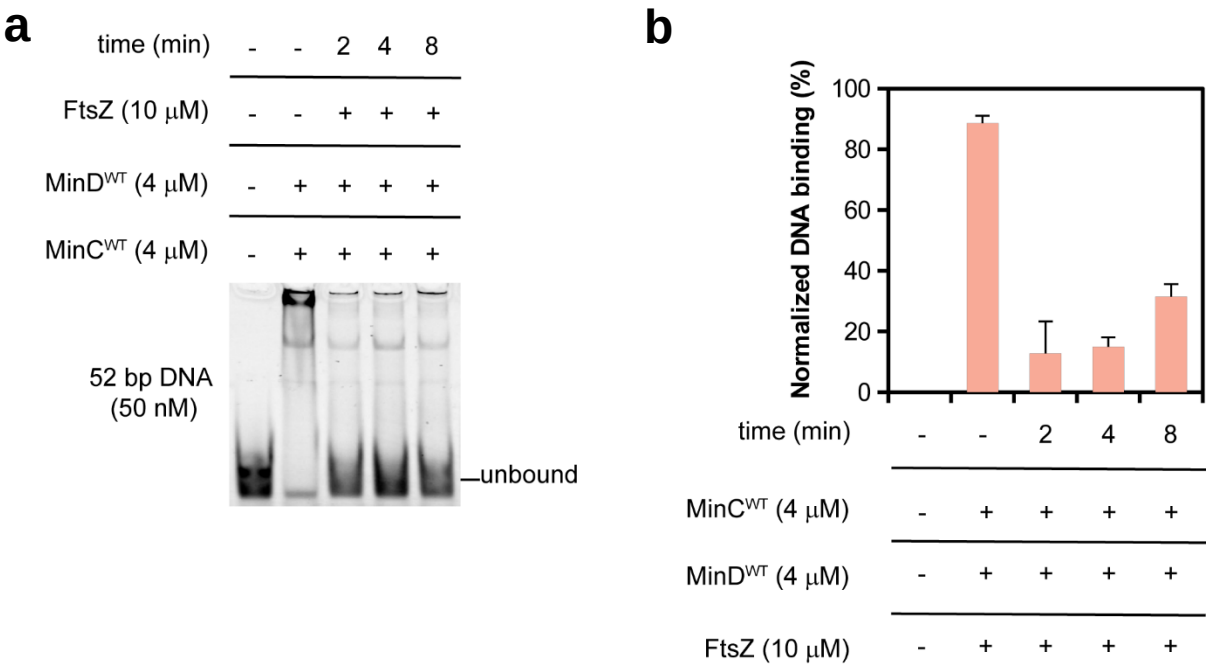

Figure 29. FtsZ inhibits the DNA-binding ability of MinC/MinD. MinD (4 μM) was co-incubated with MinC (4 μM) and 50 nM of hex-labelled DNA (52 bp) in a buffer containing 5 mM $MgCl_2$ and 1 mM ATP, and at regular intervals FtsZ (10 μM) was added. a) Representative native-PAGE (EMSA) gel showing DNA-binding activity of MinCD with FtsZ. b) Bar plot showing quantification of DNA binding (in %) of MinCD with FtsZ. Experiments were performed thrice and mean±S.E.M. is plotted in the graph.

2.1.9. FtsZ interaction of MinC^{G10P} is impaired

Min system is involved in the proper placement of Z-ring in *E. coli*. Additionally, we propose that MinC/MinD are involved in chromosome segregation. In order to study the chromosome segregation *in vivo*, we needed a mutant of MinC/MinD, which in theory, should not disturb the cell division but the DNA-binding ability should be impaired. We have a candidate MinC mutant, G10D, in which the DNA-binding activity is impaired. But, this mutant has impaired function with FtsZ too (21,22,79).

To make a proper comparison with MinC^{G10D}, we needed another MinC mutant in which the DNA-binding ability should be retained, while the inhibition of FtsZ should be impaired. For studying the MinC impairment in inhibitng the FtsZ polymerization, we performed cell viability spot assay. Overexpression of MinC and MinD in *E. coli* cells result in a lethal phenotype (no bacterial growth). On the contrary, if a MinC mutant has impaired function with FtsZ, *E. coli* cells can still able to divide by forming mini-cells (anucleate) and nucleate cells (bacterial growth). *E. coli minC* and *minD*, with their native ribosome binding sites, were cloned into the pBAD33 vector. Additionally, point mutations namely, G10A, G10D, G10P, and G10R were introduced in MinC. Upon the addition of arabinose to the media, the proteins are expressed. **Figure 30a** shows an overview of the cell viability spot assay. It was found that at higher arabinose concentration (0.1 %), MinC^{G10A} exhibited a lethal phenotype similar to that of the MinC WT (**Figure 30b**). On the other hand, MinC^{G10D} and MinC^{G10P} exhibited a non-lethal phenotype (**Figure 30b**). MinC^{G10R} exhibited an intermediary behavior (**Figure 30b**).

Cell viability spot assay was also performed for the MinC non-native and native linker variants to study whether the linker has any role in the FtsZ inhibition. First, we studied MinC WT and the linker variants in the absence of MinD. Unlike the previous study, MinC (WT or the mutants) has to be overexpressed way higher in order to induce lethality. For this purpose, MinC (WT or the mutants) was cloned into the pET28a vector and transformed into *E. coli* Rosetta™(DE3)pLysS strain. And, spotting was done on agar plates containing different concentrations of IPTG. Other steps were similar to the previous study. It was found that all the linker variants had slight to moderate impairment in the FtsZ interaction (**Figure 31**).

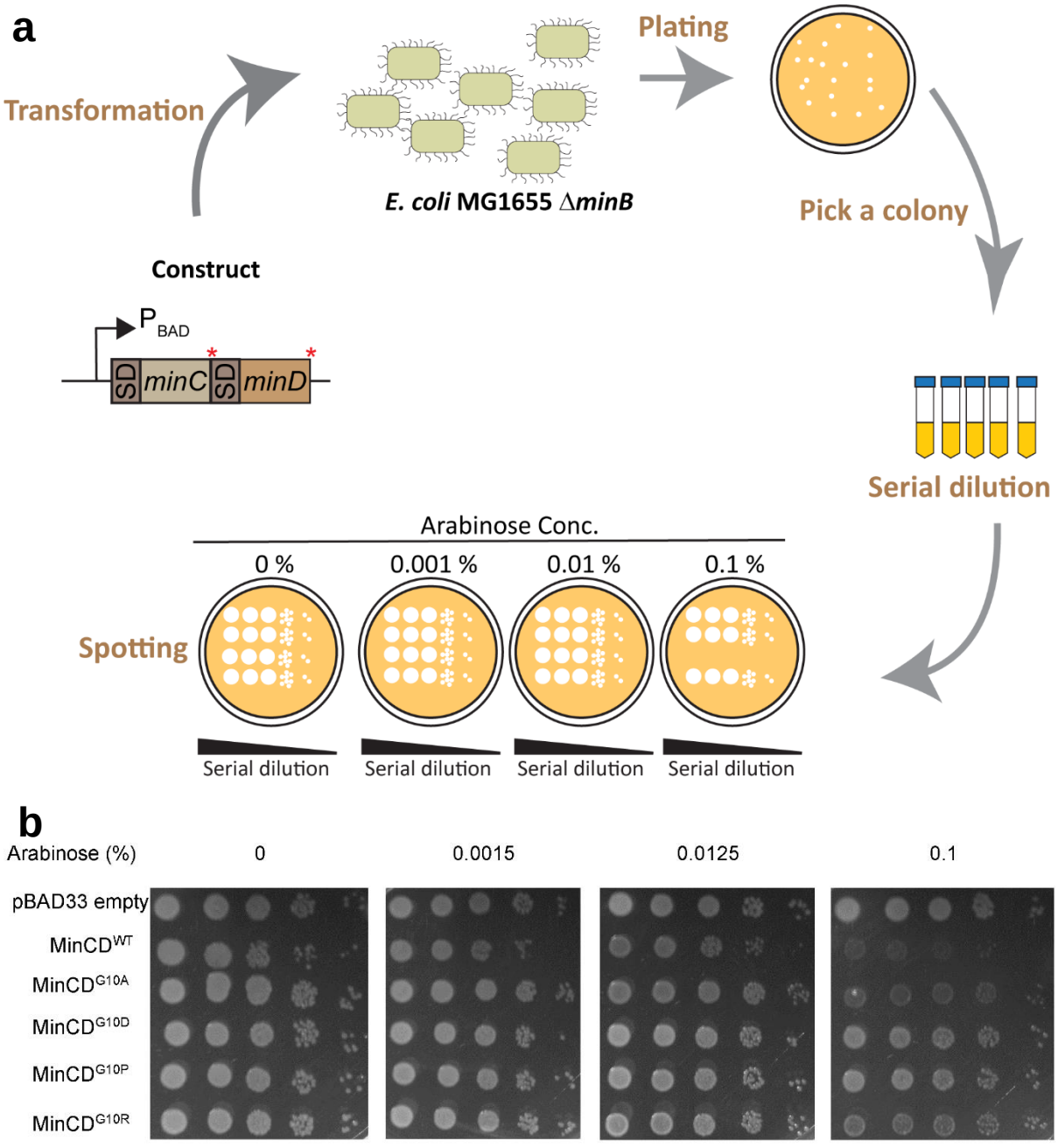

Figure 30. MinC^{G10P} behaves similar to MinC^{G10D} in cell viability spot assay. a) Overview of cell viability spot assay. Illustration was made based on the information from Zhou and Lutkenhaus (80). b) Representative agar plate images showing cell viability of MinC WT and point mutants.

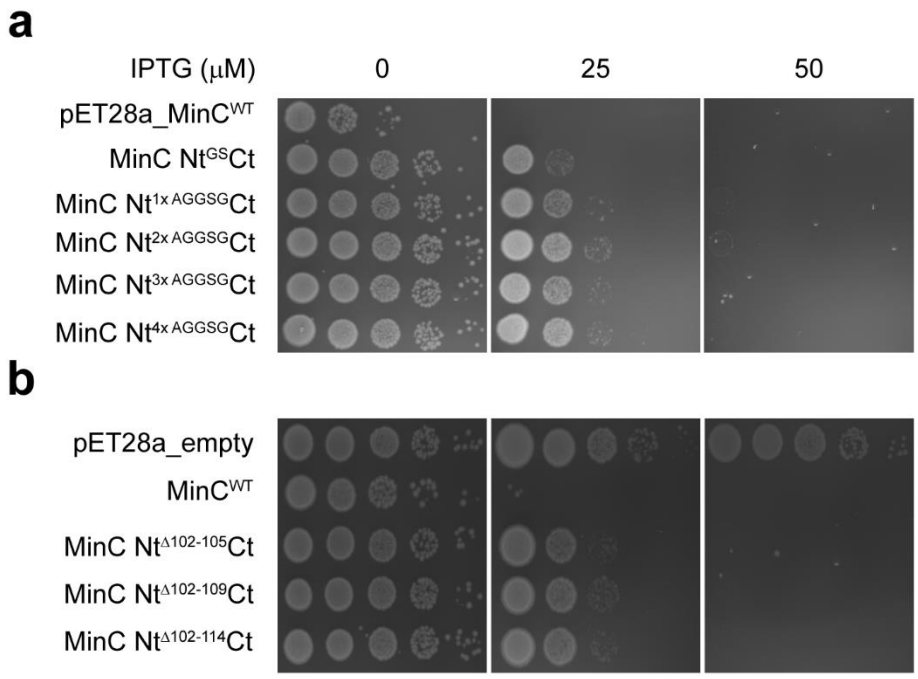

Figure 31. MinC linker variants show slight to moderate impairment in FtsZ interaction. a) Representative agar plate images showing cell viability of MinC non-native linker variants. b) Representative agar plate images showing cell viability of MinC native linker variants.

Next, we studied the same with the presence of MinD. For this purpose, we went back to the pBAD33 backbone and spotting was done on plates with different arabinose concentrations. Surprisingly, now MinC with only two linker residues (GS) lost its ability to interact with FtsZ completely (**Figure 32**). While the other linker variants exhibited only slight impairment in the FtsZ interaction (**Figure 32**). Taken together the data from the cell viability spot assays, we interpreted that $MinC^{G10P}$ has impairment in the FtsZ interaction similar to that of the $MinC^{G10D}$. Additionally, when MinC is in a soluble form (cytoplasmic), the linker length only plays a minor role in the FtsZ polymerization inhibition. On the other hand, when MinC gets recruited to the cell membrane *via* MinD, the linker length must be greater than 2 residues in order to inhibit the FtsZ polymerization. Therefore, we conclude that in a WT strain MinC's linker length plays an important role in inhibiting the FtsZ polymerization.

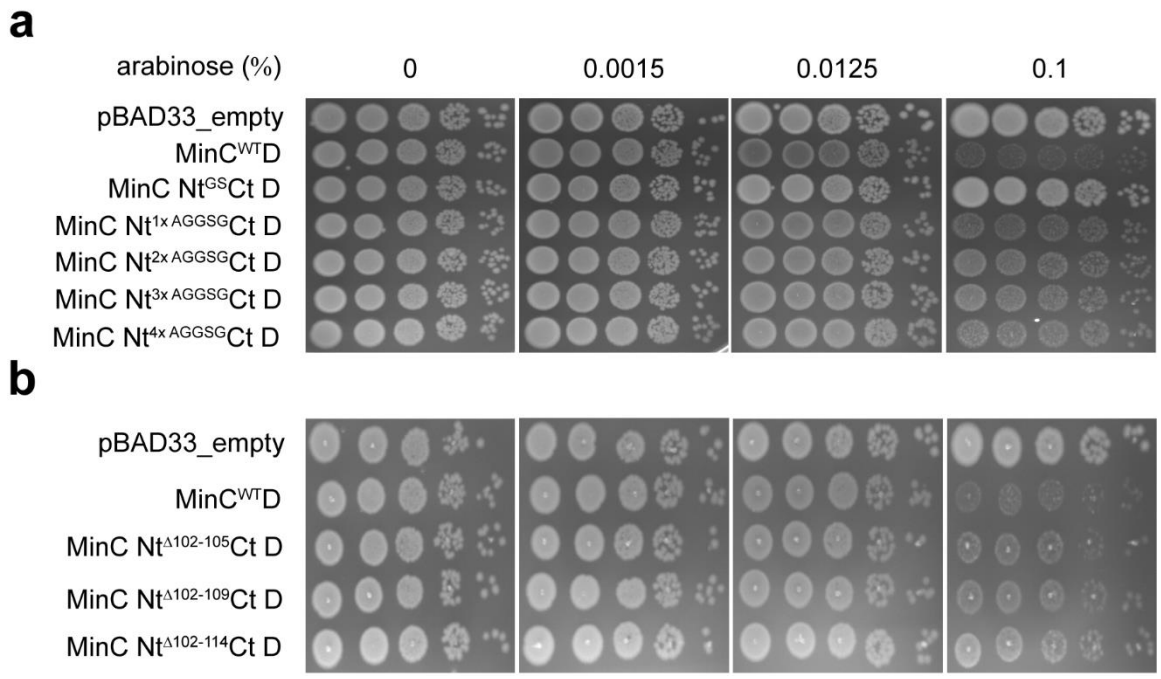

Figure 32. MinC's linker length plays a role in FtsZ interaction when recruited to cell membrane by MinD. a) Representative agar plate images showing cell viability of MinC non-native linker variants. b) Representative agar plate images showing cell viability of MinC native linker variants.

2.1.10. MinC N-terminal bZIP synthetic construct co-localizes with E. coli chromosome in vivo

Our new hypothesis revolves around the notion that not only MinD but also MinC aid in the chromosome segregation in *E. coli*. In the EMSA experiments, MinC$^{linker+C\text{-}term}$ exhibited the strongest DNA binding (**Figure 28**). However, this construct exhibited DNA binding only with the presence of MinD. I speculated that expression of both MinC$^{linker+C\text{-}term}$ and MinD inside *E. coli* cells will recruit most of MinC$^{linker+C\text{-}term}$ to the membrane and co-localization might not be observed. So, I decided to use the MinC$^{N\text{-}term+linker}$-bZIP synthetic construct with the *mruby3* gene fused downstream to the leucine zipper (pTrc99a-MinC$^{N\text{-}term+linker}$-bZIP-mRuby3) for the co-localization study (**Figure 33**). pTrc99a-MBP-bZIP-mRuby3 construct was used as a negative control for the comparison. It could be seen that MinC$^{N\text{-}term+linker}$-bZIP-mRuby3 co-localized with the nucleoid while the protein without the native linker (MinC$^{N\text{-}term}$-bZIP-mRuby3) and MBP-bZIP-mRuby3 were dispersed throughout the cell (**Figure 33**). Moreover, cells expressing MinC$^{N\text{-}term}$-bZIP-mRuby3 exhibited a filamentous phenotype (**Figure 33**). With the introduction of the G10D mutation to MinC$^{N\text{-}term+linker}$-bZIP-mRuby3, the co-localization was found not to be affected (**Figure 34**). Microscopy experiments were also performed in an *E. coli* MG1655 *hu-gfp* strain (81). Again, co-localization was observed with MinC$^{N\text{-}term+linker}$-bZIP-mRuby3, while MinC$^{N\text{-}term}$-bZIP-mRuby3 and MBP-bZIP-mRuby3

did not co-localize with the nucleoid (**Figure 35**). Expression of MBP-bZIP-mRuby3 in the *hu-gfp* strain exhibited an improper nucleoid segregation and cell division (**Figure 35**), while the expression of MinC$^{N\text{-}term}$-bZIP-mRuby3 exhibited a cell elongation (**Figure 35**), albeit not like the filamentation phenotype observed in the Δ*minB* counterpart (**Figure 33**).

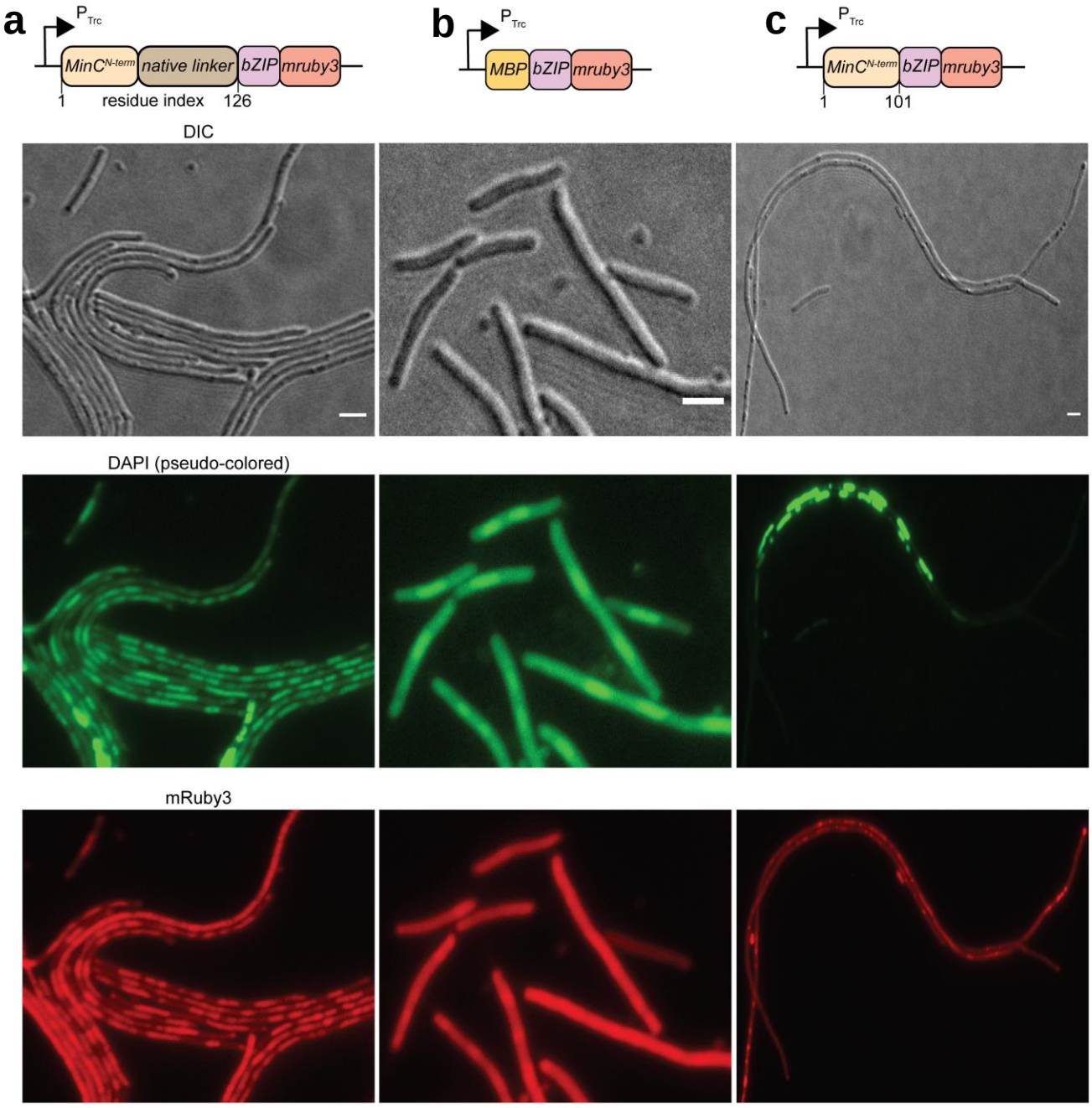

Figure 33. *In vivo* co-localization of MinC$^{N\text{-}term+linker}$-bZIP in Δ*minB E. coli* cells. Microscopy images of Δ*minB E. coli* cells transformed with the indicated constructs. a) MinC$^{N\text{-}term+linker}$-bZIP-mRuby3, b) MBP-bZIP-mRuby3 and c) MinC$^{N\text{-}term}$-bZIP-mRuby3. Protein expression was induced with 100 μM IPTG for 3 hours. Scale bar = 3 μm. Microscopy images were taken by Emir Bora Akmeriç.

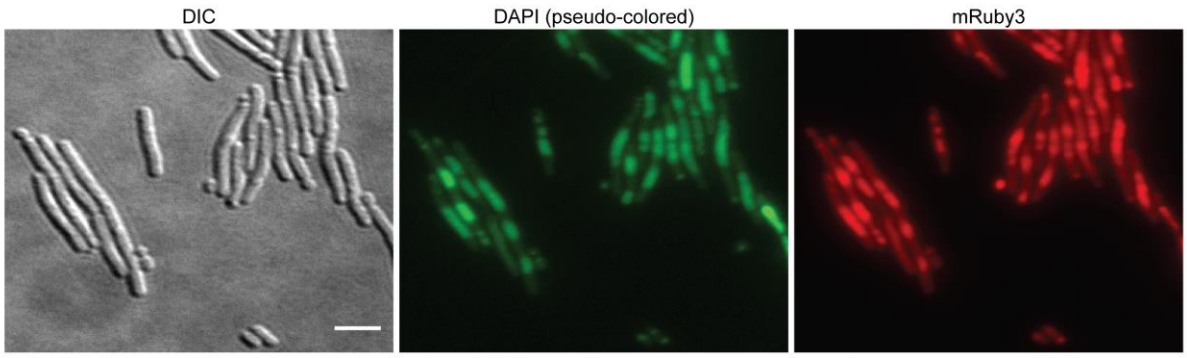

Figure 34. *In vivo* co-localization of MinC$^{N\text{-term/G10D+linker+bZIP}}$ in Δ*minB E. coli* cells. Microscopy images of Δ*minB E. coli* cells with the indicated construct. Protein expression was induced with 100 μM IPTG for 3 hours. Scale bar = 3 μm. Microscopy images were taken by Emir Bora Akmeriç.

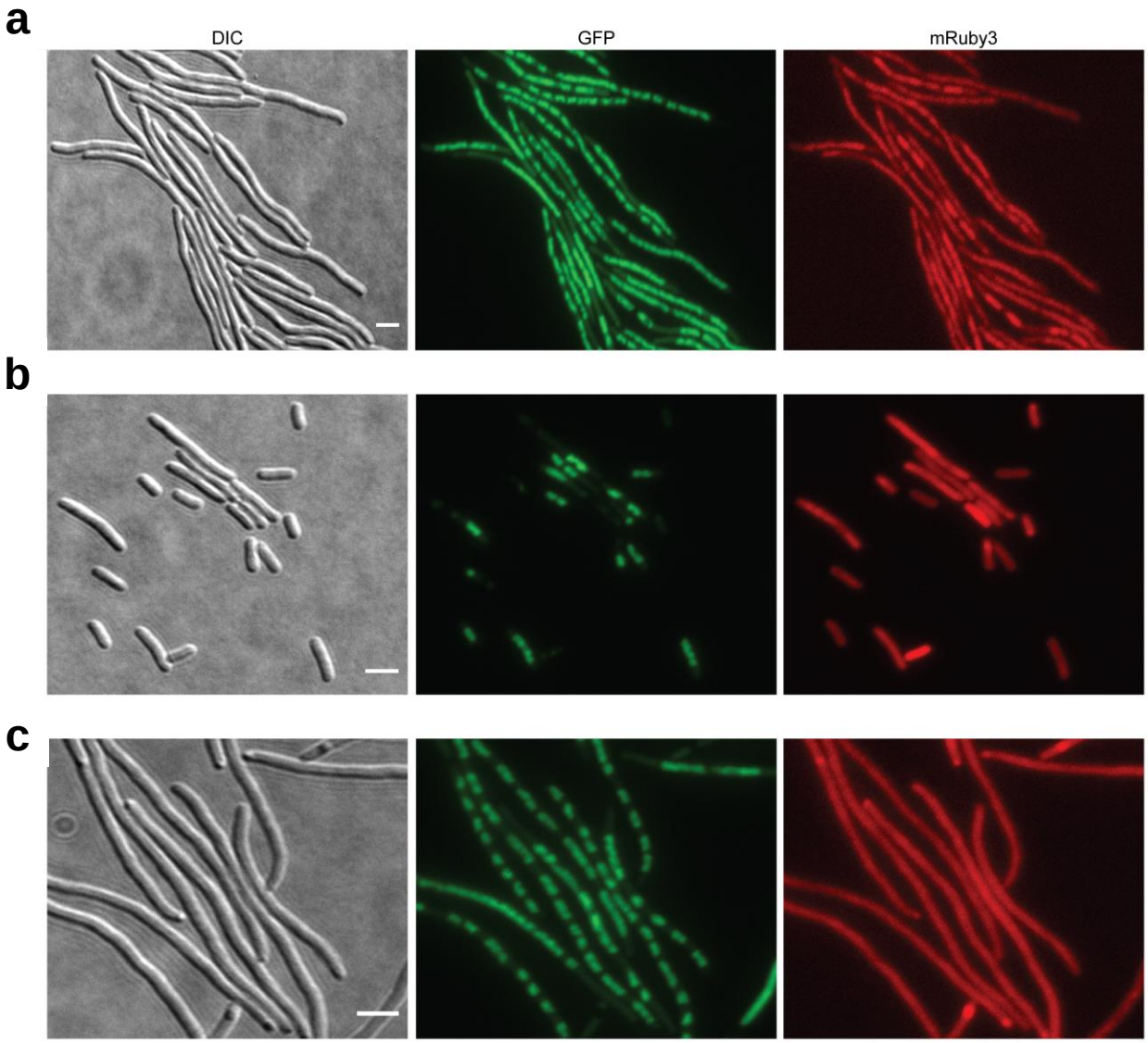

Figure 35. *In vivo* co-localization of MinC$^{N\text{-term+linker}}$-bZIP in *hu-gfp E. coli* cells. Microscopy images of *hu-gfp E. coli* cells transformed with the following constructs; a) MinC$^{N\text{-term+linker}}$-bZIP-mRuby3, b) MBP-bZIP-mRuby3

and c) MinC$^{N\text{-}term}$-bZIP-mRuby3. Protein expression was induced with 100 μM IPTG for 3 hours. Scale bar = 3 μm. Microscopy images were taken by Emir Bora Akmeriç.

2.2. MinE-eYFP fusion protein characterization

2.2.1. Overexpression of MinC^{G10D}DE-eYFP in a ΔminB strain exhibits a lethal phenotype

When *E. coli* MG1655 Δ*minB* strain was transformed with a pBAD33-MinC^{G10D}DE-eYFP construct, at the highest arabinose induction concentration (0.1 %), I found cells exhibiting Sep (-) phenotype (**Figure 36a**) and die (a lethal phenotype) in the cell viability spot assay. An earlier study has shown that MinC^{G10D} has impaired binding to FtsZ, suggesting that the septum ring can form at any position inside the cell giving rise to mini-cells and variably sized nucleated cells (a viable phenotype) (21,22,79). To eliminate the observed discrepancy, the *E. coli* MG1655 Δ*minB* strain was transformed this time with a pBAD33-MinC^{G10D}DE construct and performed the cell viability spot assay again. This time, I found cells exhibiting Sep (+) phenotype (viable phenotype) (**Figure 36b**). These observations hinted to me that the C-terminal tagging of MinE with eYFP impaired MinE's function. With these observations as the starting point, I looked into the available literature and tried to gain insights regarding the functional impairment of MinE fusion proteins. I found two studies from de Boer *et al*. who made similar observations like me yet in a different context (37,58). In those two studies, they did not further investigate to understand the mechanism behind the functional impairment of MinE-GFP. So, to understand the mechanism behind the functional impairment of MinE fusion protein (fluorescent protein fused downstream to MinE), I characterized MinE-eYFP *in vitro, in vivo*, and *in silico*.

2.2.2. In vivo complementation of mini-cell phenotype of a ΔminB strain by MinE-eYFP is impaired compared to untagged MinE

To verify the phenotypic observations made by the earlier studies (37,58), *E. coli* MG1655 Δ*minB* strain transformed with either pBAD33-empty or pBAD33-MinCDE or pBAD33-MinCDE-eYFP plasmid, and *E. coli* MG1655 WT strain transformed with pBAD33-empty plasmid were imaged under the microscope, and cell length and mini-cells were quantified. **Figure 37** shows the schematics of the constructs used for the microscopy studies.

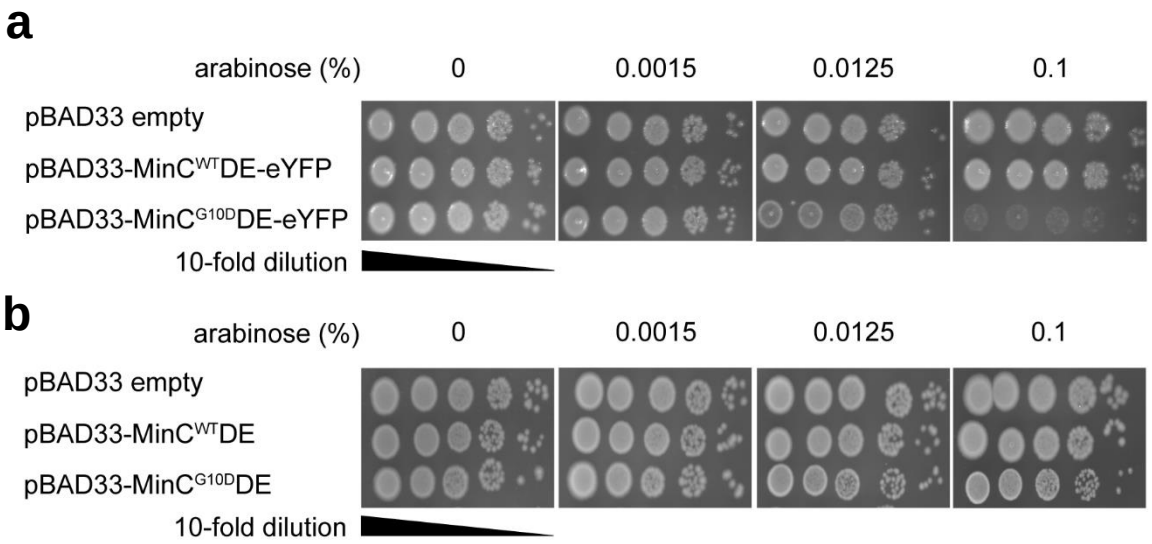

Figure 36. Lethal and viable phenotypes of MinE with and without eYFP, respectively, by cell viability spot assay. The indicated plasmids were transformed into *E. coli* MG1655 Δ*minB* strain. Protein expression was induced with different concentrations of arabinose (0.0015 – 0.1 %).

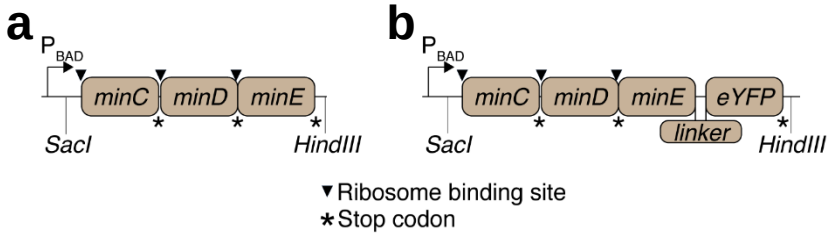

Figure 37. Schematics of pBAD33-MinCDE (a) and pBAD33-MinCDE-eYFP (b) constructs. Between MinE and eYFP, nucleotides specific for *BamHI* restriction enzyme was included followed by additional nine nucleotides coding for amino acids 'GGG' (linker). Image was taken from Palanisamy *et al.* (47) under a Creative Commons Attribution 4.0 International License.

The percentage of cells with cell length >4 μm was found to be the highest in *E. coli* MG1655 Δ*minB* cells transformed with the pBAD33-empty plasmid (17 %), followed by *E. coli* MG1655 Δ*minB* cells transformed with the pBAD33-MinCDE-eYFP plasmid (9.8 %) (**Figure 38**). On the other hand, Δ*minB* cells transformed with the pBAD33-MinCDE plasmid exhibited 3 fold less number of cells with cell length >4 μm compared to the pBAD33-MinCDE-eYFP plasmid (**Figure 38**). In the *E. coli* MG1655 WT strain transformed with the pBAD33-empty plasmid (positive control), only 0.3 % of cells exhibited cell length >4 μm (**Figure 38**).

The percentage of mini-cells with respect to the total number of cells, when transformed with the different plasmid constructs, was also quantified. Again, the percentage of mini-cells was found to be the highest in *E. coli* MG1655 Δ*minB* cells transformed with the pBAD33-

empty plasmid, followed by the pBAD33-MinCDE-eYFP plasmid (**Figure 39**). When *E. coli* MG1655 Δ*minB* cells were transformed with the pBAD33-MinCDE plasmid, the percentage of mini-cells was nearly halved compared to the pBAD33-MinCDE-eYFP plasmid (**Figure 39**).

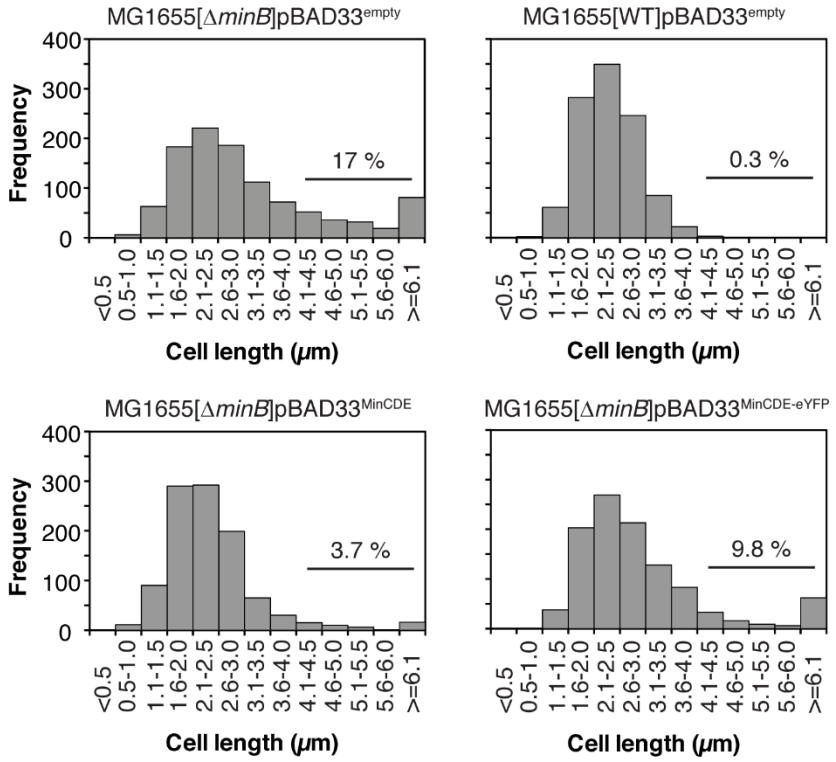

Figure 38. Histograms showing the cell length frequencies after transforming *E. coli* MG1655 WT and Δ*minB* strains with the indicated constructs. Protein expression was induced with 0.0001 % arabinose for 3 hours. The percentages in histograms represent cells with cell length >4 μm. Image was taken from Palanisamy *et al.* (47) under a Creative Commons Attribution 4.0 International License.

2.2.3. MinE-eYFP is vulnerable to aggregation

In order to have a better mechanistic understanding of MinE-eYFP's functional impairment, and to have better control over the protein levels in the assays, we moved for *in vitro* characterization of the proteins. The proteins purified in the present study, by default, were overexpressed in *E. coli* Rosetta™ (DE3) pLysS strain at 37 ºC for 3 hours. We observed that MinE when expressed alone, only half of the protein remained in the supernatant (soluble) (**Figure 40**). eYFP, on the other hand, when expressed alone most of the protein remained in the supernatant (**Figure 40**). By fusing eYFP downstream to MinE, we found that all the proteins were lost in the pellet (insoluble) during ultracentrifugation of the cell lysate (**Figure 40**). Microscopy analysis of *E. coli* Rosetta™ (DE3) pLysS strain expressing MinE-eYFP at

37 ºC for 3 hours showed the presence of inclusion bodies (**Figure 41**). To avoid aggregation, MinE-eYFP was overexpressed at 18 ºC for 12 hours for the protein purification. Similar observation was also made when MinE was fused downstream with either GST (MinE-GST; glutathione S-transferase) or MBP (MinE-MBP; maltose-binding protein) albeit in the case of MBP nearly 1/3rd of the protein was found in the supernatant (**Figure 40**).

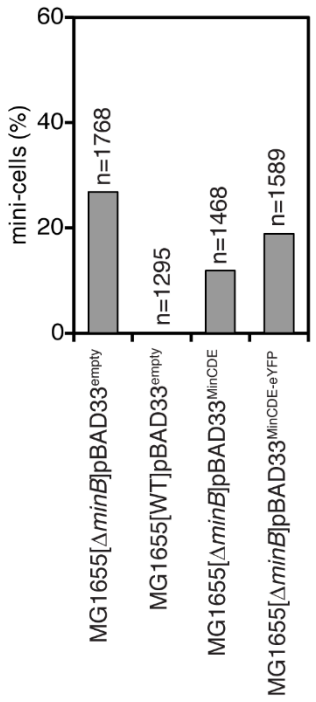

Figure 39. Bar plot showing mini-cells (in %) observed after transforming *E. coli* MG1655 WT and Δ*minB* strains with the indicated constructs. n = total number of cells. Image was taken from Palanisamy *et al.* (47) under a Creative Commons Attribution 4.0 International License.

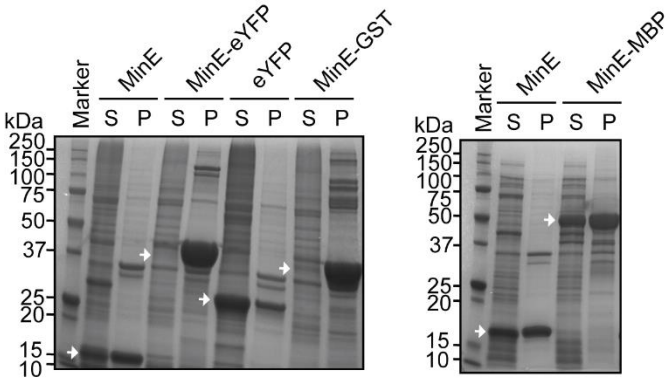

Figure 40. MinE-eYFP is prone to aggregation and is found in the insoluable fraction. Representative Coomassie-stained SDS-PAGE gels showing soluable and insoluable fractions of proteins when overexpressed in *E. coli* Rosetta™ (DE3) pLysS strain at 37 ºC with the indicated constructs. Image was taken from Palanisamy *et al.* (47) under a Creative Commons Attribution 4.0 International License. The white arrow indicates the band representing the overexpressed protein, and for the simplicity, the arrow is shown only next to the soluble fraction.

Considering MinE-eYFP's tendency to form aggregates *in vivo*, we studied *in vivo* localization of MinE-eYFP under two different protein expression levels. For this study, the pBAD33-MinCDE-eYFP plasmid was transformed into Δ*minB* strain and the protein expression was induced with either 0.0001 % or 0.1 % arabinose. With the low arabinose concentration, normal pole-to-pole oscillations and formation of E-rings were observed in nearly 95 % of cells (**Figure 42**). On the other hand, with the high arabinose concentration, pole-to-pole oscillations were irregular and/or stationary fluorescent clusters were observed in nearly 90 % of cells (**Figure 42**). Moreover, the cells were extremely long compared to Δ*minB* cells transformed with the pBAD33-MinCDE plasmid at 0.1 % arabinose concentration (**Figure 43**).

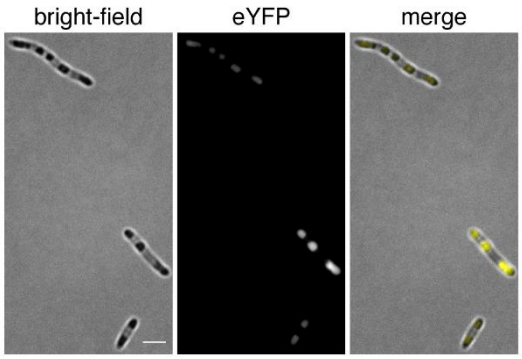

Figure 41. MinE-eYFP forms inclusion bodies *in vivo* at high concentrations. Representative fluorescence microscopy image showing the presence of inclusion bodies when MinE-eYFP was overexpressed in *E. coli* Rosetta™ (DE3) pLysS strain at 37 ºC for 3 hours. Scale bar = 3 μm. Image was taken from Palanisamy *et al.* (47) under a Creative Commons Attribution 4.0 International License.

2.2.4. MinE-eYFP cannot dislodge MinC from MinD as well as untagged MinE

To compare the ability of MinE and MinE-eYFP in displacing MinC from MinD, I performed the liposome co-sedimentation assay. MinD is recruited to the liposome in the presence of ATP provided no MinE is present in the reaction mixture. MinC too gets recruited to the liposomes *via* MinD and found in the pellet fraction when the reaction mixture was centrifuged. The displacement of MinC from MinD was studied with varying concentrations of MinE or MinE-eYFP. At 1 μM MinE concentration, nearly 95 % of MinC was displaced from MinD. On the other hand, MinE-eYFP was found to displace only ~40 % of MinC from MinD at the same concentration (**Figure 44**).

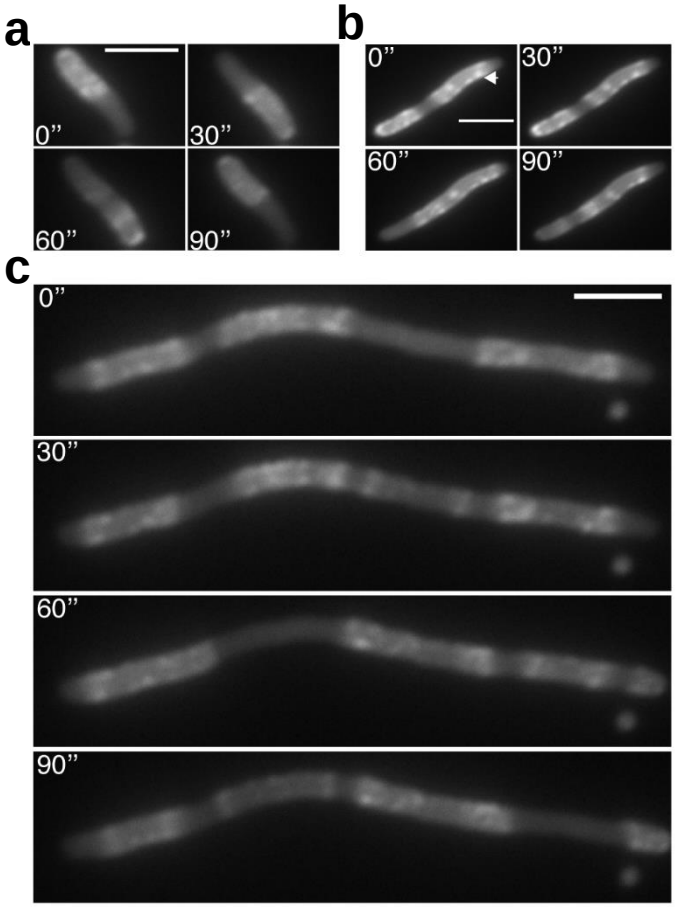

Figure 42. Fluorescence time-lapse microscopy images of *E. coli* MG1655 Δ*minB* strain transformed with pBAD33-MinCDE-eYFP plasmid, showing MinE-eYFP localization at 0.0001 % (a) and 0.1 % (b, c) arabinose induction levels. Scale bar = 3 μm. Arrow indicates a stationary fluorescent cluster. Image was taken from Palanisamy *et al.* (47) under a Creative Commons Attribution 4.0 International License.

2.2.5. MinE-eYFP cannot dislodge MinD from the membrane as well as untagged MinE

In the previous experimental setup, we cannot discern whether MinE or MinE-eYFP can enhance the ATPase activity of MinD as MinC, if present, has to be first displaced by MinE or MinE-eYFP before enhancing the ATPase activity of MinD. Although MinE-eYFP is impaired in displacing MinC, it could still be that it enhances the ATPase activity of MinD as well as untagged MinE. To study this, we performed the liposome co-sedimentation assay again but this time omitting MinC in the reaction. We found that MinE at 0.25 μM concentration, a 2-fold increase in displacement of MinD from the membrane was observed compared to having no MinE (**Figure 45**). MinE-eYFP, on the other hand, a 2-fold increase in the displacement of MinD from the membrane was observed only at 1 μM concentration compared to having no MinE-eYFP (**Figure 45**).

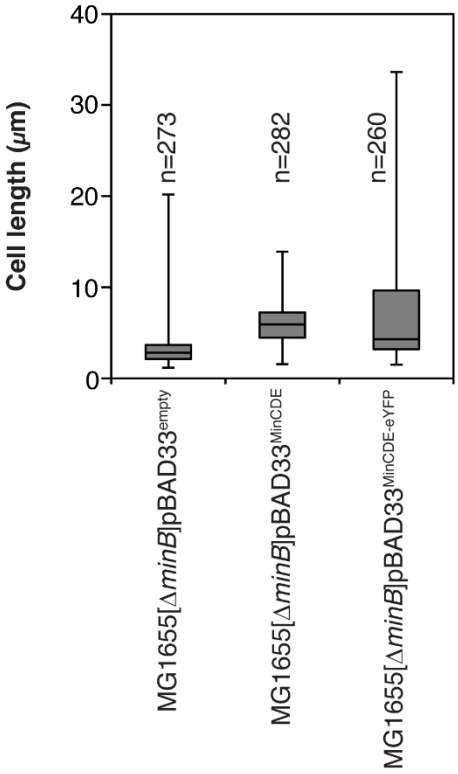

Figure 43. Expression of MinE-eYFP at high arabinose induction level (0.1 %) results in cell elongation. Box and whiskers plot showing the cell length when *E. coli* MG1655 Δ*minB* strain was transformed with the indicated plasmids and the protein expression was induced with 0.1 % arabinose. n = total number of cells quantified. Image was taken from Palanisamy *et al.* (47) under a Creative Commons Attribution 4.0 International License.

2.2.6. MinE-eYFP is able to bind to MinD

From the liposome co-sedimentation assays, we cannot find out whether the MinE-eYFP's impairment in displacing MinD from the membrane is due to loss of MinD binding or due to MinE-eYFP's inability to induce the ATPase activity of MinD. To answer this question, we performed the pull-down assay. For this assay, we used a variant of MinD ($MinD^{D40A\Delta10}$) which lacks the membrane targeting sequence and also aspartate at position 40 was mutated to alanine. This variant cannot hydrolyze ATP and remains soluble, and is ideal for studying the binding of MinE to MinD (32). The assay was performed in the presence of ADP or ATP. It was found that $MinD^{D40A\Delta10}$ mutant binds to MinE 8.4-fold more in the presence of ATP compared to ADP (**Figure 46**). On the other hand, $MinD^{D40A\Delta10}$ mutant was found to bind to MinE-eYFP 3.5-fold more in the presence of ATP compared to ADP (**Figure 46**). Taken together the data from the liposome co-sedimentation and pull-down assays, they suggest that MinE-eYFP, despite able to bind to MinD, is unable to induce the ATPase activity of MinD.

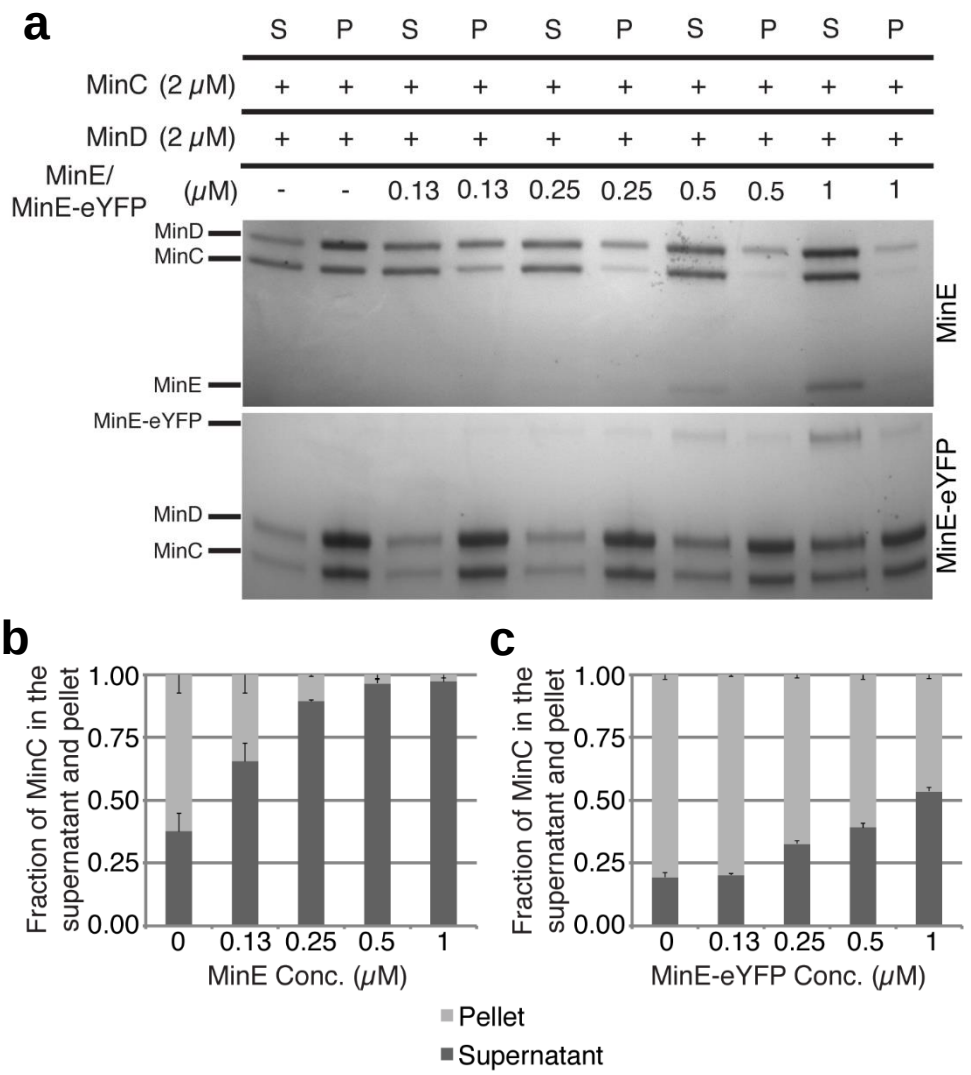

Figure 44. MinE-eYFP shows impairment in displacing MinC from MinD in the co-sedimentation assay. (a) Representative Coomassie-stained SDS-PAGE gels after co-sedimentation assay performed with fixed concentration of MinD and MinC and increasing concentration of MinE and MinE-eYFP. (b, c) Bar plots showing quantification of MinC (in %) in the supernatant (S) and the pellet (P) with increasing MinE (b) and MinE-eYFP (c) concentrations. Experiments were done thrice and mean±SEM is plotted in the graph. Image was taken from Palanisamy *et al.* (47) under a Creative Commons Attribution 4.0 International License.

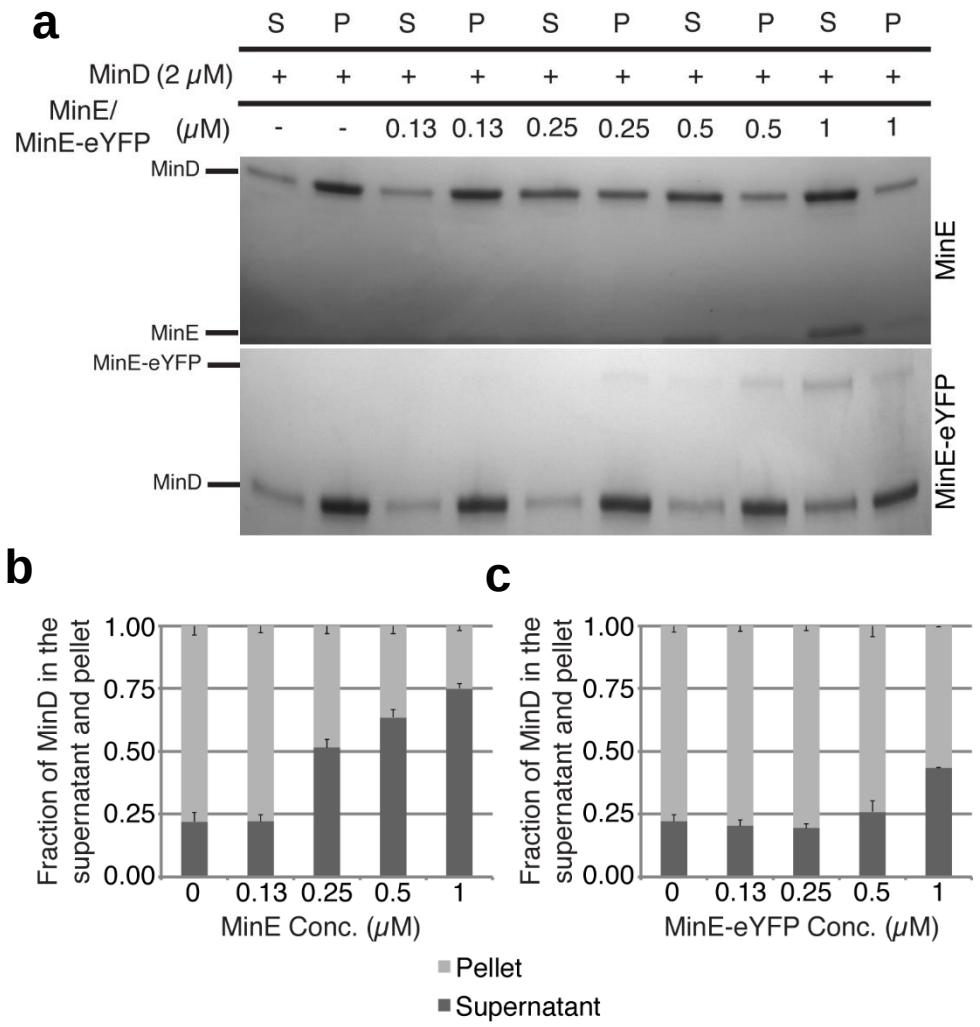

Figure 45. MinE-eYFP shows impairment in displacing MinD from the membrane in the co-sedimentation assay. (a) Representative Coomassie-stained SDS-PAGE gels after co-sedimentation assay performed with fixed concentration of MinD and increasing concentration of MinE and MinE-eYFP. (b, c) Bar plots showing quantification of MinD (in %) in the supernatant (S) and the pellet (P) with increasing MinE (b) and MinE-eYFP (c) concentrations. Experiments were done thrice and mean±SEM is plotted in the graph. Image was taken from Palanisamy *et al.* (47) under a Creative Commons Attribution 4.0 International License.

2.2.7. Computational analysis of MinE-eYFP predicted reduced accessibility of membrane targeting sequence and R21 in MinE

As stated in the introduction, MinE is a highly dynamic protein and possesses three functional regions namely; 1) N-terminal membrane targeting sequence, 2) anti-MinCD domain and 3) dimerization domain. Affecting the function of any of these regions can cause functional impairment in MinE-eYFP. We went for a computational approach to further identify the differences between MinE and MinE-eYFP in the aforementioned functional regions. Dr. Mehmet Ali Öztürk performed coarse-grained replica-exchange molecular

dynamics simulations with modeled MinE and MinE-eYFP structures and studied the accessibility of the functional regions from the generated ensembles. He found that the accessibilities of the N-terminal membrane targeting sequence and the amino acid at position 21 in the anti-MinCD domain, needed for the activation of the MinD ATPase activity, were reduced in the fusion protein. He further found that the dimerization interface of MinE in MinE-eYFP was not affected. To test these computational predictions, I performed further *in vitro* experiments.

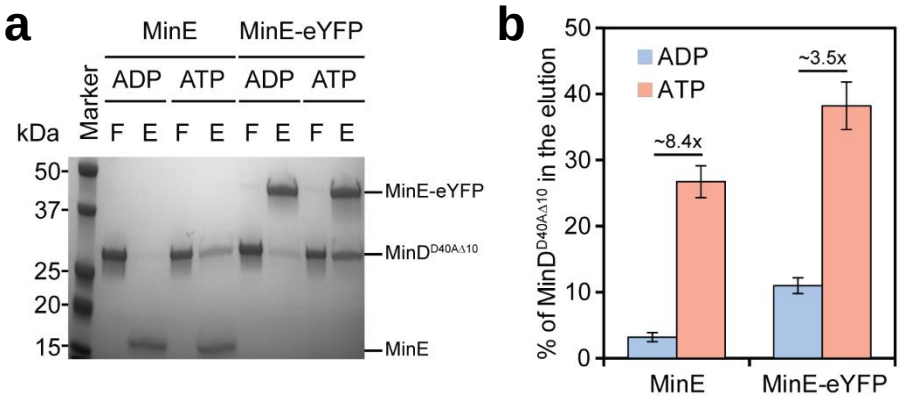

Figure 46. MinE-eYFP binds to $MinD^{D40A\Delta10}$ in the pull-down assay. (a) Representative Coomassie-stained SDS-PAGE gel after the pull-down assay of $MinD^{D40A\Delta10}$ with either MinE or MinE-eYFP in presence of ADP or ATP. (b) Bar plot showing quantification of $MinD^{D40A\Delta10}$ (in %) in the elution. Experiments were done thrice and mean±SEM is plotted in the graph. Image was taken from Palanisamy *et al.* (47) under a Creative Commons Attribution 4.0 International License.

2.2.8. MinE-eYFP is not able to bind to the membrane as predicted computationally

Shih *et al.* have shown that direct MinE membrane binding and self-assembly properties of MinE are needed for the proper functioning of the Min system in *E. coli* (28,82). To study the membrane binding ability of MinE-eYFP, I performed membrane-binding assay as shown by Shih *et al.* (28). The N-terminal membrane targeting sequence of MinE is in an equilibrium between 'closed' and 'open' states. In the 'open' state, MinE can interact with the membrane and dissociate in the 'closed' state. So, in the membrane-binding assay, a small fraction of MinE is always found in the pellet. I performed the assay in the presence and absence of liposomes. I found that with the presence of liposomes, the recruitment of MinE to the pellet was increased by ~4-fold (**Figure 47**). On the other hand, no significant difference was seen in the recruitment of MinE-eYFP to the pellet with the presence or absence of liposomes (**Figure 47**). Moreover, the percentage of MinE-eYFP in the pellet was high both in the presence and absence of liposomes indicating aggregation. I questioned whether MinE-eYFP's inability to

induce the ATPase activity of MinD in the liposome co-sedimentation assay is due to a lack of membrane binding. To understand further, I created and purified a MinE mutant lacking the first 12 amino acids responsible for the membrane binding ($MinE^{13-88}$), and performed the liposome co-sedimentation assay with MinD. I found that $MinE^{13-88}$ could efficiently displace MinD from the membrane as well as the MinE WT (**Figure 48**). This observation suggests that direct membrane association by MinE is not needed for activating the ATPase activity of MinD in the liposome co-sedimentation assay.

2.2.9. MinE-eYFP dimerization interface is not affected as predicted computationally

Computational analysis predicted that the dimerization interface of MinE in MinE-eYFP is not affected. To study the dimerization properties of MinE and MinE-eYFP, I performed size-exclusion chromatography. At the studied concentration (13 μM), a major proportion of MinE was found as a tetramer in line with the previous finding (83), while MinE-eYFP was found as a dimer (**Figure 49**). This observation complements our computational prediction that the dimerization interface is not affected.

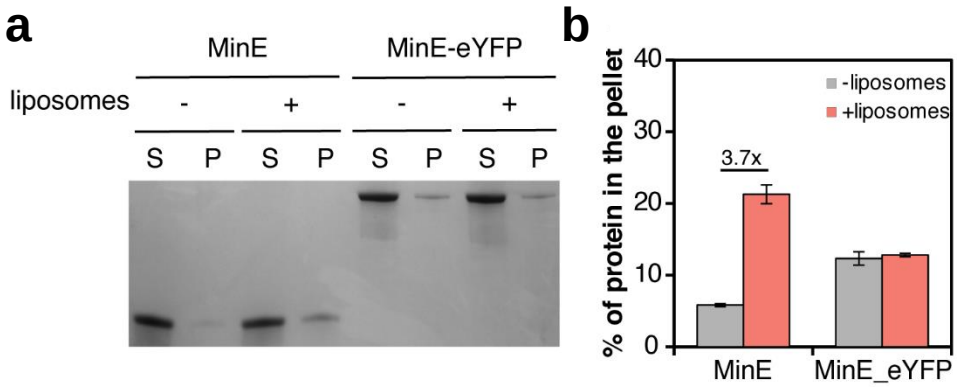

Figure 47. MinE-eYFP binding to membrane is impaired. (a) Representative Coomassie-stained SDS-PAGE gel after performing the membrane-binding assay with MinE or MinE-eYFP in presence or absence of liposomes. (b) Bar plot showing quantification of MinE and MinE-eYFP (in %) in the pellet. Experiments were done thrice and mean±SEM is plotted in the graph. Image was taken from Palanisamy *et al.* (47) under a Creative Commons Attribution 4.0 International License.

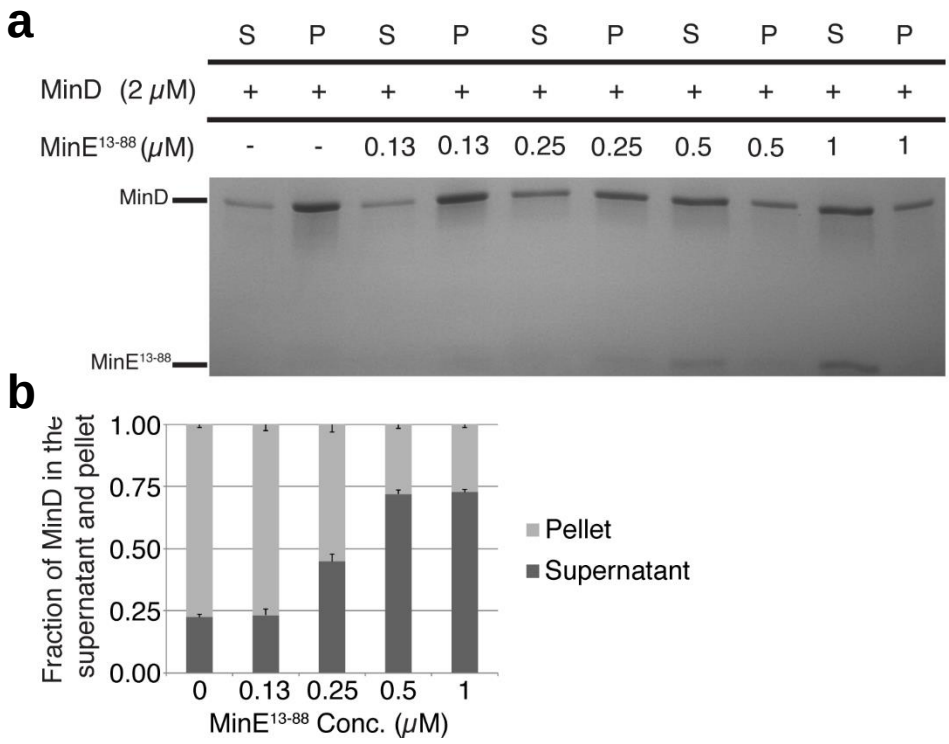

Figure 48. Membrane binding of MinE is not needed for enhancing the ATPase activity of MinD. (a) Representative Coomassie-stained SDS-PAGE gel after co-sedimentation assay performed with fixed concentration of MinD and increasing concentration of $MinE^{13-88}$. (b) Bar plot showing quantification of MinD (in %) in the supernatant (S) and the pellet (P) with increasing $MinE^{13-88}$ concentration. Experiments were done thrice and mean±SEM is plotted in the graph. Image was taken from Palanisamy *et al.* (47) under a Creative Commons Attribution 4.0 International License.

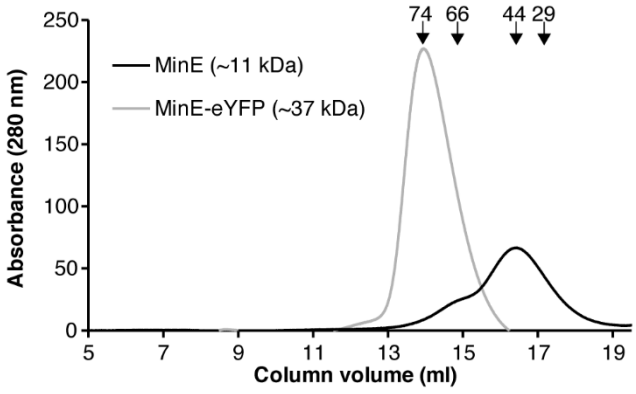

Figure 49. MinE-eYFP forms dimers. Size exclusion chromatography analysis of MinE and MinE-eYFP, both at 13 μM concentration. Bovine serum albumin (BSA) and carbonic anhydrase (CA) were used as size markers and are indicated with black arrow with sizes 66 and 29 kDa, respectively. Image was taken from Palanisamy *et al.* (47) under a Creative Commons Attribution 4.0 International License.

2.3. SiMPl plasmid toolbox

2.3.1. SiMPl plasmid pair based on kanamycin

For splitting aminoglycoside phosphotransferase (APT), which confers resistance against kanamycin, a previously published split-site was chosen (84). **Figure 50** shows the plasmid maps of SiMPl^{k} plasmid pair based on kanamycin.

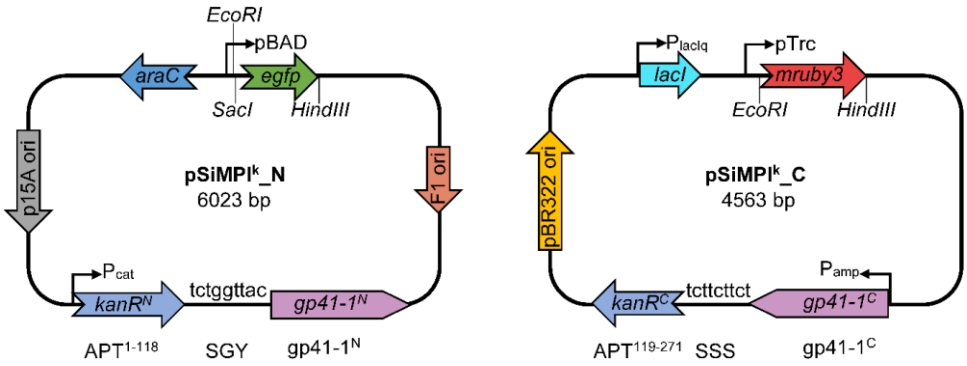

Figure 50. Plasmid maps of SiMPl^{k} plasmid pair based on kanamycin. DNA fragments corresponding to amino acid residues 1-118 and 119-271 of aminoglycoside phosphotransferase (APT) were amplified independently and assembled with DNA fragments of gp41-1 N and C-inteins, respectively, and with the respective backbones (pBAD33 or pTrc99a) by the Gibson Assembly® method. Figure shows important features found in pSiMPl^{k}_N (**a**) and pSiMPl^{k}_C (**b**) plasmids constituting the SiMPl^{k} plasmid pair. Image was taken from Palanisamy *et al.* (85) under a Creative Commons Attribution 4.0 International License.

The assembled pSiMPl^{k}_N and pSiMPl^{k}_C plasmids were transformed into *E. coli* cells either individually or together. It could be seen that only when both the pSiMPl^{k}_N and pSiMPl^{k}_C plasmids were transformed together, colonies appear on a kanamycin containing nutrient agar plate (**Figure 51**).

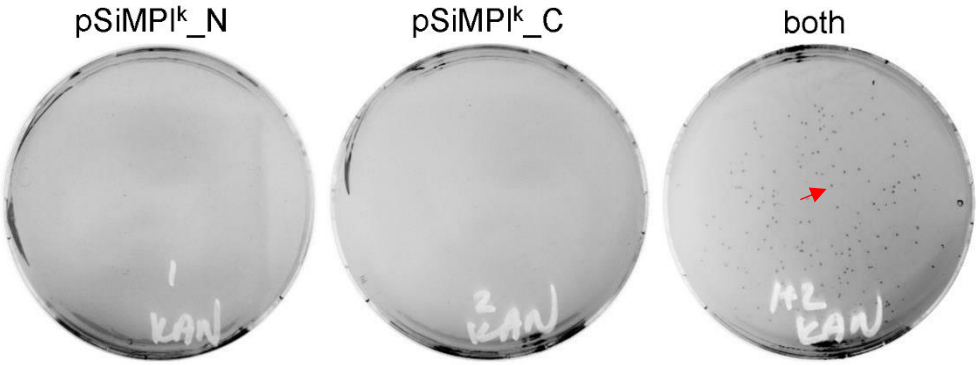

Figure 51. Agar plate images showing the growth of bacterial colonies only when both the pSiMPl^{k}_N and pSiMPl^{k}_C plasmids were transformed together into TOP10 *E. coli* cells. Hundred ng each of Gibson assembled® pSiMPl^{k}_N and pSiMPl^{k}_C plasmids were transformed into TOP10 *E. coli* cells either individually or together by

the heat shock method and screened on a nutrient agar plate containing kanamycin. An example colony is pointed with a red arrow in the figure.

Two colonies were randomly picked from the plate and did an overnight culture individually in a nutrient broth containing kanamycin. The plasmid DNA from the respective clones was isolated and then visualized by running them on a 1 % agarose gel stained with ethidium bromide. Both the pSiMPl^{k}_N and pSiMPl^{k}_C plasmids could be seen (**Figure 52**).

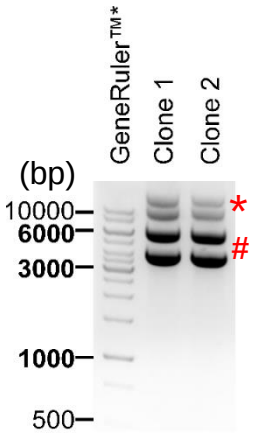

Figure 52. Ethidium bromide-stained agarose gel showing the presence of both the SiMPl^{k} plasmids. Two colonies were randomly chosen, mini-preped and the total plasmid DNA was ran on 1 % agarose gel. From the gel it could be seen that both the pSiMPl^{k}_N and pSiMPl^{k}_C plasmids are present. Both these plasmids exhibited supercoiled (represented by #) and nicked/linear structures (represented by *). Image was taken and modified from Palanisamy *et al.* (85) under a Creative Commons Attribution 4.0 International License.

The presence of both the plasmids in *E. coli* cells was further validated by performing a PCR. Primers annealing to *egfp* and *mruby3* genes were used for the PCR validation. Additionally, primers annealing to full-length *kanR* gene (APT) were also used. *E. coli* cells transformed with both the SiMPl^{k} plasmids, when used as a template for the PCR, DNA bands appeared for both the *egfp* and *mruby3* genes while no band was seen when primers were used for the full-length *kanR* gene (**Figure 53**).

The presence of both the plasmids in *E. coli* cells was also further validated by performing a fluorescence microscopy. *E. coli* cells transformed with both the SiMPl^{k} plasmids were induced for the expression of EGFP and mRuby3 by adding arabinose and IPTG, respectively, to the culture. Fluorescence microscopy was performed by embedding the induced cells on an agar pad. It could be seen that *E. coli* cells expressed both EGFP and mRuby3 upon induction (**Figure 54**).

To confirm that inteins are needed to reconstitute APT, two mutants were created; the first cysteine in the N-terminal of gp41-1 N intein was mutated to alanine and the final asparagine in the C-terminal of gp41-1 C intein was mutated to alanine as well. These residues were shown to play an important role in the intein function by an earlier study (86). It was found that mutating asparagine to alanine resulted in a feeble APT activity, as seen by a lesser bacterial growth compared to the WT while mutating cysteine to alanine completely abolished the APT activity (**Figure 55**).

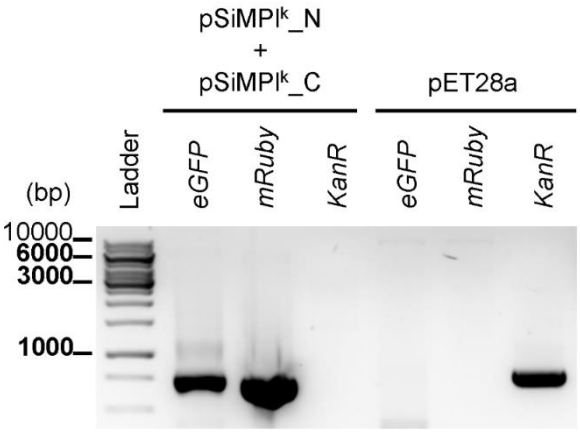

Figure 53. Ethidium bromide-stained agarose gel showing the presence and absence of bands corresponding to the genes of interest after PCR. When SiMPl^k plasmids (pSiMPl^k_N + pSiMPl^k_C) were used as template, bands were seen for *egfp* and *mruby3* genes, while no PCR product was seen for the full length *kanR* gene. pET28a plasmid DNA was used as positive and negative controls for *KanR* and, *egfp* and *mruby3* genes, respectively. Image was taken from Palanisamy *et al.* (85) under a Creative Commons Attribution 4.0 International License.

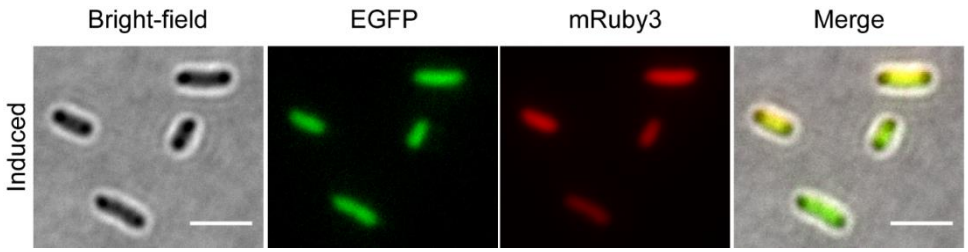

Figure 54. Microscopy images showing the expression of EGFP and mRuby3 by the SiMPl^k plasmids. Culture was grown in a tryptone broth containing kanamycin. After attaining an OD_{600} of 0.5, expression of EGFP and mRuby3 were induced with 0.1 % arabinose and 1 mM IPTG, respectively. Scale: 3 μM. Image was taken and modified from Palanisamy *et al.* (85) under a Creative Commons Attribution 4.0 International License.

Transformation efficiencies of two plasmids with two different selection makers and two plasmids with a single selection marker (*i.e.* with our SiMPl^k plasmids) were compared. It

was found that SiMPl^{k} plasmids outperformed pBAD33+pTrc99a plasmids combination by roughly seven-fold in yielding the number of bacterial transformants (**Figure 56**).

The stability of SiMPl^{k} plasmids, over a long time period, was also studied by continuously sub-culturing *E. coli* TOP10 cells carrying the SiMPl^{k} plasmids into a fresh nutrient broth containing kanamycin every day for over a period of 4 weeks and collecting the bacterial pellets at regular intervals for isolation of the plasmid DNA. It was found that SiMPl^{k} plasmids, like other commonly used plasmids, were stable during the entire study period (**Figure 57**).

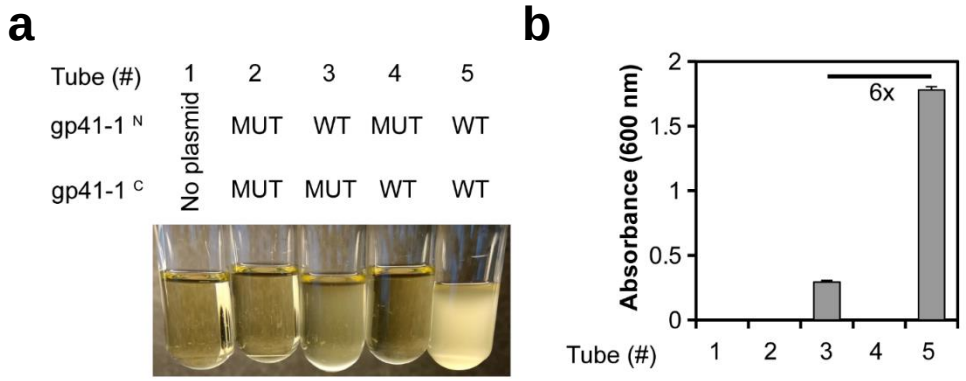

Figure 55. Analysis of intein-mediated reconstitution for the activity of aminoglycoside phosphotransferase (APT). **a**) Nutrient broth showing bacterial growth with SiMPl^{k} gp41-1^{N} wild type (WT) and gp41-1^{C} WT plasmids (tube #5) and, SiMPlk gp41-1^{N} WT and gp41-1^{C} mutant plasmids (tube #3). **b**) Bar graph showing quantification of bacterial growth with WT and mutant SiMPl^{k} plasmids. Experiments were performed three times and mean±SEM is plotted in the graph. gp41-1^{N} MUT = first cysteine in the gp41-1 N-intein mutated to alanine. gp41-1^{C} MUT = final asparagine in the gp41-1 C-intein mutated to alanine. Image was taken and modified from Palanisamy *et al.* (85) under a Creative Commons Attribution 4.0 International License.

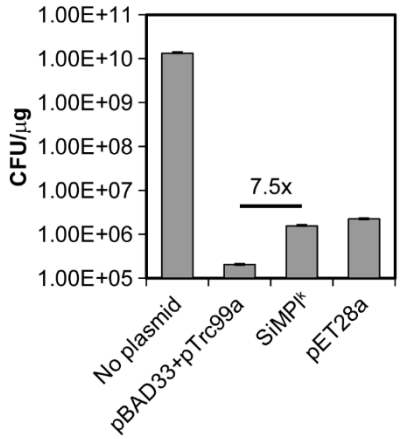

Figure 56. Transformation efficiencies of SiMPl^{k} plasmids and pBAD33+pTrc99a plasmids combination. Bar graph showing the number of colonies obtained after transforming *E. coli* TOP10 chemical competent cells with the corresponding plasmids. Experiments were performed three times and mean±SEM is plotted in the graph.

Image was taken and modified from Palanisamy *et al.* (85) under a Creative Commons Attribution 4.0 International License.

2.3.2. SiMPl plasmid pairs based on chloramphenicol and ampicillin

No previous study exists showing a split version for chloramphenicol acetyltransferase (CAT). To split CAT, I followed a computational approach. More specifically, I looked at the flexibility of individual amino acids in CAT and identified two potential split sites (**Figure 58a**). The flexibility of a residue is directly proportional to the root mean square fluctuation (RMSF) value. Additionally, I also considered only those residues that were surface exposed. For splitting TEM-1 β lactamase (TEM-1βL), which confers resistance against ampicillin, although two works of literature were available, I still went for our computational based approach for the splitting and identified three potential split sites (**Figure 58b**) (87,88). It was found that two out of the two predicted split sites for CAT and two out of the three predicted split sites for TEM-1βL exhibited bacterial growth in a media containing the corresponding antibiotics when transformed with the respective SiMPl plasmids (**Figure 59a-c**). Surprisingly, later it was found that one of the two identified split sites for TEM-1βL namely, K213:V214, exhibited bacterial growth with ampicillin when transformed with only one plasmid containing the first half of TEM-1βL and the N-intein (**Figure 59d**).

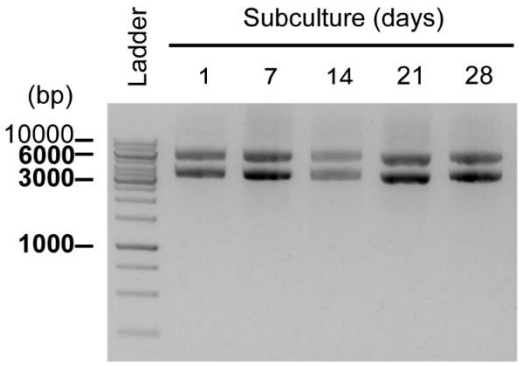

Figure 57. Stability of SiMPl^{k} plasmids. Ethidium bromide-stained 1 % agarose gel showing SiMPl^{k} plasmids isolated from bacterial cultures at regular intervals, which was grown continuously for 28 days. Image was taken from Palanisamy *et al.* (85) under a Creative Commons Attribution 4.0 International License.

For further analysis, split sites E140:N141 (of CAT) and S104:P105 (of TEM-1βL) were considered as SiMPl^{c} and SiMPl^{a} plasmids, respectively. Like for the SiMPl^{k} plasmids, the transformation efficiencies of SiMPl^{c} and SiMPl^{a} plasmids were compared with the transformation efficiency of pBAD33+pTrc99a plasmids combination in *E. coli* TOP10 cells.

It was found that while SiMPl^{c} plasmids yielded 2.3-fold more bacterial transformants compared to the pBAD33+pTrc99a plasmids combination, SiMPl^{a} plasmids yielded 36-fold fewer transformants (**Figure 60**).

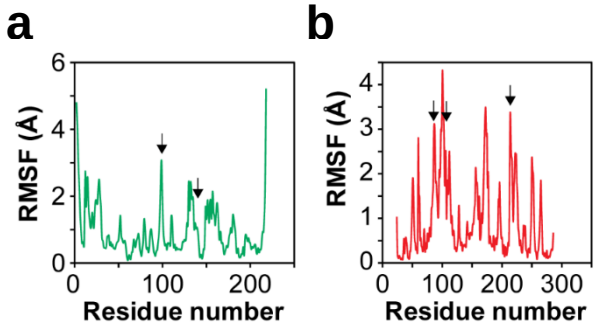

Figure 58. Root mean square fluctuation (RMSF) analysis of chloramphenicol acetyl transferase (**a**) and TEM-1 β lactamase **(b)**. Sites chosen for further experimental studies are indicated by black arrows. Image was taken from Palanisamy *et al.* (85) under a Creative Commons Attribution 4.0 International License.

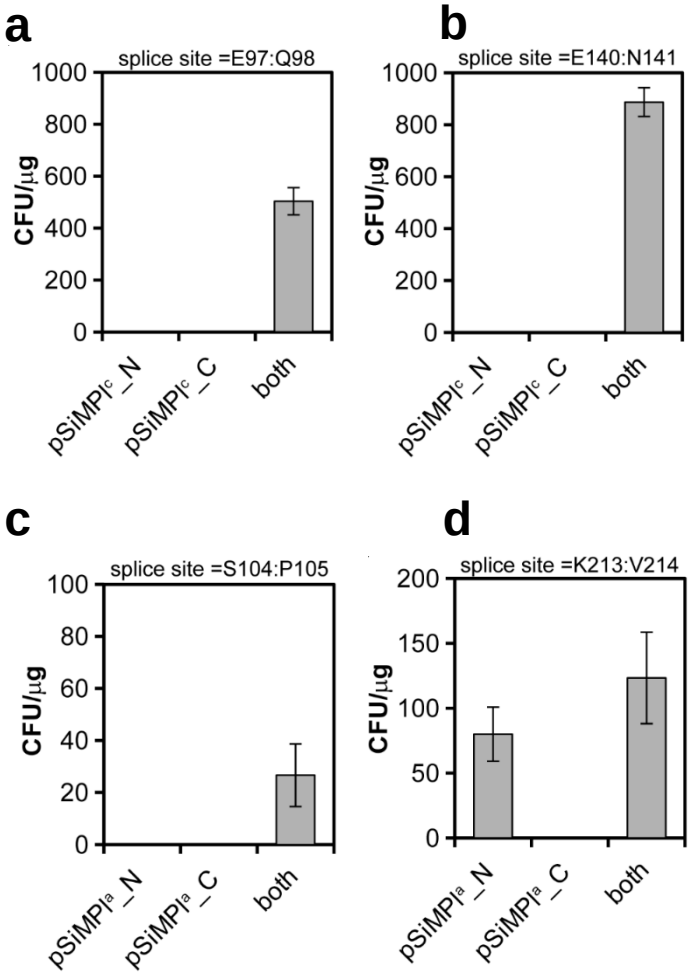

Figure 59. Quantification of bacterial colonies for the predicted splice sites of chloramphenicol acetyl transferase (CAT) and TEM-1 β lactamase (TEM-1βL). (**a**, **b**) Bar graphs showing the number of colonies obtained after

transforming *E. coli* TOP10 cells with the SiMPl plasmids constructed based on the predicted splice sites for CAT. (**c**, **d**) Bar graphs showing the number of colonies obtained after transforming *E. coli* TOP10 cells with the SiMPl plasmids constructed based on the predicted splice sites for TEM-1βL. Experiments were performed three times and mean±SEM is plotted in the graph. Image was taken and modified from Palanisamy *et al.* (85) under a Creative Commons Attribution 4.0 International License.

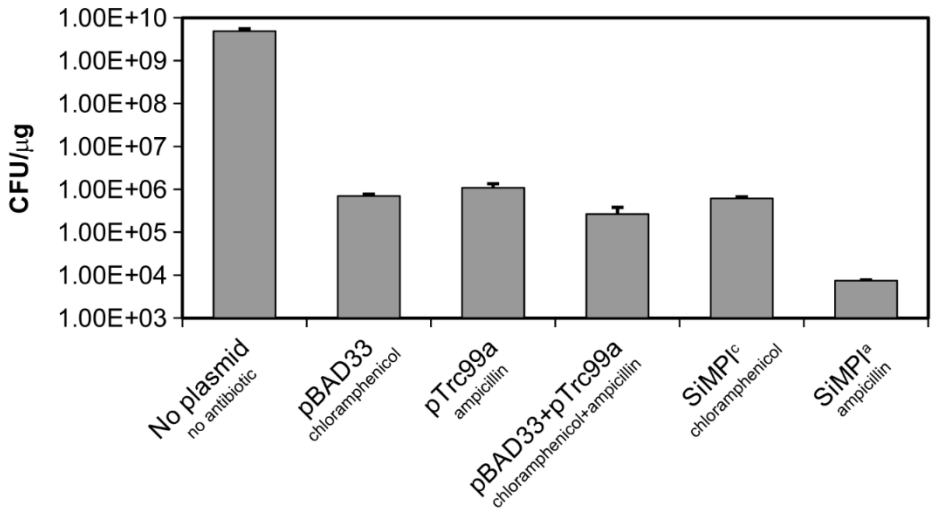

Figure 60. Transformation efficiencies of SiMPl^{c} and SiMPl^{a} plasmids, and pBAD33+pTrc99a plasmids combination. Bar graph showing the number of colonies obtained after transforming *E. coli* TOP10 chemical competent cells with the corresponding plasmids. Experiments were performed three times and mean±SEM is plotted in the graph. Image was taken and modified from Palanisamy *et al.* (85) under a Creative Commons Attribution 4.0 International License.

Similar to the SiMPl^{k} plasmids, the requirement for the intein-mediated reconstitution of CAT and TEM-1βL were studied for the SiMPl^{c} and SiMPl^{a} plasmids, respectively. For this study, additional to the E140:N141 splice site, the E97:Q98 splice site was also considered for CAT. It was found that for the E140:N141 splice site, intein-mediated reconstitution was necessary to get a functional CAT, while for the E97:Q98 splice site bringing the two fragments to a close proximity yielded functional CAT albeit 2.5 times lesser than the reconstituted WT CAT (**Figure 61a, b**). Similar to the E97:Q98 splice site for CAT, the S105:P105 splice site for TEM-1βL yielded functional enzyme by bringing the two fragments together with activity similar to that of the WT reconstituted TEM-1βL.

2.3.3. SiMPl plasmid pairs based on hygromycin and puromycin

We also extended the SiMPl plasmid toolbox for selecting mammalian cell lines carrying two plasmids with a single antibiotic. Unlike for the selection of bacterial cells, only a handful of useable antibiotics exist for selecting the mammalian cells. Two such antibiotics

are hygromycin and puromycin. To split hygromycin phosphotransferase (HPT), which confers resistance towards hygromycin, I took advantage of the splice site information from APT, as HPT and APT perform the same function on different antibiotics belonging to the same antibiotics class. On the sequence level, it was found that HPT and APT do not possess high similarity (**Figure 62a**), but on the secondary structure level, high similarities were observed (**Figure 62b**).

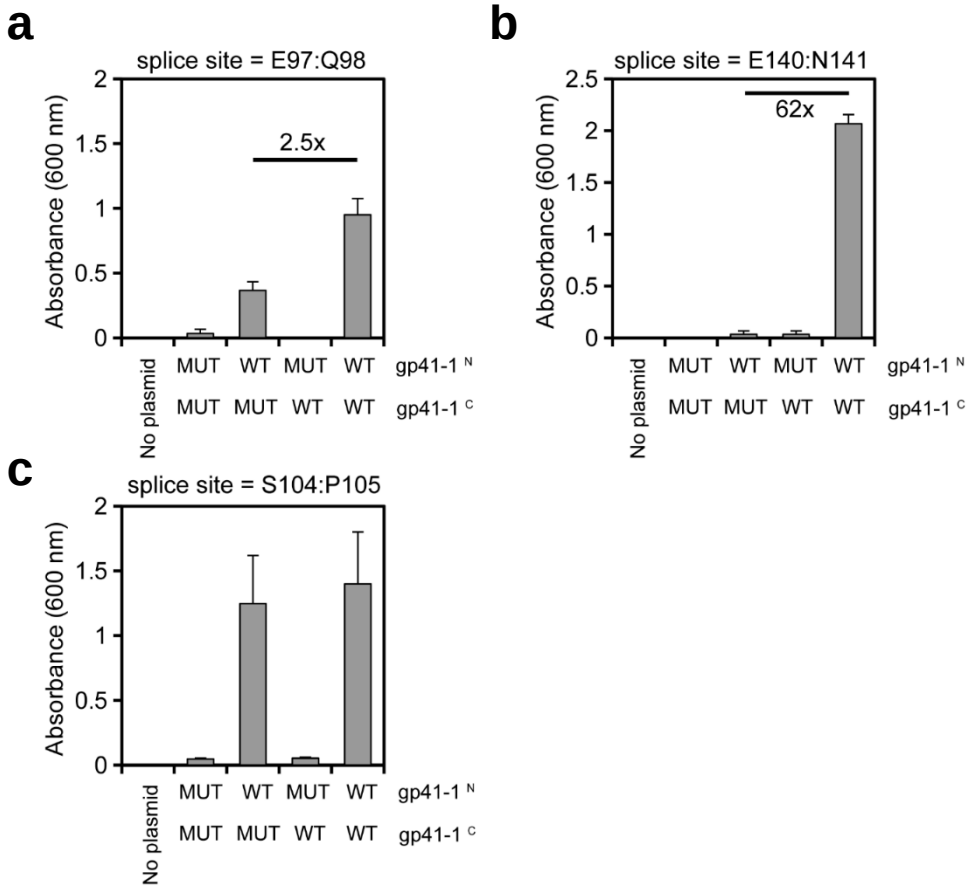

Figure 61. Analysis of intein-mediated reconstitution for the activity of chloramphenicol acetyl transferase (CAT) and TEM-1 β lactamase (TEM-1βL). (**a**, **b**) Bar graphs showing quantification of bacterial growth with WT and mutant SiMPl^{c} plasmids. **c**) Bar graph showing quantification of bacterial growth with WT and mutant SiMPl^{a} plasmids. Experiments were performed three times and mean±SEM is plotted in the graph. gp41-1^{N} MUT = first cysteine in the gp41-1 N-intein mutated to alanine. gp41-1^{C} MUT = final asparagine in the gp41-1 C-intein mutated to alanine. Image was taken from Palanisamy *et al.* (85) under a Creative Commons Attribution 4.0 International License.

Based on the secondary structure comparison between HPT and APT, a splice site (E105:T106) was identified for HPT and was tested for the bacterial selection. Surprisingly, no transformants were obtained. So, I went for the residue-fluctuation based identification of

splice sites for HPT. I identified two potential splice sites namely, D207:N208 and E255:L256 (**Figure 63a**), and tested these sites for the bacterial selection. Only two bacterial colonies were obtained upon transformation of the splice site E255:L256, while no colonies were obtained for the splice site D207:N208. After plasmid isolation from the two colonies, the presence of both the plasmids was verified by running on an agarose gel (**Figure 63b**).

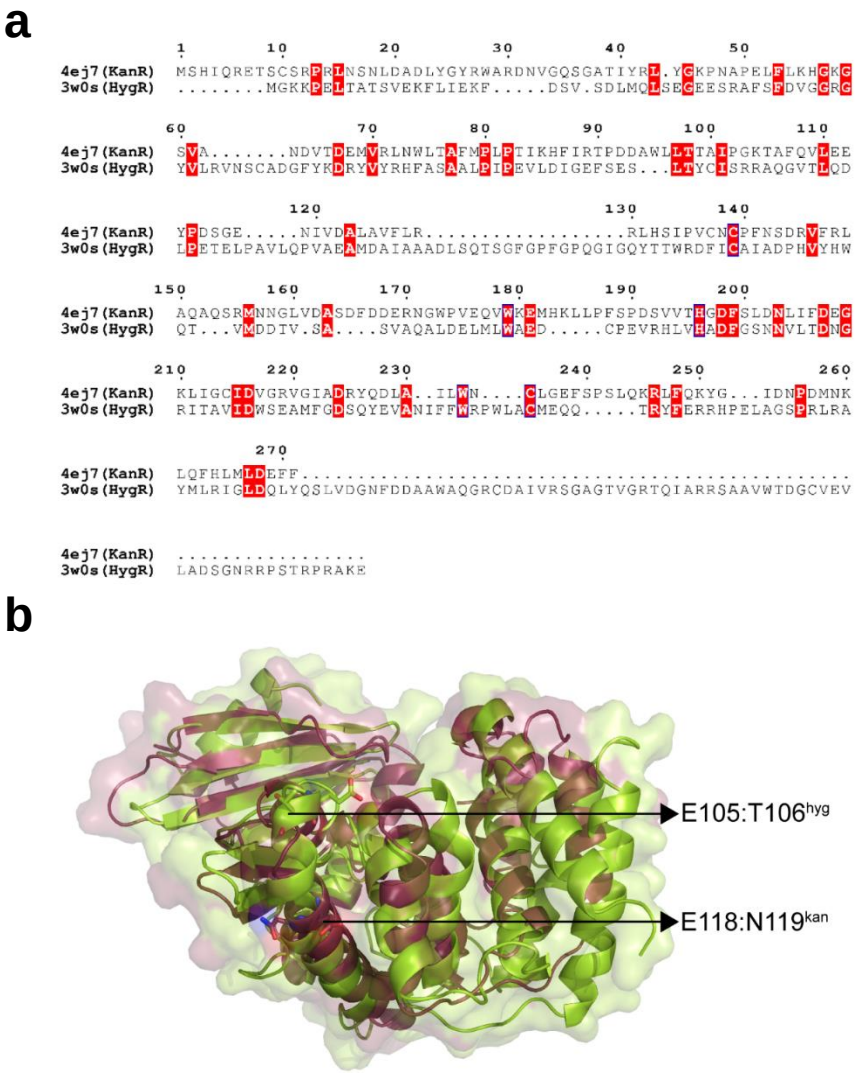

Figure 62. Homology of hygromycin phosphotransferase (HPT; HygR) and aminoglycoside phosphotransferase (APT; KanR) on the amino acid sequence (**a**) and secondary structure (**b**) levels. Image was taken from Palanisamy *et al.* (85) under a Creative Commons Attribution 4.0 International License.

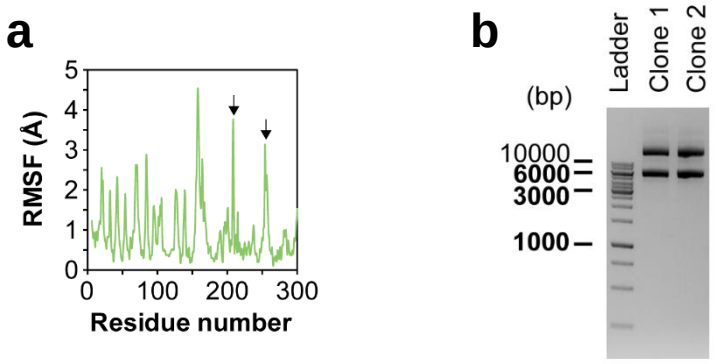

Figure 63. Splice sites for hygromycin phosphotransferase (HPT). (**a**) Root mean square fluctuations (RMSF) of residues of HPT. Predicted sites are indicated with an arrow. (**b**) Ethidium bromide-stained 1 % agarose gel showing SiMPl^{h} plasmids isolated from the two bacterial colonies which grew after the hygromycin selection. Image was taken and modified from Palanisamy *et al.* (85) under a Creative Commons Attribution 4.0 International License.

By sequencing the plasmids from the two bacterial colonies, a mutation was identified in the N- fragment of HPT in both the colonies where proline at position 254 was mutated to glutamine. The effect(s) of P254Q mutation on the structure and function of HPT were further studied. This study was entirely performed by Dr. Mehmet Ali Öztürk. It was found that adding SGYSSS residues to the HPT WT reduces the ligand entry pocket area (**Figure 64b**), while the introduction of P254Q mutation to the HPT with the SGYSSS residues resulted in an increased ligand entry pocket area even higher than that of the HPT WT without the SGYSSS residues (**Figure 64b**). I then tested whether the intein-mediated reconstitution was necessary to yield a functional HPT. Similar to the above-mentioned antibiotics, corresponding mutants were created for HPT and were transformed into *E. coli* TOP10 cells. Unlike the above-mentioned antibiotics, intein-mediated reconstitution was studied here on an agar plate rather than on a broth. It was found that full reconstitution was needed to get a functional HPT (**Figure 65**).

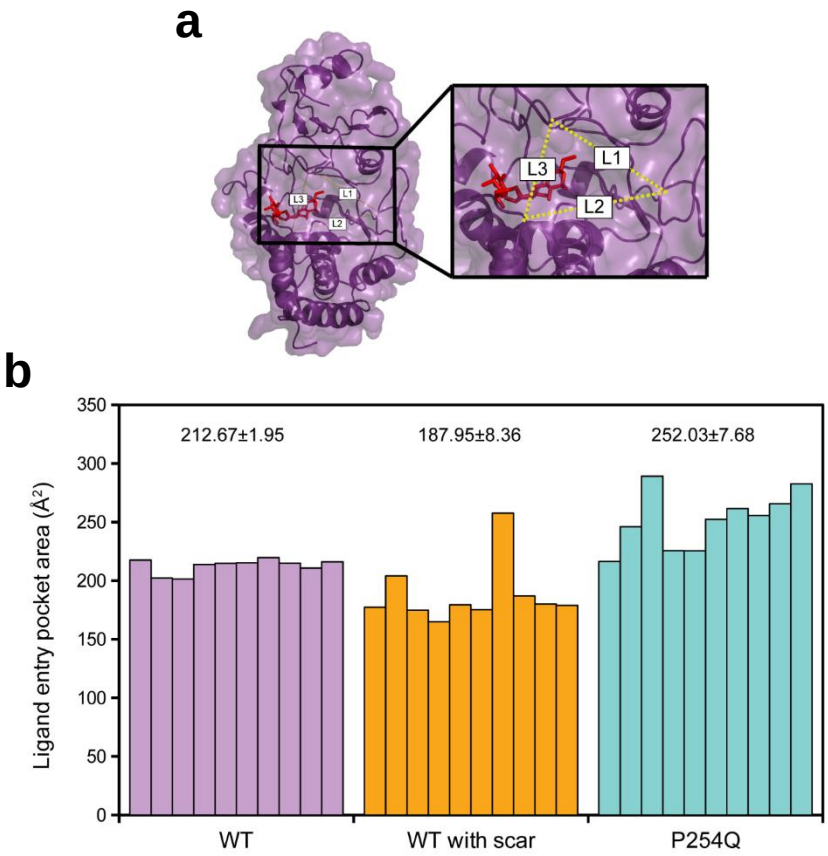

Figure 64. Computational analysis of P254Q mutation on hygromycin phosphotransferase (HPT) function. (**a**) Three-dimensional crystal structure of HPT showing how ligand entry pocket area was calculated. (b) Bar graph showing ligand entry pocket area (Å^2) calculated for the ensembles obtained from the CABS-flex 2.0 webserver (89). Image was taken from Palanisamy *et al.* (85) under a Creative Commons Attribution 4.0 International License. Computational analysis was performed by Dr. Mehmet Ali Öztürk.

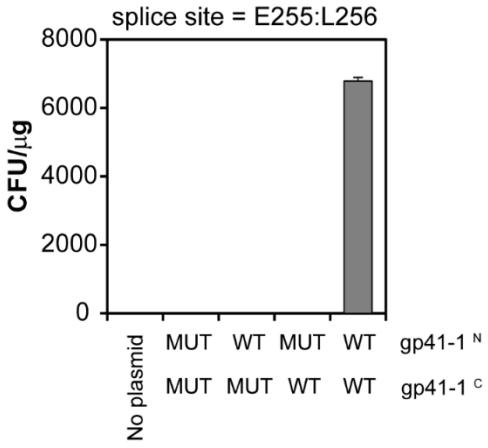

Figure 65. Analysis of intein-mediated reconstitution for the activity of hygromycin phosphotransferase (HPT). Bar graph showing quantification of bacterial transformants with WT and mutant SiMPl^h plasmids. Experiments were performed three times and mean±SEM is plotted in the graph. gp41-1^N MUT = first cysteine in the gp41-1 N-intein mutated to alanine. gp41-1^C MUT = final asparagine in the gp41-1 C-intein mutated to alanine. Image

was taken and modified from Palanisamy *et al.* (85) under a Creative Commons Attribution 4.0 International License.

For identifying splice sites of puromycin N-acetyltransferase (PAT), similar to CAT, TEM-1βL, and HPT, the backbone fluctuation of residues was analyzed and four potential sites were predicted (**Figure 66a**). Out of these four potential sites, only one splice site (V82:E83) yielded bacterial transformants (**Figure 66b**). Two colonies were chosen randomly from the obtained transformants and the presence for two plasmids was verified by running the isolated plasmid on 1 % agarose gel (**Figure 66c**) followed by Sanger sequencing of the isolated SiMPl^{p} plasmids. Mutation analysis of the residues in inteins showed that intein function was not needed albeit the presence of both the N- and C-inteins are needed for bringing the two dysfunctional fragments together to yield the active enzyme (**Figure 67**).

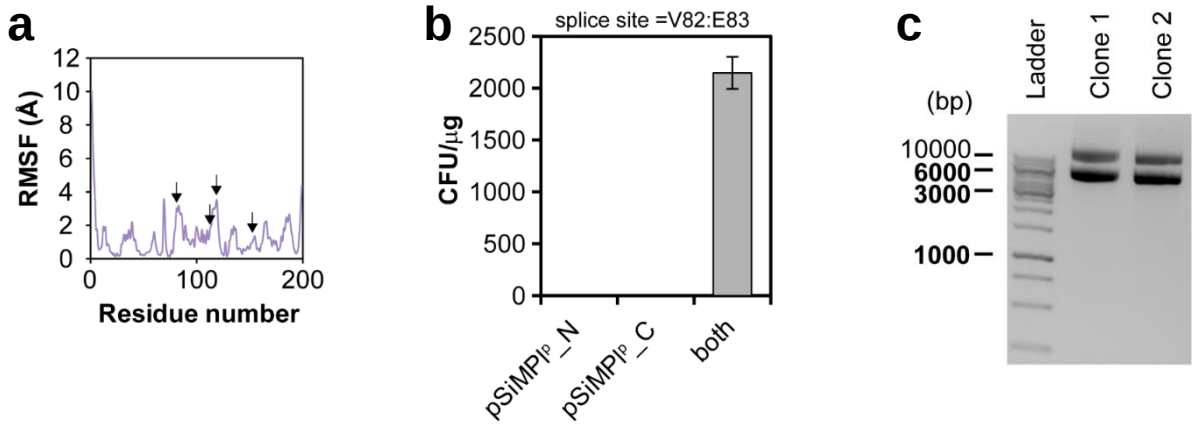

Figure 66. Identification of splice sites for puromycin N-acetyltransferase (PAT). (**a**) Root mean square fluctuations (RMSF) of PAT residues. (**b**) Bar graph showing the number of colonies obtained after transforming *E. coli* TOP10 cells with the V82:E83 splice site for PAT. Experiments were performed three times and mean±SEM is plotted in the graph. (**c**) Ethidium bromide-stained 1 % agarose gel showing SiMPl^{p} plasmids isolated from bacterial transformants. Image was taken and modified from Palanisamy *et al.* (85) under a Creative Commons Attribution 4.0 International License.

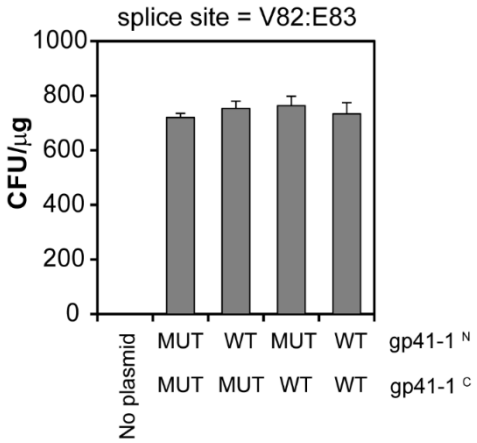

Figure 67. Analysis of intein-mediated reconstitution for the activity of puromycin acetyltransferase (PAT)**.** Bar graph showing quantification of bacterial transformants with WT and mutant SiMPl^{p} plasmids. Experiments were performed three times and mean±SEM is plotted in the graph. gp41-1^{N} MUT = first cysteine in the gp41-1 N-intein mutated to alanine. gp41-1^{C} MUT = final asparagine in the gp41-1 C-intein mutated to alanine. Image was taken and modified from Palanisamy *et al.* (85) under a Creative Commons Attribution 4.0 International License.

3. Discussion

3.1. MinC linker plays a vital role in the DNA binding and FtsZ interaction

For nearly a decade, our group has extensively studied the DNA binding ability of MinD and its potential involvement in chromosome segregation in *E. coli* (1,51,90). Although a few earlier studies suggested that mere entropic forces alone can achieve full chromosome segregation (49,50), we hypothesize that for full chromosome segregation to happen, in addition to the mere entropic forces, an active machinery is needed (51). To further strengthen our hypothesis, in my thesis I found residues/regions on MinC, the binding partner of MinD and co-passenger of the MinD/MinE oscillations, that are either directly or indirectly involved in the DNA binding activity of the MinCD complex. Despite having broadened our understanding of how MinD and MinC bind to the DNA, there are many observations that require further studies.

3.1.1. Appearance of a higher order DNA-bound structure not responsive to MinC in the EMSAs

As previously done by Linda Klauss (1), I found that MinC enhances the DNA-binding ability of MinD in a concentration dependent manner (**Figure 11**). Moreover, I found that the limiting factor in the DNA-binding activity of MinCD is the MinD concentration (**Figure 12**). An earlier study by Di Ventura *et al*. has shown that MinD can bind to the DNA either in the ATP-bound state or in the absence of any nucleotide (51). In my thesis, I observed that MinCD can bind to DNA only when MinD is a dimer, that in the ATP-bound state. In the EMSA experiments, in the presence of MinD or sometimes MinC (**Figure 28**), I see the appearance of a variably intense DNA band with a higher-order structure compared to the unbound DNA, and this band intensity seems not to be affected by MinC (**Figure 16**, **Figure 23**, **Figure 24**, **Figure 26**, **Figure 28** and **Figure 29**). Interestingly, this band appears when the reaction mixture includes ATP or when the nucleotide is absent but not in the presence of ADP (**Figure 13**). At this stage, it is difficult for me to speculate anything about the reason why this band appears. I plan to perform mass spectrometry to find out which protein(s) is(are) responsible for shifting the DNA and bring it to migrate at that position in the gel.

3.1.2. Co-polymer formation and DNA binding

Two groups have previously shown that MinC and MinD form alternating co-polymers *in vitro* (91,92). A study by Lutkenhaus *et al*. has shown using MinC and MinD mutants that these copolymers are not needed for the Min system to function *in vivo* in mid-cell

determination (78). From the EMSA experiments, I found that excess of $MinC^{R133A}$ (a MinC mutant lacking the ability to bind to MinD) (78) was unable to impair the DNA-binding activity of the MinCD complex (**Figure 14**). This observation supports the notion that alternating co-polymers of MinC and MinD are not needed for DNA binding. At first sight, these results are in contradiction with those obtained by Linda Klauss, since she saw that an excess of $MinC^{R133A}$ led to a decrease in DNA binding by MinCD (1). However, it should be noted that she performed liposome co-sedimentation assays and not EMSA assays. In the EMSAs, the protein-DNA complexes are resolved based on mass, shape and total charge; in the liposome co-sedimentation assays, on the other hand, the complexes are resolved purely based on mass. Moreover, from the EMSA experiments, it is difficult to distinguish affinity from avidity. For example, assuming that a DNA binding unit consists of a MinD dimer and $MinC^{WT/R133A}$ heterodimer, though this binding unit cannot form co-polymers, it still can bind to the DNA in close proximity to one another. On the other hand, in the liposome co-sedimentation assays, in order to bring plasmid DNA to the pellet, co-polymer formation on the liposomes might increase the avidity of the MinCD complex for the DNA thereby bringing more DNA to the pellet. Due to these reasons, DNA binding was observed in the EMSA experiments while reduced DNA binding was observed in the liposome co-sedimentation assays with the excess of $MinC^{R133A}$. I conclude that co-polymer formation is not needed for the DNA-binding ability of the MinCD proteins. So far, the alternating co-polymers of MinC and MinD have not been visualized *in vivo* and their functional relevance has yet to be established.

3.1.3. MinC G10 residue in the DNA binding and dimerization

MinC G10 residue has been shown to interact with FtsZ (21,22,79). In my thesis, by performing EMSA experiments, I have shown that mutation of this glycine to aspartic acid nearly abolishes DNA binding (**Figure 16**). This is in line with a previous study from our group (1). Interestingly, however, in liposome co-sedimentation assays, $MinC^{G10D}$ showed reduced DNA pelleting ability (60 % compared to WT), rather than no pelletting (1). From the CD spectroscopy data, it was found that substitution of aspartic acid with glycine did not significantly affect the secondary structural elements of MinC, thereby suggesting that the DNA-binding impairment is purely electrostatic (**Figure 19** and **20**). On the other hand, deletion of the first 20 amino acids in the very N-terminus of MinC did not abolish DNA binding (**Figure 17**), suggesting that G10 does not directly bind to the DNA or its absence can be somehow compensated by a different conformation assumed by the protein. In line with these results, I observed that introduction of the G10D mutation to $MinC^{N\text{-}term+linker}$-bZIP did

not compromise the co-localization with the nucleoid (**Figure 34**). Moreover, EMSAs with only $MinC^{linker+C\text{-}term}$ and MinD exhibited the highest DNA binding (**Figure 28**). Taken together, these data question the role of $MinC^{N\text{-}term}$ in the DNA binding. It is likely that this domain does not directly contact the DNA and that the negative aspartic acid simply repels the DNA in the EMSA assay. While reduced DNA binding was observed with $MinC^{K66A}$ and $MinC^{1\text{-}20\Delta}$ in EMSAs, it cannot be excluded that these modifications bring about some unforeseen conformational change to the MinC structure, as evident from the CD spectroscopy analysis of $MinC^{1\text{-}20\Delta}$ (**Figure 19** and **Figure 20**), which might have hindered the DNA binding by the MinC linker and $MinC^{C\text{-}term}$ domain/MinD. Further, from the competition experiments with FtsZ, I assumed that both the FtsZ and DNA binding interfaces overlap on MinC (**Figure 29**). Maybe, they do not have to overlap as I assumed. It is known that FtsZ interacts with $MinC^{N\text{-}term}$, $MinC^{C\text{-}term}$ and MinD in the MinCD complex (21,22,93). FtsZ, by binding to these regions, can bring a conformational change in the MinC linker not ideal for DNA binding. Taking this information all together, I believe that MinC linker is responsible for the DNA binding, provided it can dimerize, which is achieved by MinD and MinC. The N-terminal domain of MinC may be entirely dispensable for the binding, however further experiments are needed to clarify this point.

Substitution of G10 with proline showed significant perturbances in the secondary structural elements in CD spectroscopy (**Figures 19** and **20**), but no effect on DNA binding (**Figure 16**). MinC N-terminal domain dimerizes (18,23) and the crystal structure has shown that this dimerization happens *via* domain swapping of a β-sheet that includes the G10 residue (23). However, I found that, even after disruption of this β-sheet (with the introduction of G10P mutation), the mutant protein dimerized (**Figure 21**). Furthermore, with the removal of the whole β-sheet (1-20Δ), surprisingly, the mutant protein is able to form even higher-order structures in size-exclusion chromatography (**Figure 21**). These observations suggest that the MinC N-terminal domain has more than one dimerization interface.

3.1.4. MinC unstructured linker region and its importance in DNA binding

To the best of my knowledge, no previous study exists showing the importance of the linker region in *Ec*MinC in the function of the protein. The proline-rich disordered linker region connects *Ec*MinC N- and C- terminal domains (**Figure 22**), and a complete structure of *Ec*MinC is not yet available (23,24). For the past two decades, intrinsically disordered regions and proteins have been gaining popularity for their roles in cell signaling, receptor recognition,

enzyme catalysis, diseases, etc. (94,95). One of the best-known examples for the role of intrinsically disordered regions is the lac repressor. The lac repressor is a relatively big protein (347 amino acids) consisting of a DNA recognition domain, a core domain and a 4-helix bundle domain (96,97). The DNA recognition and core domains are connected by an intrinsically disordered linker consisting of 13 amino acids (96,97). This linker region gets structured upon binding to the lac operator sequence and is known to play a vital role in not only bringing together dimers of the DNA recognition domain, but also in increasing the binding affinity and sequence-specific recognition of the lac operator (98). In my thesis, I have shown that not only the sequence composition, but also the length of the *Ec*MinC linker is important for the DNA binding activity of the MinCD complex. Similarly to the lac repressor protein, the disordered linker in *Ec*MinC might aid in increasing the DNA binding affinity, in bending the DNA to accommodate the MinCD complex or in the recognition of specific DNA sequence or in all of these processes.

It is quite interesting to see in the EMSA experiments that just by introducing the MinC linker sequence to the maltose-binding protein (MBP) fused to a bZIP dimerization domain, a weak DNA binding can be observed (**Figure 28**). This binding was neither enhanced nor reduced by MinD, suggesting an inherent DNA binding activity by the MinC linker sequence alone.

3.1.5. Role of MinC linker in MinC-FtsZ interaction

Two hotspots on *Ec*MinC have been identified that interact with FtsZ (22). Additionally, MinD has also been shown to interact with the H10 helix of FtsZ directly, and by doing so, it positions MinC and FtsZ in such a way that MinC-FtsZ interaction is stronger (93). From the cell viability spot assays, I could see that in the presence of MinD, the MinC linker length plays a significant role in the interaction with FtsZ (**Figure 32**). If the linker is reduced to two or fewer residues, MinC is unable to inhibit FtsZ polymerization (**Figure 32**). Moreover, the linker sequence composition also plays a moderate role in FtsZ inhibition (**Figure 32**). Taken together, these results suggest that the MinC N- and C-terminal domains have to be oriented in a specific way and/or both domains should be highly flexible in order to efficiently inhibit FtsZ polymerization. Although in the cytoplasmic form of MinC the linker region does not seem to play a major role, its relevance becomes more evident when MinC is recruited to the cell membrane by MinD (**Figure 31** and **Figure 32**). This further supports my

notion mentioned under **Section 3.1.3.**, that binding of FtsZ to MinC and MinD brings a conformational change in MinC linker.

In the EMSA competition experiments with FtsZ, I observed that 10 μM FtsZ could inhibit DNA binding by MinCD (**Figure 29**). In an earlier study, however, in the liposome co-sedimentation experiments,10 μM FtsZ only weakly inhibited MinCD binding to the DNA, and a higher FtsZ concentration (30 μM) was needed to completely inhibit the DNA binding by MinCD (1). This could be due to the fact that, in the EMSA experiments, I used a short DNA fragment (52 bp) and not an entire plasmid as in the liposome co-sedimentation assay. In this case, FtsZ could have easier access to MinC and compete with DNA in binding to it.

*3.1.6. Co-localization of MinC$^{N\text{-}term+linker}$-bZIP-mRuby3 in the E. coli MG1655 Δ*minB* and *hu-gfp strains*

I observed co-localization of MinC$^{N\text{-}term+linker}$-bZIP-mRuby3 with the nucleoid in the Δ*minB* and *hu-gfp* strains (**Figure 35**). In the *hu-gfp* strain (81), however, the fusion protein was expressed at very low levels compared to those reached in the Δ*minB* strain, despite using the same IPTG concentration and incubation time for the induction. This could be due to the fact that the cells express two different fluorescent proteins at the same time, which are exogenous to *E. coli*, creating a heavy metabolic burden.

Overexpression of MBP-bZIP-mRuby3 in the *hu-gfp E. coli* strain resulted in cells with an abnormal cell length and defects were also observed in chromosome segregation (**Figure 35**). This suggests that bZIP from *S. cerevisiae* does something in the *E. coli* cells. It should be noted that the whole point of this study is to see only the co-localization of MinC with the bacterial nucleoid and that MBP-bZIP was only used as the negative control for the co-localization. How MBP-bZIP affects *E. coli* cells still remains an open question that is currently beyond the scope of my thesis.

Overexpression of MinC$^{N\text{-}term}$-bZIP in the Δ*minB E. coli* strain leads to a lethal filamentation phenotype (**Figure 33**), while expressing the same construct in the *hu-gfp E. coli* strain results in elongated cells, which are however not as long as those observed for the Δ*minB* strain (**Figure 35**). I speculate that, within the WT protein, the linker covers the region on the MinC N-terminal domain needed for inhibiting FtsZ polymerization (a negative regulator); probably two states exists, ‘covered’ and ‘uncovered’, and the equilibrium is shifted towards the ‘covered’ state for cytoplasmic MinC, thereby FtsZ inhibition is rather weak. MinC$^{N\text{-}term}$-

bZIP would be able to inhibit FtsZ since it lacks the linker and would be shifted towards the 'uncovered' state. In the *hu-gfp* strain, endogenous WT MinC could bind to $MinC^{N\text{-}term}$-bZIP, thereby attenuating inhibition of FtsZ. Binding between $MinC^{N\text{-}term}$-bZIP and WT MinC should be verified by performing pull-down and liposome-MinD co-sedimentation assays.

3.1.7. Min system and chromosome segregation - what did we learn from my Ph.D. studies

By performing computational analysis, Di Ventura *et al*. have predicted that for complete and stable chromosome segregation to happen in *E. coli*, the duplicated chromosomes have to be transiently tethered to the membrane creating a Brownian ratchet-type of motion (51). Further, they have proposed that MinD is responsible for this tethering and have shown for the first time *in vitro* and *in vivo* that MinD binds to DNA (51). While the study also tried to pinpoint the residues in MinD involved in the DNA binding, the identified residues were in close proximity to the cell membrane (51). Since both the cell membrane and the DNA are negatively charged, it was hypothesized that the identified residues near the C-terminal end might rather play an indirect role in DNA binding. With these data, it was hypothesized that N-terminal residues of MinD should be involved in the direct DNA binding.

Dr. Linda Klauss created a library of single and double mutants of MinD by systematically mutating positively charged residues with negative ones in the N-terminal region of MinD (1). By using this library, she identified several residues of MinD that are involved in DNA binding, albeit she could not clarify if the role of these residues was direct or indirect (1). Especially, she identified a double mutant (R99E/K110E) for which DNA binding was impaired *in vitro,* while membrane binding and Min oscillations were not affected when the protein was expressed above a certain level (1). Using this mutant, she observed chromosome segregation defects in *E. coli* cells, albeit at very low significance for smaller cells, and a moderate statistical significance for longer cells (1). Further, by performing ChIP-Seq analysis, she found no sequence specificity for MinD (1). Finally, she observed that MinC enhances DNA binding by MinD (1).

During my Ph.D. thesis, I studied the involvement of MinC in DNA binding by MinD in detail. Using computational tools, G10 and K66 residues of MinC were predicted to be involved in DNA binding, which I verified by creating and purifying various mutants and testing them in EMSA experiments (**Figure 16**). Several lines of evidence suggested that the loss of DNA binding by the $MinC^{G10D}$ mutant is due to electrostatic repulsion of the negatively charged DNA by the negatively charged aspartic acid (**Figure 19** and **Figure 20**). Finally, I

have discovered that MinC linker region is critical to DNA binding, both in terms of sequence composition (**Figure 23** and **Figure 25**) and length (**Figure 24**). Somewhat puzzlingly, microscopy experiments with synthetic constructs revealed that the G10 position does not seem to play a role in *in vivo* DNA binding, as nucleoid co-localization was observed when $MinC^{N\text{-}term/G10D\text{-}linker}$-bZIP was expressed in *E. coli* cells (**Figure 34**). Further, EMSAs with $MinC^{linker+C\text{-}term}$ and MinD suggest that $MinC^{N\text{-}term}$ is dispensable for DNA binding (**Figure 28**). Additionally, MinC linker region was found to play a significant role in the inhibitory activity of MinC against FtsZ (**Figure 31** and **Figure 32**). This is the first time that the importance of this linker for MinC function is highligthed.

The data obtained from my Ph.D. studies strongly support the notion that MinC bind to DNA when in complex with MinD. The direct DNA binding surface might involve MinC linker, as long as it can dimerize and has a proper orientation/conformation. MinD aids in the dimerization and orientation of MinC linker through $MinC^{C\text{-}term}$, and by doing so, might also end up interacting with DNA, as supported by previous studies from our group. Future structural studies should clarify this issue. Despite obtaining a large amount of data, our original hypothesis, i.e. that the Min system supports chromosome segregation in *E. coli*, still remains to be elucidated. The difficulty in studying chromosome segregation comes from the fact that it is nearly impossible to identify a mutant of MinD and/or MinC which lost the DNA binding activity but retained all other functionalities needed for the proper positioning of the septum at mid-cell. Depending on the growth conditions, *E. coli* cells show at times good segregation of the genetic material even in the absence of the Min system. Therefore, we cannot exclude that the Min proteins do not participate in chromosome segregation as originally hypothesized, but rather in other processes such as compaction or proper positioning of the nucleoid in respect to the membrane.

Earlier studies performed by Nordström *et al*. and Di Ventura *et al*. have already shown chromosome segregation defects in an *E. coli* Δ*minB* strain (51,99,100), yet, some of the cells of this strain are still able to place the Z-ring near to the mid-cell and the chromosomes are evenly distributed between the two daughter cells. This suggests that other protein machineries might exist in *E. coli* that are involved in chromosome segregation. In *E. coli* cells, the deletion of FtsK, a translocase, has been shown to negatively affect chromosome segregation (101,102). FtsK by assembling at the septum, aids in the translocation of the replicated chromosome to the daughter cell, in order to prevent guillotining of the chromosome by the constricting septum (101–103). Using the *E. coli* Δ*minB* strain, another negative regulator of FtsZ polymerization,

namely SlmA (synthetic lethal without Min) was discovered (104). SlmA tightly associates with bacterial nucleoid and prevents the Z-ring placement wherever the nucleoid is present (104). These redundencies add another layer of complication to studying the effect of MinC and MinD on chromosome segregation *in vivo* in *E. coli* cells.

3.2. Aggregation tendency, loss of direct MinE membrane interaction, inability to dislodge MinC and reduced accessibility of R21 residue in MinE-eYFP

Using a combination of *in vitro, in vivo* and *in silico* methods, in the present study we showed that MinE-eYFP is functionally impaired compared to untagged MinE. I used *in vitro* assays to control the level of protein(s) under investigation thereby eliminating the possibility of concentration-dependent effects. Computational analysis of MinE-eYFP predicted that the accessibility of the N-terminal membrane-binding region and of arginine at position 21, which is needed to activate/enhance the ATPase activity of MinD (14), were reduced while MinD binding and dimerization interfaces remain unaffected (data generated by Dr. Mehmet Ali Öztürk). I validated these predictions using a variety of experimental procedures (**Figures 46, 47** and **48**).

3.2.1. Direct membrane interaction of MinE-eYFP

In the membrane binding assay, I found that direct membrane interaction of MinE is affected in MinE-eYFP (**Figure 47**). Although membrane-binding by MinE is not required for displacing MinD from the membrane in the liposome co-sedimentation assay (**Figure 48**), the membrane-binding function of MinE has been shown to be needed for the proper Min oscillations and functioning of the Min system (28,32). This could also be a reason for the lack of complementation of Δ*minB* phenotype *in vivo* (**Figure 38**).

3.2.2. Displacement of MinC and MinD from the membrane by MinE-eYFP

In the liposome co-sedimentation assay with MinC and MinD I observed that MinE-eYFP was unable to displace MinC from MinD as well as untagged MinE (**Figure 44**). It is known from previous studies that both MinC and MinE compete for the same binding region on MinD which is created upon MinD dimerization (11,12,105). Although it is known that ATP hydrolysis by MinD is not necessary in order for MinE to displace MinC from MinD, the mechanism behind this displacement is still unclear (35,36). One could speculate that MinE first interacts with MinC directly and displaces MinC from MinD by force of repulsion, or

MinE interacts with MinD and induces a conformational change on MinD, which consequently results in MinC falling off from MinD. Since the mechanism is not clear, we could not perform detailed computational analyses to understand why MinE-eYFP is unable to displace MinC from MinD.

3.2.3. Aggregation tendency of MinE-eYFP

During expression and purification of MinE-eYFP, I found that MinE-eYFP forms inclusion bodies inside *E. coli* cells at high expression levels (**Figure 40** and **Figure 41**). The aggregation tendency of MinE-eYFP was not likely due to eYFP as I used a monomeric variant of eYFP containing the A206K mutation (106,107). In fact, when I expressed eYFP alone under the same conditions, most of the protein still remained in the soluble fraction (**Figure 40**). I speculate that eYFP interacts with the N-terminal membrane-binding region of MinE thereby favoring MinE to 'open state' (26). In the open state, the loop region and the β1-sheet of MinE are exposed (26). These regions become the so-called 'contact helix' upon interaction with MinD (26). In an earlier study, the I25R mutation on MinE has been shown to lead to a protein constitutively attached to the cell membrane (32). Thus fusion to eYFP seems to be doing something similar to MinE as the I25R mutation, however, unlike for $MinE^{I25R}$, the MTS in MinE-eYFP is less available for membrane binding, being likely "sequestered" by eYFP. The open state of MinE-eYFP can bind to MinD, however when MinD levels are lower compared to those of MinE-eYFP, the loop region and the β1-sheet on MinE can form amyloid-like fibrils as reported by a previous study (82).

3.3. SiMPl plasmid toolbox outperforms conventional method in maintaining two plasmids

3.3.1. Splitting and reconstituting enzymes conferring resistance towards antibiotics using split inteins

With the emergence of antibiotic resistance in bacteria and increased usage of antibiotics in the biotechnology and veterinary fields, the need for new classes of antibiotics is higher than ever before. In the present study, I have developed a tool using which two plasmids can be stably maintained with a single antibiotic. Although the tool does not prevent the emergence of antibiotic resistance in bacteria nor help in the treatment of resistant bacteria *per se*, it can minimize the amounts/types of antibiotics used in industries involved in biotransformation and in research; thereby reducing the costs involved. Unlike other methods

based on functional reconstitution of enzymes by unassisted (108) or assisted (72) physical proximity of the two dysfunctional parts, our tool uses the gp41-1 natural split intein (109) to reconstitute a full-length enzyme, where the two fragments are linked by a proper peptide bond after splicing. For some proteins, functional reconstitution works only partially (110). Apart from protein activity, the half-life of a protein inside a cell is determined by the type of amino acids which are present as the first and the last residues in a protein (111). Using inteins, these issues can be overcome.

Splitting a functional protein into two or more dysfunctional parts can be done rationally or randomly. For splitting the CAT, TEM-1βL, HPT and PAT enzymes, I followed a semi-rational approach. I looked for surface-exposed and flexible residues in the protein for identifying potential split sites. While flexible linker regions tend to be less conserved in most cases, some flexible regions are important for the protein function, for instance in *Ec*MinC (112). To surmount this issue, the evolutionary conservation of residues was also taken into account in identifying potential split sites. For CAT, TEM-1βL, HPT and PAT, 2, 3, 2 and 4 potential split sites were predicted by our method, respectively. While for CAT both the predicted sites yielded bacterial transformants on agar plates containing chloramphenicol, only one of the predicted sites yielded bacterial transformants for the remaining studied enzymes, with the exception of TEM-1βL. This may be due to lack of stability of the split fragments in *E. coli* cells. Further refinement has to be done to our methodology in the future. In our split constructs, mutation(s) of key residues in gp41-1 needed for the splicing reaction to occur showed that a complete reconstitution was needed for CAT (only split-site E140:N141) and HPT (split-site E255:L256) enzymes. For APT (split-site E118:N119), TEM-1βL (split-site S104:P105), and CAT (split-site E97:Q98), on the other hand, mutation of the asparagine at the very C-terminus of the C-intein still supported bacterial growth. For PAT, intein function was found to be completely dispensable albeit both the N and the C-intein fragments were needed to bring the two PAT halves together.

4. Outlook

4.1. E. coli MinCD proteins and chromosome segregation

4.1.1. Physiological role of DNA binding by MinCD proteins

To answer some of the open questions that arose during my Ph.D. studies, I have already suggested a few necessary experiments to be done while discussing the results. Our main hypothesis that the MinCD proteins together aid in the chromosome segretation process remains to be proved in the *in vivo* context. I cannot exclude that the DNA binding is needed to help compact or position the nucleoid rather than for active chromosome segregation. Further *in vivo* experiments are needed to have this mechanistic understanding.

4.1.2. Elucidation of DNA binding interface

The direct DNA binding surface on MinC/MinD still remains to be identified. This could be achieved using NMR for instance or cryo-EM, albeit the resolution here may not be sufficient to fully identify the residues involved in the binding. X-ray crystallography would be the best method, however full-length MinD is not a well-behaved protein, reason why in all current structural studies the mutant $MinD^{D40A\Delta10}$ is employed, being this a soluble, well-behaved protein. I however fear that such mutant may not reflect the wild-type protein and would prefer a method that allows using full-length MinD.

4.2. Linker sequence composition and length in fusion proteins

Given the functional impairment of the MinE-eYFP fusion protein, a solution to visualize and study Min oscillations *in vivo* could be the use of a chromobody. Yet the chromobody itself might also interfere with some function of MinE. Therefore, I believe that a better way forward is to find an optimal linker that may alleviate the functional impairment of the MinE-eYFP fusion protein. The advantage of this approach is that it can be generalized and applied in the context of other fusion proteins, opening up the possibility to solve the issue of dysfunctional GFP fusions.

4.3. Expanding the SiMPl plasmid toolbox

I have created the SiMPl plasmid toolbox for use with commonly selected antibiotics namely kanamycin, chloramphenicol, ampicillin, hygromycin, and puromycin. Researchers from other scientific communities, though, use other antibiotics in their regular research. I would be happy to expand the SiMPl tool-kit to facilitate research in these areas, too.

5. Materials and Methods

5.1. Plasmid constructs and bacterial strains

For protein purification purposes, the pET28a vector backbone was used (https://www.addgene.org/vector-database/2565/). The desired gene was cloned into the pET28a vector using the *BamHI* and *HindIII* or *NotI* restriction sites. In a few cases, the desired gene was cloned into the pET28a vector between the aforementioned restriction sites by the Gibson Assembly method®. Isolated genome from *E. coli* MG1655 WT strain was used as a template for PCR amplification of desired genes. For all the PCR amplifications, high-fidelity Phusion polymerase was used. Desired mutation(s) was/were introduced using the site-directed mutagenesis kit (Agilent) as per the manufacturer's protocol. Plasmids were amplified by transforming them into chemically competent *E. coli* TOP10 cells (Invitrogen™) and were isolated from *E. coli* cells using QIAprep® Spin Miniprep Kit (Qiagen) as per the manufacturer's protocol. The constructs were validated by performing Sanger sequencing (GATC Biotech, Germany). For protein expression, *E. coli* Rosetta™(DE3)pLysS cells were used (Novagen).

For *in vivo* studies, the pBAD33 vector backbone (https://www.addgene.org/vector-database/1848/) was used. Desired gene(s) or operon was cloned into the pBAD33 vector using the *SacI* and *HindIII* restriction sites. Similar to the plasmid constructs for the protein purification purposes, in a few cases, gene(s) or operon was cloned into pBAD33 vector between the aforementioned restriction sites by the Gibson Assembly method®. By default, the pBAD33 vector lacks a ribosome binding site. The ribosome binding site of *Ec*MinC was included in all our pBAD33 constructs. Unless otherwise specified differently, *E. coli* MG1655 WT and/or *E. coli* MG1655 Δ*minB* strain was used for all our *in vivo* studies.

minE-eyfp gene was cloned into the pET28a vector *via* the Gibson Assembly® method (NEB). Briefly, the pET28a-MinE plasmid was linearized without the stop codon after MinE by PCR. *eyfp* gene was amplified using a primer pair containing overlapping sequences with MinE and pET28a backbone. Additionally, the forward primer of the *eyfp* gene contained a *BamHI* restriction site followed by 9 nucleotides coding for amino acids 'GGG'. The *eyfp* gene was amplified using pBDV-15 as the template (51). The PCR products were then assembled into the pET28a-MinE-eYFP plasmid by the Gibson Assembly® method. For constructing pET28a-eYFP plasmid, the *eyfp* gene was amplified with a primer pair containing 5' and 3' with *BamHI* and *HindIII* restriction sites, respectively. Further downstream steps were similar

to as described for the construction of pET28a-MinC, pET28a-MinD, and pET28a-MinE plasmids.

pET28a-Strep-MinD$^{D40A\Delta10}$ plasmid was made by first introducing D40A mutation into the pET28a-MinD plasmid using the QuikChange II site-directed mutagenesis kit (Agilent Technologies) as per the manufacturer's protocol. Using overlapping primers, with a forward primer additionally containing nucleotides for Strep-tag and a reverse primer designed to carry a stop codon omitting the nucleotides coding for the final 10 amino acids in MinD, *strep-minD$^{D40A\Delta10}$* PCR fragment was generated. Using the pET28a-empty vector, the backbone without the sequences between *NcoI* and *HindIII* restriction sites was amplified by PCR. The PCR products were then assembled by the Gibson Assembly® method to yield pET28a-Strep-MinD$^{D40A\Delta10}$ plasmid. Plasmids constructed during my Ph.D. period are given in **Section 6**.

5.2. Protein expression and purification

Overnight bacterial culture was diluted in a 1-liter fresh nutrient broth containing 50 μg/ml of kanamycin with a starting OD_{600} of 0.1. The culture was grown till OD_{600} of 0.5, after which, protein expression was induced with 1 mM IPTG. The protein expression was carried out for 3 hours at 37 ^{o}C with shaking at 180 r.p.m. The bacterial cells were pelletized by centrifugation at 5000 r.p.m. for 20 min at 4 ^{o}C. The cells were then re-suspended in 30 ml of lysis buffer (50 mM potassium phosphate pH 8.0, 300 mM NaCl and 10 mM imidazole pH 8.0), additionally containing 1 cOmplete™, EDTA-free protease inhibitor cocktail tablet, 0.2 mM ADP and 0.2 mM $MgCl_2$. The cells were lysed by ultrasonication, and the lysate was clarified by centrifugation at 20000 r.p.m. for 20 min at 4 ^{o}C. The supernatant was further filtered by passing through a 0.4 μm filter and fed to an NGC™ medium pressure chromatography system (Bio-Rad). The chromatography system was fitted with a Profinity™ IMAC resin Ni-charged 1 ml column and a Bio-Scale™ Mini Bio-Gel® P-6 desalting 10 ml cartridge. The bound proteins were washed with 10 ml of wash buffer (50 mM potassium phosphate pH 7.5, 300 mM NaCl, 20 mM imidazole pH 8.0 and 10 % glycerol) and eluted with 2 ml of elution buffer (50 mM potassium phosphate pH 7.5, 300 mM NaCl, 500 mM imidazole pH 8.0 and 10 % glycerol). The elution buffer was then exchanged with storage buffer (50 mM HEPES-KOH pH 7.25, 150 mM KCl, 10 % glycerol and 0.1 mM EDTA pH 8.0). The protein in the storage buffer was split into two aliquots. One aliquot was stored at -80 ^{o}C for later use. His-tag cleavage was performed for the other aliquot by incubating the proteins with thrombin agarose beads (Thrombin CleanCleave™ Kit from Sigma-Aldrich) for 3 hours at room

temperature in a rotating wheel. After the His-tag removal, the protein was stored at -80 ºC as 50 µl aliquots.

For purifying Strep-MinD$^{D40A\Delta10}$, Strep-Tactin® Superflow® cartridge (IBA life sciences) was used. Wash and elution buffers were changed as per the manufacturer's protocol. Other buffers used were identical to the ones as described above.

5.3. Electrophoretic mobility shift assay (EMSA)

*Ec*MinD with or without *Ec*MinC was incubated with 50 nM 5' hex-labelled (hexachloro-6-carboxy-fluoresceine) 52 bp DNA in a buffer containing 50 mM HEPES-KOH pH 7.25, 150 mM KCl, 10 % glycerol, 0.1 mM EDTA pH 8.0, 1 mM ATP (or ADP) and 5 mM $MgCl_2$ at room temperature (20-25 ºC) for 10 min. The reaction mixture was then loaded on a 6 % native-PAGE gel. The gel was run in 0.5x TBE buffer for 20 min at constant voltage (150 V). Finally, the gel image was obtained using an Amersham Typhoon Gel and Blot Imaging Systems (GE Healthcare).

5.4. Liposome co-sedimentation assay

*Ec*MinD (WT or mutant) with or without *Ec*MinC (WT or mutant), 2 µM each, and with varying concentration or without *Ec*MinE, was co-incubated with 0.5 mg/ml of liposomes in a buffer containing 50 mM HEPES-KOH pH 7.25, 150 mM KCl, 10 % glycerol, 0.1 mM EDTA pH 8.0, 1 mM ATP and 5 mM $MgCl_2$ at room temperature (20-25 ºC) for 15 min. The reaction mixture was centrifuged at 14000 r.p.m. for 20 min at room temperature and the supernatant and the pellet were collected separately. The samples were denatured by boiling at 95 ºC for 12 min in 1x Laemmli sample buffer and were loaded on a 12 % Mini-PROTEAN® TGX™ precast protein gel (Bio-Rad). The gel was run for 30 min with a constant voltage (200 V) in 1x TGS buffer and then stained using InstantBlue™ protein gel stain (Expedeon). The gel image was documented using a UVP UVsolo touch (Analytik Jena).

5.5. Cell viability spot assay

*Ec*MinC (WT or mutant) and *Ec*MinD were cloned into the pBAD33 vector between the *SacI* and *HindIII* restriction sites with their native ribosome binding sites, respectively. Spot assay was performed as described previously by Zhou and Lutkenhaus (80). In detail, the constructed plasmid was transformed into an *E. coli* MG1655 Δ*minB* strain. A colony was picked and suspended in a nutrient broth without any antibiotic. The cells were then serially

diluted and spotted on agar plates with different arabinose concentration. The plates were then incubated overnight at 37 ^{o}C and visualized for cell viability.

5.6. Fluorescence microscopy

Overnight grown bacterial culture was diluted in a fresh nutrient (or tryptone) broth with a starting OD_{600} of 0.1. The culture was grown till OD_{600} of 0.5, after which, protein expression was induced with 1 mM or 100 μM IPTG or different concentrations of L-(+)-arabinose. The protein expression was carried out for 3 hours at 37 ^{o}C with shaking at 180 r.p.m. The bacterial cells were embedded on a 0.5 % agar pad and imaged using a Zeiss Axio Observer wide-field microscope equipped with a cooled CCD-camera 'AxioCam MRm' and alpha-Plan-APOCHROMAT 100x objective. The microscopy filter sets were adjusted to DAPI (or one of the conventional fluorescent protein markers depending on the experiment) and bright-field or DIC.

5.7. Pull-down assay

His-tagged MinE or MinE-eYFP (5 μM) was incubated with Strep-$MinD^{D40A\Delta10}$ (3 μM) at room temperature (20 – 25 ^{o}C) in an assay buffer (50 mM HEPES-KOH pH 7.25, 150 mM KCl, 0.1 mM EDTA pH 8.0, 1 mM ATP or ADP, 5 mM $MgCl_2$ and 10 % glycerol), additionally containing Promega MagneHis™ beads (Promega) for 15 min. Bound proteins were eluted with an elution buffer (50 mM Tris-HCl pH 7.0 and 500 mM Imidazole pH 8.0). The remaining downstream steps were similar to those as described in the **Liposome co-sedimentation assay section**.

5.8. MinE membrane-binding assay

MinE's membrane-binding ability was studied using a protocol described previously (28). To elaborate, MinE or MinE-eYFP (6 μM) was incubated with 1 mg/ml of liposomes derived from *E. coli* lipids (a kind gift from Chris van der Does) in 90 μl of buffer containing 20 mM Tris-HCl pH 7.5 and 200 mM sucrose, at 30 ^{o}C for an hour. The samples were then centrifuged at 14000 rpm for 20 min at room temperature (20 – 25 ^{o}C) and the supernatant and the pellet were collected separately. The samples were then boiled in a tricine sample buffer (100 mM Tris-HCl pH 6.8, 20 % glycerol, 1 % SDS, 0.02 % Coomassie Blue G-250 and 1 % β-mercaptoethanol) for 5 min and ran on a 16.5 % tris-tricine precast protein gel (Bio-Rad). The gel was then stained using the InstantBlue™ protein stain (Expedeon Ltd) and documented using the UVP UVsolo touch (Analytik Jena, Germany).

5.9. Size-exclusion chromatography

Size-exclusion chromatography was performed using an AZURA® fast protein liquid chromatography device (KNAUER) fitted with a Superdex 200 column (GE). A sample volume of 500 µl was injected into the system. Bovine serum albumin (BSA: 15 µM) and carbonic anhydrase (CA: 33 µM) were used as reference samples for the molecular weight determination. MinE or MinE-eYFP was injected into the system with a concentration of 13 µM. The running buffer consisted of 50 mM HEPES-KOH pH 7.25, 150 mM KCl, 0.1 mM EDTA pH 8.0 and 10 % glycerol. The device was driven with a flow rate of 0.5 ml/min.

5.10. Construction of SiMPl plasmids

For the construction of the SiMPl plasmids, backbones of the pBAD33 and pTrc99a plasmids were chosen. Arabinose is used to induce the expression of the desired gene in the pBAD33 vector while isopropyl-β-D-thiogalactoside (IPTG), a non-metabolizing lactose analog, is used to induce the expression of the desired gene in the pTrc99a vector. **Figure 68** shows the plasmid maps of the aforementioned vectors. The pBAD33 vector carries chloramphenicol acetyltransferase (CAT) that confers resistance towards chloramphenicol while the pTrc99a vector carries TEM-1 β lactamase (TEM-1 βL) that confers resistance towards ampicillin.

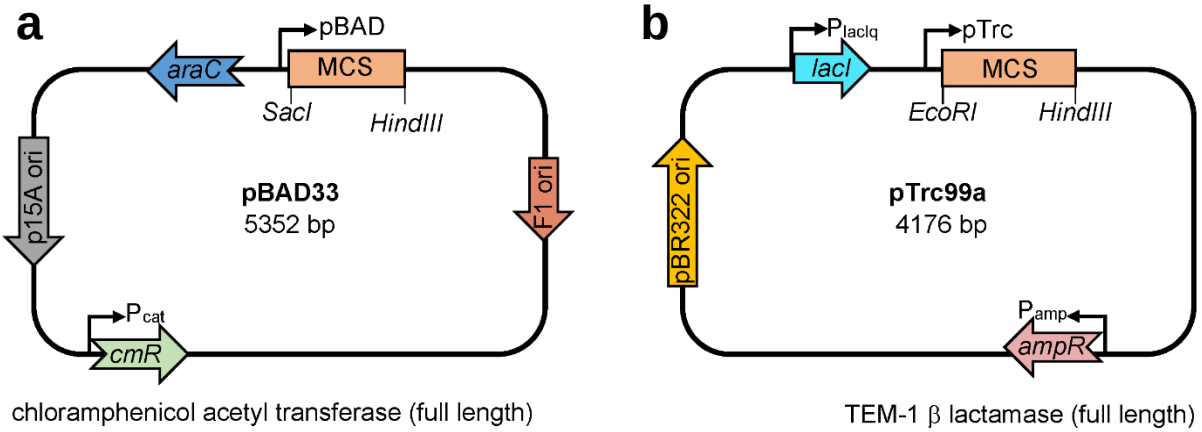

Figure 68. Plasmid maps showing important features of pBAD33 (**a**) and pTrc99a (**b**) empty plasmids. MCS = multiple cloning site. p15A origin of replication in pBAD33 belongs to incompatible group B while pBR322 origin of replication in pTrc99a belongs to incompatible group A.

Genes coding for *egfp* and *mruby3* were amplified by PCR and doubled digested with restriction enzymes *SacI* and *HindIII*, and *EcoRI* and *HindIII*, respectively. *egfp* was cloned into the MCS of the pBAD33 vector and *mruby3* was cloned into the MCS of the pTrc99a vector. To make these plasmids into a SiMPl plasmid-pair version, the pBAD33-eGFP

backbone was amplified *via* PCR without the chloramphenicol acetyltransferase gene and the pTrc99a-mRuby3 backbone was amplified *via* PCR without the TEM-1 β lactamase gene. Gene of respective enzymes conferring resistance towards particular antibiotics was PCR amplified into two halves independently and genes of gp41-1 N and C-inteins were also amplified independently. Finally, the respective PCR amplified DNA fragments and the vector backbones were added together and assembled into the final plasmids by the Gibson Assembly® method (NEB Inc., the USA). All the PCR amplifications were done using the 2x Phusion Flash High-Fidelity PCR Master Mix (Thermo Fisher Scientific, the US) as per the manufacturer's protocol.

5.11. Transformation and selection of E. coli cells containing SiMPl plasmids

For the selection and propagation of plasmids, chemically competent One Shot TOP10 *E. coli* cells were used (invitrogen™). For the selection of *E. coli* cells carrying the desired plasmids, antibiotics namely, kanamycin, ampicillin, chloramphenicol, and hygromycin were used with final concentrations 50, 100, 35 and 100 (μg/ml), respectively. For selecting *E. coli* cells carrying resistance gene for puromycin, the selection was performed on a pH adjusted nutrient agar or broth (50 mM Tris-HCl pH 8.0) with 50 μg/ml final concentration of puromycin.

5.12. Plasmid isolation and agarose gel electrophoresis

Plasmid DNA was isolated using the QIAprep® Spin Miniprep kit (QIAGEN, Germany) as per the manufacturer's protocol.

DNA (plasmid or PCR product) was visualized on a 1 % agarose gel. The agarose gel was run for 45 min at 100 V (constant) in 0.5x TAE buffer (20 mM Tris-acetate pH 8.5 and 0.5 mM EDTA pH8.0) and the gel was imaged using the UVP UVsolo touch (Analytik Jena AG, Germany).

5.13. Bacterial growth analysis

The bacterial growth curve was studied *via* two methods, one using the shaking incubator while the other one using a plate reader. When using the shaking incubator, 20 ml of fresh nutrient broth with the respective antibiotic, was inoculated with the overnight grown bacterial culture with a starting OD_{600} of 0.1 in a 50 ml Erlenmeyer flask. The culture was incubated at 37 ^{o}C and shaken at 220 r.p.m. OD_{600} measurements were taken using IMPLEN OD600 DiluPhotometer™ (IMPLEN GmbH, Germany) for every 30 minutes until the absorbance reaches 2.0.

For studying the bacterial growth curve using a plate reader, a previously published protocol was followed (113). Briefly, overnight bacterial culture was diluted to OD_{600} of 0.01 with a fresh nutrient broth containing the respective antibiotic. One hundred and twenty µl of this diluted culture was then pipetted into each well of a flat-bottom 96-well plate. The plate was then closed with a lid and the sides were sealed using a parafilm tape to avoid evaporation. Absorbance measurement was done using BioTek Synergy™ H4 plate reader. This plate reader was driven by Gen5 v2.01.14 software and had following settings; temperature = 37 ^{o}C, run time = 20 hours, read interval = 2 min and 43 sec, wavelength = 600 nm, shake = slow, shake once every 130 sec, read = absorbance endpoint, read speed = normal and delay = 100 msec. The plate reader was pre-heated to 37 ^{o}C before the start of the experiment. For each strain, growth analysis was done with biological duplicates and technical triplicates.

5.14. Protein Cα– fluctuation analysis

The flexibility of residues, in terms of alpha carbon (Cα) fluctuation, in a protein was studied using CABS-flex 2.0 webserver (http://biocomp.chem.uw.edu.pl/CABSflex2) with default parameters (89).

5.15. Image analysis

Protein gel images were analyzed and band intensities were quantified using Fiji (https://imagej.net/Fiji) (114). Similarly, Fiji was also used to visualize the miscroscopy images.

6. List of plasmids constructed

Plasmid name	Description
pNPY1	pET28a backbone with *minD* cloned between *BamHI* and *HindIII*
pNPY2	pET28a backbone with *minC* cloned between *BamHI* and *HindIII*
pNPY3	pET28a backbone with *minE* cloned between *BamHI* and *HindIII*
pNPY4	pET28a backbone with *ftsZ* cloned between *BamHI* and *HindIII*
pNPY5	pET28a backbone with *minC* (G10A mutant). Site-directed mutagenesis performed with pNPY2
pNPY6	pET28a backbone with *minC* (G10D mutant). Site-directed mutagenesis performed with pNPY2
pNPY7	pET28a backbone with *minC* (G10P mutant). Site-directed mutagenesis performed with pNPY2
pNPY8	pET28a backbone with *minC* (G10R mutant). Site-directed mutagenesis performed with pNPY2
pNPY9	pET28a backbone with *minC* (K66A mutant). Site-directed mutagenesis performed with pNPY2
pNPY10	pET28a backbone with *minC* (Δ1-20 mutant). Omitted the desired residues in the construct by linearization and self-circularization performed with pNPY2
pNPY11	pET28a backbone with *minC* (only N-terminal domain). Omitted the desired residues in the construct by linearization and self-circularization performed with pNPY2
pNPY12	pET28a backbone with *minC* (only C-terminal domain). Omitted the desired residues in the construct by linearization and self-circularization performed with pNPY2
pNPY13	pET28a backbone with *minC* (only N-terminal domain with G10D mutation). Site-directed mutagenesis performed with pNPY11
pNPY14	pET28a backbone with *minC* (only N-terminal domain with G10P mutation). Site-directed mutagenesis performed with pNPY11
pNPY15	pET28a backbone with *minC* (GS as linker residues instead of the native linker region residues). Omitted and added the desired residues in the construct by linearization and self-circularization performed with pNPY2

pNPY16	pET28a backbone with *minC* (AGGSG as linker residues instead of the native linker region residues). Omitted and added the desired residues in the construct by linearization and self-circularization performed with pNPY2
pNPY17	pET28a backbone with *minC* (AGGSGAGGSG as linker residues instead of the native linker region residues). Omitted and added the desired residues in the construct by linearization and self-circularization performed with pNPY2
pNPY18	pET28a backbone with *minC* (AGGSGAGGSGAGGSG as linker residues instead of the native linker region residues). Omitted and added the desired residues in the construct by linearization and self-circularization performed with pNPY2
pNPY19	pET28a backbone with *minC* (AGGSGAGGSGAGGSGAGGSG as linker residues instead of the native linker region residues). Omitted and added the desired residues in the construct by linearization and self-circularization performed with pNPY2
pNPY20	pET28a backbone with *minC* (AGGSGAGGSGAGGSGAGGS as linker residues instead of the native linker region residues). Omitted and added the desired residues in the construct by linearization and self-circularization performed with pNPY2
pNPY21	pET28a backbone with *minC* (Δ102-105 mutant). Omitted the desired residues in the construct by linearization and self-circularization performed with pNPY2
pNPY22	pET28a backbone with *minC* (Δ102-109 mutant). Omitted the desired residues in the construct by linearization and self-circularization performed with pNPY2
pNPY23	pET28a backbone with *minC* (Δ102-114 mutant). Omitted the desired residues in the construct by linearization and self-circularization performed with pNPY2
pNPY24	pET28a backbone with *minC* (R133A mutant). Site-directed mutagenesis performed with pNPY2

pNPY25	pET28a backbone with *minC* (only N-terminal domain with native linker). Omitted the desired residues in the construct by linearization and self-circularization performed with pNPY2
pNPY26	pET28a backbone with *minC* (only native linker with C-terminal domain). Omitted the desired residues in the construct by linearization and self-circularization performed with pNPY2
pNPY27	pET28a backbone with *minC* (only N-terminal domain with native linker and GCN4 leucine zipper). Omitted and added the desired residues in the construct by linearization and self-circularization performed with pNPY2
pNPY28	pET28a backbone with maltose binding protein
pNPY29	pET28a backbone with maltose binding protein and GCN4 leucine zipper. Added the desired residues in the construct by linearization and self-circularization performed with pNPY28
pNPY30	pET28a backbone with maltose binding protein, MinC linker region sequence and GCN4 leucine zipper. Added the desired residues in the construct by linearization and self-circularization performed with pNPY28
pNPY31	pBAD33 backbone with *minC* and *minD* cloned between *SacI* and *HindIII* restriction sites with their native ribosome binding sites.
pNPY32	pBAD33 backbone with *minC* (G10A mutant) and *minD* cloned between *SacI* and *HindIII* restriction sites with their native ribosome binding sites. Site-directed mutagenesis performed with pNPY31
pNPY33	pBAD33 backbone with *minC* (G10D mutant) and *minD* cloned between *SacI* and *HindIII* restriction sites with their native ribosome binding sites. Site-directed mutagenesis performed with pNPY31
pNPY34	pBAD33 backbone with *minC* (G10P mutant) and *minD* cloned between *SacI* and *HindIII* restriction sites with their native ribosome binding sites. Site-directed mutagenesis performed with pNPY31
pNPY35	pBAD33 backbone with *minC* (G10R mutant) and *minD* cloned between *SacI* and *HindIII* restriction sites with their native ribosome binding sites. Site-directed mutagenesis performed with pNPY31
pNPY36	pBAD33 backbone with *minC* (GS as linker residues instead of the native linker region residues) and *minD* cloned between *SacI* and *HindIII*

	restriction sites with their native ribosome binding sites. Omitted and added the desired residues in the construct by linearization and self-circularization performed with pNPY31
pNPY37	pBAD33 backbone with *minC* (AGGSG as linker residues instead of the native linker region residues) and *minD* cloned between *SacI* and *HindIII* restriction sites with their native ribosome binding sites. Omitted and added the desired residues in the construct by linearization and self-circularization performed with pNPY31
pNPY38	pBAD33 backbone with *minC* (AGGSGAGGSG as linker residues instead of the native linker region residues) and *minD* cloned between *SacI* and *HindIII* restriction sites with their native ribosome binding sites. Omitted and added the desired residues in the construct by linearization and self-circularization performed with pNPY31
pNPY39	pBAD33 backbone with *minC* (AGGSGAGGSGAGGSG as linker residues instead of the native linker region residues) and *minD* cloned between *SacI* and *HindIII* restriction sites with their native ribosome binding sites. Omitted and added the desired residues in the construct by linearization and self-circularization performed with pNPY31
pNPY40	pBAD33 backbone with *minC* (AGGSGAGGSGAGGSGAGGSG as linker residues instead of the native linker region residues) and *minD* cloned between *SacI* and *HindIII* restriction sites with their native ribosome binding sites. Omitted and added the desired residues in the construct by linearization and self-circularization performed with pNPY31
pNPY41	pBAD33 backbone with *minC* (Δ102-105 mutant) and *minD*. Omitted the desired residues in the construct by linearization and self-circularization performed with pNPY31
pNPY42	pBAD33 backbone with *minC* (Δ102-109 mutant) and *minD*. Omitted the desired residues in the construct by linearization and self-circularization performed with pNPY31
pNPY43	pBAD33 backbone with *minC* (Δ102-114 mutant) and *minD*. Omitted the desired residues in the construct by linearization and self-circularization performed with pNPY31

pNPY44	pTrc99a backbone with *minC* (only N-terminal domain with native linker and GCN4 leucine zipper) followed by *mruby3* cloned between *EcoRI* and *HindIII*
pNPY45	pTrc99a backbone with *minC* (only N-terminal domain and GCN4 leucine zipper) followed by *mruby3* cloned between *EcoRI* and *HindIII*
pNPY46	pTrc99a backbone with *mbp* followed by *mruby3* cloned between *EcoRI* and *HindIII*
pNPY47	pTrc99a backbone with *minC* (only N-terminal domain with native linker and GCN4 leucine zipper) followed by *mruby3* cloned between *EcoRI* and *HindIII*. It has a G10D mutation. Site-directed mutagenesis performed with pNPY44
pNPY48	Same as pNPY44. *ampR* was replaced with *kanR*
pNPY49	Same as pNPY45. *ampR* was replaced with *kanR*
pNPY50	Same as pNPY46. *ampR* was replaced with *kanR*
pNPY51	pBAD33 backbone with *minB* operon cloned between *EcoRI* and *HindIII*
pNPY52	pBAD33 backbone with *minB* operon cloned between *EcoRI* and *HindIII.* The stop codon after minE was removed and added 'GSGGG' residues followed by *eyfp* gene
pNPY53	pET28a backbone with *eyfp* cloned between *EcoRI* and *HindIII*. N-terminal of *eyfp* gene additionally has 'GSGGG' residues
pNPY54	pET28a backbone with *minE*-GSGGG-*eyfp* cloned between *EcoRI* and *HindIII*
pNPY55	pET28a backbone with $minD^{D40A\Delta 10}$ gene cloned between *NcoI* and *HindIII*. His-tag was replaced with a strep-tag
pNPY55	pET28a backbone with *minE* (13-88) mutant. Omitted the desired residues in the construct by linearization and self-circularization performed with pNPY3
pNPY56	pBAD33 backbone with *egfp* gene cloned between *SacI* and *HindIII.*
pNPY57	pTrc99a backbone with *mruby3* gene cloned between *EcoRI* and *HindIII*
pNPY58	pNPY56 with *cmR* replaced with one half of *kanR* and *gp41-1 N-intein*. Also known as $SiMPl^k$_N
pNPY59	pNPY57 with *ampR* replaced with *gp41-1 C-intein* and another half of *kanR*. Also known as $SiMPl^k$_C

pNPY60	pNPY56 with *cmR* replaced with one half of *cmR* and *gp41-1 N-intein*. Also known as SiMPl^{c}_N. Split 97
pNPY61	pNPY57 with *ampR* replaced with *gp41-1 C-intein* and another half of *cmR*. Also known as SiMPl^{c}_C. Split 97
pNPY62	pNPY56 with *cmR* replaced with one half of *cmR* and *gp41-1 N-intein*. Also known as SiMPl^{c}_N. Split 140
pNPY63	pNPY57 with *ampR* replaced with *gp41-1 C-intein* and another half of *cmR*. Also known as SiMPl^{c}_C. Split 140
pNPY64	pNPY56 with *cmR* replaced with one half of *ampR* and *gp41-1 N-intein*. Also known as SiMPl^{a}_N. Split 104
pNPY65	pNPY57 with *ampR* replaced with *gp41-1 C-intein* and another half of *ampR*. Also known as SiMPl^{a}_C. Split 104
pNPY66	pNPY56 with *cmR* replaced with one half of *ampR* and *gp41-1 N-intein*. Split 213
pNPY67	pNPY56 with *cmR* replaced with one half of *hygR* and *gp41-1 N-intein*. Also known as SiMPl^{h}_N
pNPY68	pNPY57 with *ampR* replaced with *gp41-1 C-intein* and another half of *hygR*. Also known as SiMPl^{h}_C
pNPY69	pNPY56 with *cmR* replaced with one half of *purR* and *gp41-1 N-intein*. Also known as SiMPl^{p}_N
pNPY70	pNPY57 with *ampR* replaced with *gp41-1 C-intein* and another half of *purR*. Also known as SiMPl^{p}_C

7. References

1. Klauss LE. Molecular mechanism of chromosome segregation by the *E. coli* Min system [Internet]. Heidelberg: Dissertation, Ruperto-Carola University of Heidelberg, 2017; 2018 [cited 2020 Feb 25]. 1 Online-Ressource (110 Seiten). Available from: http://nbn-resolving.de/urn:nbn:de:bsz:16-heidok-232299.

2. Wang JD, Levin PA. Metabolism, cell growth and the bacterial cell cycle. Nat Rev Microbiol. 2009 Nov;7(11):822–7.

3. Toro E, Hong S-H, McAdams HH, Shapiro L. *Caulobacter* requires a dedicated mechanism to initiate chromosome segregation. Proc Natl Acad Sci. 2008 Oct 7;105(40):15435–40.

4. Wu LJ, Errington J. Nucleoid occlusion and bacterial cell division. Nat Rev Microbiol. 2012 Jan;10(1):8–12.

5. Rowlett VW, Margolin W. The Min system and other nucleoid-independent regulators of Z ring positioning. Front Microbiol [Internet]. 2015 [cited 2020 Feb 25];6. Available from: https://www.frontiersin.org/articles/10.3389/fmicb.2015.00478/full.

6. Böhm K, Meyer F, Rhomberg A, Kalinowski J, Donovan C, Bramkamp M. Novel Chromosome Organization Pattern in *Actinomycetales*—Overlapping Replication Cycles Combined with Diploidy. mBio [Internet]. 2017 Jul 5 [cited 2020 Feb 25];8(3). Available from: https://mbio.asm.org/content/8/3/e00511-17.

7. Boer PA de, Crossley RE, Rothfield LI. Isolation and properties of *minB*, a complex genetic locus involved in correct placement of the division site in *Escherichia coli*. J Bacteriol. 1988 May 1;170(5):2106–12.

8. Boer PAJ de, Crossley RE, Rothfield LI. A division inhibitor and a topological specificity factor coded for by the minicell locus determine proper placement of the division septum in *E. coli*. Cell. 1989 Feb 24;56(4):641–9.

9. Raskin DM, de Boer PAJ. Rapid pole-to-pole oscillation of a protein required for directing division to the middle of *Escherichia coli*. Proc Natl Acad Sci U S A. 1999 Apr 27;96(9):4971–6.

10. Lutkenhaus J, Sundaramoorthy M. MinD and role of the deviant Walker A motif, dimerization and membrane binding in oscillation. Mol Microbiol. 2003 Apr;48(2):295–303.

11. Zhou H, Schulze R, Cox S, Saez C, Hu Z, Lutkenhaus J. Analysis of MinD Mutations Reveals Residues Required for MinE Stimulation of the MinD ATPase and Residues Required for MinC Interaction. J Bacteriol. 2005 Jan 15;187(2):629–38.

12. Wu W, Park K-T, Holyoak T, Lutkenhaus J. Determination of the structure of the MinD-ATP complex reveals the orientation of MinD on the membrane and the relative location of the binding sites for MinE and MinC. Mol Microbiol. 2011 Mar;79(6):1515–28.

13. Hayashi I, Oyama T, Morikawa K. Structural and functional studies of MinD ATPase: implications for the molecular recognition of the bacterial cell division apparatus. EMBO J. 2001 Apr 17;20(8):1819–28.

14. Park K-T, Wu W, Lovell S, Lutkenhaus J. Mechanism of the asymmetric activation of the MinD ATPase by MinE. Mol Microbiol. 2012 Jul;85(2):271–81.

15. Hu Z, Lutkenhaus J. A conserved sequence at the C-terminus of MinD is required for binding to the membrane and targeting MinC to the septum. Mol Microbiol. 2003 Jan;47(2):345–55.

16. Szeto TH, Rowland SL, Habrukowich CL, King GF. The MinD membrane targeting sequence is a transplantable lipid-binding helix. J Biol Chem. 2003 Oct 10;278(41):40050–6.

17. Szeto TH, Rowland SL, King GF. The Dimerization Function of MinC Resides in a Structurally Autonomous C-Terminal Domain. J Bacteriol. 2001 Nov 15;183(22):6684–7.

18. Hu Z, Lutkenhaus J. Analysis of MinC Reveals Two Independent Domains Involved in Interaction with MinD and FtsZ. J Bacteriol. 2000 Jul 15;182(14):3965–71.

19. Dajkovic A, Lan G, Sun SX, Wirtz D, Lutkenhaus J. MinC Spatially Controls Bacterial Cytokinesis by Antagonizing the Scaffolding Function of FtsZ. Curr Biol. 2008 Feb 26;18(4):235–44.

20. Hu Z, Mukherjee A, Pichoff S, Lutkenhaus J. The MinC component of the division site selection system in *Escherichia coli* interacts with FtsZ to prevent polymerization. Proc Natl Acad Sci. 1999 Dec 21;96(26):14819–24.

21. Park K-T, Dajkovic A, Wissel M, Du S, Lutkenhaus J. MinC and FtsZ mutant analysis provides insight into MinC/MinD-mediated Z ring disassembly. J Biol Chem. 2018 Apr 20;293(16):5834–46.

22. LaBreck CJ, Conti J, Viola MG, Camberg JL. MinC N- and C-Domain Interactions Modulate FtsZ Assembly, Division Site Selection, and MinD-Dependent Oscillation in *Escherichia coli*. J Bacteriol [Internet]. 2019 Feb 15 [cited 2020 Jan 7];201(4). Available from: https://jb.asm.org/content/201/4/e00374-18.

23. An JY, Kim TG, Park KR, Lee JG, Youn HS, Lee Y, *et al*. Crystal structure of the N-terminal domain of MinC dimerized via domain swapping. J Synchrotron Radiat. 2013 Nov;20(Pt 6):984–8.

24. Yang S, Shen Q, Wang S, Song C, Lei Z, Han S, *et al*. Characterization of C-terminal structure of MinC and its implication in evolution of bacterial cell division. Sci Rep. 2017 Aug 8;7(1):1–10.

25. Zhou H, Lutkenhaus J. The Switch I and II Regions of MinD Are Required for Binding and Activating MinC. J Bacteriol. 2004 Mar 1;186(5):1546–55.

26. Park K-T, Villar MT, Artigues A, Lutkenhaus J. MinE conformational dynamics regulate membrane binding, MinD interaction, and Min oscillation. Proc Natl Acad Sci U S A. 2017 18;114(29):7497–504.

27. Hu Z, Lutkenhaus J. Topological regulation of cell division in *E. coli*. spatiotemporal oscillation of MinD requires stimulation of its ATPase by MinE and phospholipid. Mol Cell. 2001 Jun;7(6):1337–43.

28. Hsieh C-W, Lin T-Y, Lai H-M, Lin C-C, Hsieh T-S, Shih Y-L. Direct MinE-membrane interaction contributes to the proper localization of MinDE in *E. coli*. Mol Microbiol. 2010 Jan;75(2):499–512.

29. Zhao CR, Boer PA de, Rothfield LI. Proper placement of the *Escherichia coli* division site requires two functions that are associated with different domains of the MinE protein. Proc Natl Acad Sci. 1995 May 9;92(10):4313–7.

30. Pichoff S, Vollrath B, Touriol C, Bouché JP. Deletion analysis of gene *minE* which encodes the topological specificity factor of cell division in *Escherichia coli*. Mol Microbiol. 1995 Oct;18(2):321–9.

31. King GF, Rowland SL, Pan B, Mackay JP, Mullen GP, Rothfield LI. The dimerization and topological specificity functions of MinE reside in a structurally autonomous C-terminal domain. Mol Microbiol. 1999;31(4):1161–9.

32. Park K-T, Wu W, Battaile KP, Lovell S, Holyoak T, Lutkenhaus J. The Min oscillator uses MinD-dependent conformational changes in MinE to spatially regulate cytokinesis. Cell. 2011 Aug 5;146(3):396–407.

33. Membrane Binding of MinE Allows for a Comprehensive Description of Min-Protein Pattern Formation [Internet]. [cited 2020 Jan 31]. Available from: https://journals.plos.org/ploscompbiol/article?id=10.1371/journal.pcbi.1003347.

34. Hu Z, Gogol EP, Lutkenhaus J. Dynamic Assembly of MinD on Phospholipid Vesicles Regulated by ATP and MinE. Proc Natl Acad Sci U S A. 2002;99(10):6761–6.

35. Lackner LL, Raskin DM, de Boer PAJ. ATP-dependent interactions between *Escherichia coli* Min proteins and the phospholipid membrane in vitro. J Bacteriol. 2003 Feb;185(3):735–49.

36. Hu Z, Saez C, Lutkenhaus J. Recruitment of MinC, an Inhibitor of Z-Ring Formation, to the Membrane in *Escherichia coli*: Role of MinD and MinE. J Bacteriol. 2003 Jan;185(1):196–203.

37. Hale CA, Meinhardt H, de Boer PAJ. Dynamic localization cycle of the cell division regulator MinE in *Escherichia coli.* EMBO J. 2001 Apr 2;20(7):1563–72.

38. Arjunan SNV, Tomita M. A new multicompartmental reaction-diffusion modeling method links transient membrane attachment of *E. coli* MinE to E-ring formation. Syst Synth Biol. 2010 Mar 1;4(1):35–53.

39. Fu X, Shih YL, Zhang Y, Rothfield LI. The MinE ring required for proper placement of the division site is a mobile structure that changes its cellular location during the *Escherichia coli* division cycle. Proc Natl Acad Sci U S A. 2001 Jan 30;98(3):980–5.

40. Ivanov V, Mizuuchi K. Multiple modes of interconverting dynamic pattern formation by bacterial cell division proteins. Proc Natl Acad Sci U S A. 2010 May 4;107(18):8071–8.

41. Loose M, Fischer-Friedrich E, Ries J, Kruse K, Schwille P. Spatial Regulators for Bacterial Cell Division Self-Organize into Surface Waves *In Vitro*. Science. 2008 May 9;320(5877):789–92.

42. Lutkenhaus J, Pichoff S, Du S. Bacterial cytokinesis: From Z ring to divisome. Cytoskeleton. 2012;69(10):778–90.

43. Marston AL, Thomaides HB, Edwards DH, Sharpe ME, Errington J. Polar localization of the MinD protein of *Bacillus subtilis* and its role in selection of the mid-cell division site. Genes Dev. 1998 Nov 1;12(21):3419–30.

44. Pavlendová N, Muchová K, Barák I. Expression of *Escherichia coli* Min system in *Bacillus subtilis* and its effect on cell division. FEMS Microbiol Lett. 2010 Jan 1;302(1):58–68.

45. Jamroškovič J, Pavlendová N, Muchová K, Wilkinson AJ, Barák I. An oscillating Min system in *Bacillus subtilis* influences asymmetrical septation during sporulation. Microbiology,. 2012;158(8):1972–81.

46. Ramirez-Arcos S, Szeto J, Dillon J-AR, Margolin W. Conservation of dynamic localization among MinD and MinE orthologues: oscillation of *Neisseria gonorrhoeae* proteins in *Escherichia coli*. Mol Microbiol. 2002;46(2):493–504.

47. Palanisamy N, Öztürk MA, Ventura BD. C-terminal eYFP fusion impairs *Escherichia coli* MinE function. bioRxiv. 2020 Jan 10;2020.01.08.899393.

48. Yanagida M. Basic mechanism of eukaryotic chromosome segregation. Philos Trans R Soc B Biol Sci. 2005 Mar 29;360(1455):609–21.

49. Jun S, Mulder B. Entropy-driven spatial organization of highly confined polymers: Lessons for the bacterial chromosome. Proc Natl Acad Sci. 2006 Aug 15;103(33):12388–93.

50. Jun S, Wright A. Entropy as the driver of chromosome segregation. Nat Rev Microbiol. 2010 Aug;8(8):600–7.

51. Di Ventura B, Knecht B, Andreas H, Godinez WJ, Fritsche M, Rohr K, *et al.* Chromosome segregation by the *Escherichia coli* Min system. Mol Syst Biol. 2013;9:686.

52. Hester CM, Lutkenhaus J. Soj (ParA) DNA binding is mediated by conserved arginines and is essential for plasmid segregation. Proc Natl Acad Sci. 2007 Dec 18;104(51):20326–31.

53. Chalfie M, Tu Y, Euskirchen G, Ward WW, Prasher DC. Green fluorescent protein as a marker for gene expression. Science. 1994 Feb 11;263(5148):802–5.

54. Shaner NC, Campbell RE, Steinbach PA, Giepmans BNG, Palmer AE, Tsien RY. Improved monomeric red, orange and yellow fluorescent proteins derived from *Discosoma sp.* red fluorescent protein. Nat Biotechnol. 2004 Dec;22(12):1567–72.

55. Wang L, Jackson WC, Steinbach PA, Tsien RY. Evolution of new nonantibody proteins via iterative somatic hypermutation. Proc Natl Acad Sci. 2004 Nov 30;101(48):16745–9.

56. Walter N, Holweg CL. Head-neck domain of *Arabidopsis* myosin XI, MYA2, fused with GFP produces F-actin patterns that coincide with fast organelle streaming in different plant cells. BMC Plant Biol. 2008 Jul 3;8:74.

57. Kraft C, Deplazes A, Sohrmann M, Peter M. Mature ribosomes are selectively degraded upon starvation by an autophagy pathway requiring the Ubp3p/Bre5p ubiquitin protease. Nat Cell Biol. 2008 May;10(5):602–10.

58. Raskin DM, de Boer PA. The MinE ring: an FtsZ-independent cell structure required for selection of the correct division site in *E. coli.* Cell. 1997 Nov 28;91(5):685–94.

59. Brieger A, Plotz G, Hinrichsen I, Passmann S, Adam R, Zeuzem S. C-Terminal Fluorescent Labeling Impairs Functionality of DNA Mismatch Repair Proteins. PLoS

ONE [Internet]. 2012 Feb 14 [cited 2020 Jan 8];7(2). Available from: https://www.ncbi.nlm.nih.gov/pmc/articles/PMC3279419/.

60. Shiomi D, Margolin W. The C-Terminal Domain of MinC Inhibits Assembly of the Z Ring in *Escherichia coli*. J Bacteriol. 2007 Jan;189(1):236–43.

61. Weill U, Krieger G, Avihou Z, Milo R, Schuldiner M, Davidi D. Assessment of GFP Tag Position on Protein Localization and Growth Fitness in Yeast. J Mol Biol. 2019 Feb 1;431(3):636–41.

62. Andresen M, Schmitz-Salue R, Jakobs S. Short tetracysteine tags to beta-tubulin demonstrate the significance of small labels for live cell imaging. Mol Biol Cell. 2004 Dec;15(12):5616–22.

63. Thiol-reactive dyes for fluorescence labeling of proteomic samples - Tyagarajan - 2003 - ELECTROPHORESIS - Wiley Online Library [Internet]. [cited 2020 Mar 26]. Available from: https://onlinelibrary.wiley.com/doi/10.1002/elps.200305478.

64. Yang F, Moss LG, Phillips GN. The molecular structure of green fluorescent protein. Nat Biotechnol. 1996 Oct;14(10):1246–51.

65. Novick RP. Plasmid incompatibility. Microbiol Mol Biol Rev. 1987 Dec 1;51(4):381–95.

66. Nordström K, Austin SJ. Mechanisms That Contribute to the Stable Segregation of Plasmids. Annu Rev Genet. 1989;23(1):37–69.

67. Molecular Cloning [Internet]. [cited 2020 Feb 25]. Available from: http://www.molecularcloning.com/.

68. Austin S, Nordström K. Partition-mediated incompatibility of bacterial plasmids. Cell. 1990 Feb 9;60(3):351–4.

69. Velappan N, Sblattero D, Chasteen L, Pavlik P, Bradbury ARM. Plasmid incompatibility: more compatible than previously thought? Protein Eng Des Sel. 2007 Jul 1;20(7):309–13.

70. Shafferman A, Helinski DR. Structural properties of the beta origin of replication of plasmid R6K. J Biol Chem. 1983 Apr 10;258(7):4083–90.

71. Schmidt CM, Shis DL, Nguyen-Huu TD, Bennett MR. Stable Maintenance of Multiple Plasmids in *E. coli* Using a Single Selective Marker. ACS Synth Biol. 2012 Oct 19;1(10):445–50.

72. Paschon DE, Patel ZS, Ostermeier M. Enhanced Catalytic Efficiency of Aminoglycoside Phosphotransferase (3′)-IIa Achieved Through Protein Fragmentation and Reassembly. J Mol Biol. 2005 Oct 14;353(1):26–37.

73. Hirata R, Ohsumk Y, Nakano A, Kawasaki H, Suzuki K, Anraku Y. Molecular structure of a gene, VMA1, encoding the catalytic subunit of H(+)-translocating adenosine triphosphatase from vacuolar membranes of *Saccharomyces cerevisiae*. J Biol Chem. 1990 Apr 25;265(12):6726–33.

74. Kane PM, Yamashiro CT, Wolczyk DF, Neff N, Goebl M, Stevens TH. Protein splicing converts the yeast TFP1 gene product to the 69-kD subunit of the vacuolar H(+)-adenosine triphosphatase. Science. 1990 Nov 2;250(4981):651–7.

75. Brenzel S, Kurpiers T, Mootz HD. Engineering Artificially Split Inteins for Applications in Protein Chemistry: Biochemical Characterization of the Split Ssp DnaB Intein and Comparison to the Split Sce VMA Intein. Biochemistry. 2006 Feb 1;45(6):1571–8.

76. Zettler J, Schütz V, Mootz HD. The naturally split Npu DnaE intein exhibits an extraordinarily high rate in the protein trans-splicing reaction. FEBS Lett. 2009;583(5):909–14.

77. Perler FB. InBase: the Intein Database. Nucleic Acids Res. 2002 Jan 1;30(1):383–4.

78. Park K-T, Du S, Lutkenhaus J. MinC/MinD copolymers are not required for Min function. Mol Microbiol. 2015;98(5):895–909.

79. Shen B, Lutkenhaus J. Examination of the interaction between FtsZ and MinCN in *E. coli* suggests how MinC disrupts Z rings. Mol Microbiol. 2010;75(5):1285–98.

80. Zhou H, Lutkenhaus J. MinC Mutants Deficient in MinD- and DicB-Mediated Cell Division Inhibition Due to Loss of Interaction with MinD, DicB, or a Septal Component. J Bacteriol. 2005 Apr 15;187(8):2846–57.

81. Abebe AH, Aranovich A, Fishov I. HU content and dynamics in *Escherichia coli* during the cell cycle and at different growth rates. FEMS Microbiol Lett [Internet]. 2017 Oct 16 [cited 2020 Mar 18];364(19). Available from: https://academic.oup.com/femsle/article/364/19/fnx195/4157278.

82. Zheng M, Chiang Y-L, Lee H-L, Kong L-R, Hsu S-TD, Hwang I-S, *et al*. Self-assembly of MinE on the membrane underlies formation of the MinE ring to sustain function of the *Escherichia coli* Min system. J Biol Chem. 2014 Aug 1;289(31):21252–66.

83. Zhang Y, Rowland S, King G, Braswell E, Rothfield L. The relationship between hetero-oligomer formation and function of the topological specificity domain of the *Escherichia coli* MinE protein. Mol Microbiol. 1998 Oct;30(2):265–73.

84. Cheriyan M, Pedamallu CS, Tori K, Perler F. Faster Protein Splicing with the *Nostoc punctiforme* DnaE Intein Using Non-native Extein Residues. J Biol Chem. 2013 Mar 1;288(9):6202–11.

85. Palanisamy N, Degen A, Morath A, Ballestin JB, Juraske C, Öztürk MA, *et al*. Split intein-mediated selection of cells containing two plasmids using a single antibiotic. Nat Commun. 2019 Oct 31;10(1):1–15.

86. Mills KV, Johnson MA, Perler FB. Protein Splicing: How Inteins Escape from Precursor Proteins. J Biol Chem. 2014 May 23;289(21):14498–505.

87. Galarneau A, Primeau M, Trudeau L-E, Michnick SW. β-Lactamase protein fragment complementation assays as *in vivo* and *in vitro* sensors of protein–protein interactions. Nat Biotechnol. 2002 Jun;20(6):619–22.

88. Wehrman T, Kleaveland B, Her J-H, Balint RF, Blau HM. Protein–protein interactions monitored in mammalian cells via complementation of β-lactamase enzyme fragments. Proc Natl Acad Sci. 2002 Mar 19;99(6):3469–74.

89. Kuriata A, Gierut AM, Oleniecki T, Ciemny MP, Kolinski A, Kurcinski M, et al. CABS-flex 2.0: a web server for fast simulations of flexibility of protein structures. Nucleic Acids Res. 2018 Jul 2;46(W1):W338–43.

90. Di Ventura B, Sourjik V. Self-organized partitioning of dynamically localized proteins in bacterial cell division. Mol Syst Biol. 2011 Jan 1;7(1):457.

91. Ghosal D, Trambaiolo D, Amos LA, Löwe J. MinCD cell division proteins form alternating copolymeric cytomotive filaments. Nat Commun. 2014 Dec 15;5:5341.

92. Conti J, Viola MG, Camberg JL. The bacterial cell division regulators MinD and MinC form polymers in the presence of nucleotide. FEBS Lett. 2015;589(2):201–6.

93. Taviti AC, Beuria TK. MinD directly interacting with FtsZ at the H10 helix suggests a model for robust activation of MinC to destabilize FtsZ polymers. Biochem J. 2017 Sep 15;474(18):3189–205.

94. Oldfield CJ, Uversky VN, Dunker AK, Kurgan L. Chapter 1 - Introduction to intrinsically disordered proteins and regions. In: Salvi N, editor. Intrinsically Disordered Proteins [Internet]. Academic Press; 2019 [cited 2020 Mar 19]. p. 1–34. Available from: http://www.sciencedirect.com/science/article/pii/B9780128163481000016.

95. Anbo H, Sato M, Okoshi A, Fukuchi S. Functional Segments on Intrinsically Disordered Regions in Disease-Related Proteins. Biomolecules. 2019 Mar;9(3):88.

96. Friedman AM, Fischmann TO, Steitz TA. Crystal structure of lac repressor core tetramer and its implications for DNA looping. Science. 1995 Jun 23;268(5218):1721–7.

97. Lewis M, Chang G, Horton NC, Kercher MA, Pace HC, Schumacher MA, *et al*. Crystal Structure of the Lactose Operon Repressor and Its Complexes with DNA and Inducer. Science. 1996 Mar 1;271(5253):1247–54.

98. Kalodimos CG, Biris N, Bonvin AMJJ, Levandoski MM, Guennuegues M, Boelens R, *et al.* Structure and Flexibility Adaptation in Nonspecific and Specific Protein-DNA Complexes. Science. 2004 Jul 16;305(5682):386–9.

99. Akerlund T, Gullbrand B, Nordström K. Effects of the Min system on nucleoid segregation in *Escherichia coli*. Microbiol Read Engl. 2002 Oct;148(Pt 10):3213–22.

100. Akerlund T, Bernander R, Nordström K. Cell division in *Escherichia coli minB* mutants. Mol Microbiol. 1992;6(15):2073–83.

101. Capiaux H, Lesterlin C, Pérals K, Louarn JM, Cornet F. A dual role for the FtsK protein in *Escherichia coli* chromosome segregation. EMBO Rep. 2002 Jun 1;3(6):532–6.

102. Stouf M, Meile J-C, Cornet F. FtsK actively segregates sister chromosomes in *Escherichia coli*. Proc Natl Acad Sci. 2013 Jul 2;110(27):11157–62.

103. Männik J, Bailey MW, O'Neill JC, Männik J. Kinetics of large-scale chromosomal movement during asymmetric cell division in *Escherichia coli*. PLOS Genet. 2017 Feb 24;13(2):e1006638.

104. Bernhardt TG, de Boer PAJ. SlmA, a Nucleoid-Associated, FtsZ Binding Protein Required for Blocking Septal Ring Assembly over Chromosomes in *E. coli*. Mol Cell. 2005 May 27;18(5):555–64.

105. Ma L, King GF, Rothfield L. Positioning of the MinE binding site on the MinD surface suggests a plausible mechanism for activation of the *Escherichia coli* MinD ATPase during division site selection. Mol Microbiol. 2004 Oct;54(1):99–108.

106. Kentner D, Sourjik V. Dynamic map of protein interactions in the *Escherichia coli* chemotaxis pathway. Mol Syst Biol. 2009;5:238.

107. Zacharias DA, Violin JD, Newton AC, Tsien RY. Partitioning of lipid-modified monomeric GFPs into membrane microdomains of live cells. Science. 2002 May 3;296(5569):913–6.

108. Romei MG, Boxer SG. Split Green Fluorescent Proteins: Scope, Limitations, and Outlook. Annu Rev Biophys. 2019 May 6;48:19–44.

109. Dassa B, London N, Stoddard BL, Schueler-Furman O, Pietrokovski S. Fractured genes: a novel genomic arrangement involving new split inteins and a new homing endonuclease family. Nucleic Acids Res. 2009 May 1;37(8):2560–73.

110. Ishikawa H, Meng F, Kondo N, Iwamoto A, Matsuda Z. Generation of a dual-functional split-reporter protein for monitoring membrane fusion using self-associating split GFP. Protein Eng Des Sel. 2012 Dec 1;25(12):813–20.

111. Varshavsky A. N-degron and C-degron pathways of protein degradation. Proc Natl Acad Sci. 2019 Jan 8;116(2):358–66.

112. Yan BX, Sun YQ. Glycine Residues Provide Flexibility for Enzyme Active Sites. J Biol Chem. 1997 Feb 7;272(6):3190–4.

113. Isalan M, Lemerle C, Michalodimitrakis K, Horn C, Beltrao P, Raineri E, *et al*. Evolvability and hierarchy in rewired bacterial gene networks. Nature. 2008 Apr;452(7189):840–5.

114. Schindelin J, Arganda-Carreras I, Frise E, Kaynig V, Longair M, Pietzsch T, *et al*. Fiji: an open-source platform for biological-image analysis. Nat Methods. 2012 Jul;9(7):676–82.